

Grichar Valdes Santurio

## Dosimetry for new radiotherapy modalities:

Towards improved traceability for scintillator dosimetry in small MV photon beams



Ph.D. Thesis

Risø 2019

**DTU Nutech**  
Center for Nuclear Technologies

---

**Dosimetry for new radiotherapy modalities:**

Towards improved traceability for scintillator dosimetry in small MV photon beams

**Author**

Grichar Valdes Santurio

**Supervisor**

Claus E. Andersen

**DTU Nutech**

Center for Nuclear Technologies

Technical University of Denmark

Frederiksborgvej 399

DK-4000, Roskilde

Denmark

<http://www.nutech.dtu.dk/english>

Tel: (+45) 4677 4900

# Summary (English)

---

For over a century, radiotherapy treatments have been used as weapon against cancer. The main objective of radiotherapy is to deliver high dose to the tumor and spare the adjacent healthy tissues, and accuracy is of vital importance when delivering these treatments. The inclusion of multi-leaf collimators and image guidance in megavoltage linear accelerators has enabled complex shaping of the beam with irradiation field sizes smaller than  $1 \times 1 \text{ cm}^2$ . These improvements in treatment techniques pose several dosimetric challenges, and measurement of the absorbed dose in such small fields using conventional guidelines and detectors developed for larger fields with nearly full charge-particle equilibrium was found to lead to a large spread in results. The effect of this inconsistency in dose would potentially result in an over- or under-treatment of patients, and hospitals was therefore not be able to use the new treatment technology to its full potential before these problems were resolved.

In 2017, the International Atomic Energy Agency (IAEA) and the American Association of Medical Physics (AAPM) published a first code of practice (TRS-483) for determining the absorbed dose under small field conditions for MV photon beams. Since primary standards for small field dosimetry are not well established, the code of practice could not be directly based on such standards. The code of practice therefore derived traceability to the gray (Gy) in the international system of units (SI) using standards for conventional large fields combined with Monte-Carlo computed correction factors for small fields. However, the code of practice highlights the potential of using fiber-coupled organic plastic scintillators for direct measurements of output factors as these detectors (i) are practically water equivalent, and (ii) have small sensitive volumes. One issue of concern, however, is that scintillating detectors suffer from signal loss during irradiation, called ionization quenching. The importance of this effect was not directly addressed in the TRS-483 code of practice, and a main objective of the present study therefore was to assess the importance of ionization quenching in MV photon beam dosimetry with organic plastic scintillators, in particular for measurements of field output factors.

A Monte Carlo-based method was developed to evaluate the importance of ionization quenching in organic plastic scintillators during MV photon dosimetry. The method accounts for dose deposition by secondary electrons based on

a modified version of Birks law. Ionization quenching was found to have a small but statistically significant influence on two relevant applications:  $(0.6 \pm 0.2) \%$  for the field output factor measurements between  $0.5 \times 0.5 \text{ cm}^2$  and  $10 \times 10 \text{ cm}^2$  and about  $(2 \pm 0.4) \%$  for the ionization chamber  $k_Q$ -factor measurements for beams between 4 MV and 15 MV. The modelling results were in agreement with experimental measurements. The results support that the ionization quenching effect has a small effect on field-output factor measurements and it can probably be neglected during clinical measurement conditions.

Finally, a new dosimetric system based on graphite calorimetry and a scintillator transfer detector for direct measurement of traceable field output factors was proposed. Monte-Carlo computations support that the designed calorimeter is suitable for establishing an alternative, more direct route to traceable measurements of absorbed doses in small field sizes down to  $1 \times 1 \text{ cm}^2$  (less than 3 % correction). An important feature of the new scintillator transfer detector is that it provides an improved blinding-technique for separating the scintillator signal from the stem signal (Cerenkov light and fluorescence produced in the optical fiber cable by the primary beam and scattered radiation). The proposed dosimetric system supports the existing TRS-483 code of practice and it provides an alternative, more direct route to traceable field output factor measurements. The work in this thesis therefore is a step towards improvements in radiotherapy treatments.

# Resumé (Danish)

---

Stråleterapi har gennem de sidste hundrede år været anvendt som en behandling mod kræft. Hovedformålet er at give en høj dosis til tumorområdet, og samtidig skåne det omkringliggende raske væv. Nøjagtighed er af afgørende betydning for sådanne behandlinger. Udviklingen af nye flerbladskollimatorer og indbygget billedvejledning i lineare accelerators har muliggjort kompleks tilpasning af strålefeltet med anvendelse af feltstørrelse ned til  $1 \times 1 \text{ cm}^2$  eller mindre. Disse forbedringer i behandlingsteknologi giver en række udfordringer for dosimetrien, særligt vedrørende måling af absorberet dosis i små felter. Anvendelse af konventionelle måleprotokoller, der oprindeligt er udviklet for måling i store felter med næste fuldt udviklet ladetpartikelligevægt, har vist sig at give en stor spredning i resultater for små felter. En konsekvens af denne inkonsistent er at hospitaler ikke har kunne udnytte det fulde potentiale af den nye behandlingsteknologi førend disse måletekniske problemer blev løst. I 2017 udgav det Internationale Atomenergiagentur (IAEA) og det amerikanske selskab for medicinsk fysik (AAPM) den første protokol (TRS-483) for måling af absorberet dosis i små felter ved megavolt fotonbestrålinger. Eftersom der ikke er veletablerede primære standarder for småfeltdosimetri, kunne protokollen ikke baseres på sådanne standarder. Protokollen etablerede derfor sporbarhed til målestørrelsen gray (Gy) i det internationale enhedssystem (SI) ved anvendelse af standarder for konventionelle, store strålingsfelter kombineret med Monte-Carlo beregnede korrektionsfaktorer for små felter. Dog fremhævede protokollen anvendelsen af organiske plastscintillatorer til direkte måling af outputfaktorer, idet disse detektorer har (i) en høj grad af vandækvivalens og (ii) et lille målevolumen. Et enkelt forhold, som imidlertid kunne give anledning til bekymring, er at scintillatorer udviser ioniseringsquenching således, at der udsendes mindre lys pr. dosis, hvis bestrålingen foregår ved høj ioniseringsstæthed. Betydningen af dette problem behandles ikke direkte in TRS-483, og hovedformålet med nærværende arbejde er derfor at anslå betydningen af ioniseringsquenching for scintillatordosimetri i MV fotonbestrålinger, herunder særligt ved måling af outputfaktorer. En Monte-Carlo baseret metode er udviklet for at evaluere betydningen af ioniseringsquenching i organiske plastscintillatorer i forbindelse med MV fotondosimetri. Metoden tager højde for dosisdepositionen fra sekundære elektroner under anvendelse af en modificeret anvendelse af Birks lov. Ioniseringsquenching blev fundet til at have en lille, men

statistisk signifikant indflydelse på to undersøgte anvendelser:  $(0.6 \pm 0.2)$  % for outputfactormålinger for felter mellem  $0.5 \times 0.5 \text{ cm}^2$  og  $10 \times 10 \text{ cm}^2$ , samt omkring  $(2 \pm 0.4)$  % for ionkammer  $k_Q$ -faktormålinger i beams mellem 4 MV og 15 MV. Modelberegningerne var i overensstemmelse med målinger. Resultaterne understøtter at ioniseringsquenching har en lille effekt på outputfactormålinger, og effekten kan sandsynligvis negligeres under kliniske måleforhold. Arbejdet omfatter desuden et forslag til et nyt dosimetrisystem for direkte måling af outputfaktorer. Systemet er baseret på grafitkalorimetri og en scintillator som overførselsdetektor. Monte-Carlo beregninger understøtter, at det foreslåede kalorimeter er anvendelig til at etablere en alternativ, mere direkte vej til sporbare måling af absorberet dosis i strålingsfelter ned til  $1 \times 1 \text{ cm}^2$  (mindre end 3 % korrektion). En vigtig egenskab ved den nye scintillatordetektor er at den muliggør adskillelse af scintillatorsignalet fra det lys, som dannes i selve fiberkablet under bestrålingen (Cerenkov lys og fluorescens) ved anvendelse af en blandingsteknik. Det foreslåede dosimetrisystem understøtter TRS-483 protokollen og tilvejebringer en alternativ, mere direkte vej til sporbare outputfactormålinger. Arbejdet i denne afhandling er derfor et bidrag til forbedret stråleterapi.

# Acknowledgements

---

This work was carried out within the framework of the project: “Dosimetry for new radiotherapy modalities”, Danish Council for Independent Research (grant FTP, DFF – 4184-00151).

I will like to thank all the people that, in one way or another, contributed not only with the work carried out in this thesis but also brought joy into my life in the last three years. Just to mention a few:

I want to thank my supervisor (whom I consider my friend) Claus E. Andersen. Working with you have been like a romantic comedy movie, ups and downs but with a guarantee happy ending. I am deeply grateful for your support and advice in these last 3 years and 4 months.

To Massimo Pinto for welcoming me in your lab and sharing your knowledge with me (during and after my stay in Rome). Grazie mille!

To the EGSnrc developers. Ernesto, Reid, Freddy and Blake. Thanks so much for replying to my mails.

To my office mates during these 3 years: Jakob, Martin, Elaine, Magdalena, Trine, Rocio, Nikola, Nicolai, Susanne, and Patrik. Sharing office with you has been a unique experience (positive). Thanks for all the discussions, jokes and for not complaining about how I play guitar!

To my friends in the campus and the Friday bar crew. Megha, Peyman, Tato, Djordije, Steven, Xu, and Maria. You all have made me feel like “home” every minute we have spent together. I am deeply grateful for that.

To Ilaria Ritucci and Jeppe Brage Christensen for their friendship, help and support, not only with Latex or Solidworks but also with all possible things. Thanks a lot!

Finally to my family. Samu, Phunda and Christina. Thank you all for filling me up with love and support. You all have made me a better person with your love and support. I am, and will be eternally grateful for that.



# List of Publications and Presentations

---

**Publications** in peer-reviewed journals:

**Paper 1:** Valdes Santurio, G. Pinto, M. and Andersen, C. E.

Evaluation of the ionization quenching effect in organic plastic scintillators using kV x-rays and a modified Birks model with explicit account of secondary electrons

*Submitted to Radiation Measurements, March 2019*

**Paper 2:** Valdes Santurio, G. and Andersen, C. E.

Quantifying the ionization quenching effect in organic plastic scintillators used in MV photon dosimetry

*Submitted to Radiation Measurements, March 2019*

**Oral presentations** at national and international conferences:

- 5th Öresund Workshop on Radiotherapy. Helsingborg, Sweden. 2017
- XII Latin-American Symposium on Nuclear Physics and Applications (LANPA). Havana, Cuba. 2017

**Poster presentations** at national and international conferences:

- European Society for Radiotherapy & Oncology (ESTRO) 35 congress Turin, Italy. 2016
- Solid State Dosimetry (SSD) 18th International Conference Munich, Germany. 2016
- European Society for Radiotherapy & Oncology (ESTRO) 36 congress Vienna, Austria. 2017

- International Conference on Monte Carlo Techniques for Medical Application. Naples, Italy. 2017

**Oral or poster presentations** at national and international conferences not covered in this thesis:

- European Congress of Medical Physics. Copenhagen, Denmark. 2018 (Poster)
- European Congress of Medical Physics. Copenhagen, Denmark. 2018 (Oral)

# List of Acronyms

---

WHO	World Health Organization
IAEA	International Atomic Energy Agency
TRS	Technical Report Series
AAPM	American Association of Medical Physics
COP	Code of Practice
IMRT	Intensity Modulated Radiation Therapy
VMAT	Volumetric Modulated Arc Therapy
SRT	Sterotactic Radiotherapy
PSL	Primary Standard Laboratory
IC	Ionization Chamber
TPR	Tissue-phantom-ratio
TMR	Tissue-maximum-ratio
PDD	Percentage-depth-dose
DAP	Dose-area product
CSDA	Continuous slowing down approximation
OF	Output factor
clin	Clinical
msr	Machine-specific reference
MC	Monte Carlo
IPEM	Institute of Physics and Engineering in Medicine
ICRU	International Commission of Radiation Units and Measurements
CSDA	Continuous Slowing Down Approximation
PMT	Photomultiplier tube

CLR	Cerenkov light ratio
VRT	Variance reduction techniques
AO	Ausgab Objects
DBS	Directional Bremsstrahlung Splitting
SSD	Source-to-surface distance
CM	Component Modules
phsp	Phase space
TPS	Treatment Planning System
PMMA	Polymethylmethacrylate
ENEA-INMRI	Italian National Metrology Institute of Ionizing Radiation
HVL	Half-value layer
SAD	Source-to-axis distance
PTB	National Metrology Institute of Germany
WLS	Without lateral scatter
FLS	Full lateral scatter
SP-1	Scintillating pipe

# List of Symbols

---

$k_{Q,Q_0}$	Beam quality correction factor
$N_{D,w,Q}$	Calibration coefficient
$k_{ioq}$	Ionization quenching correction factor
$k_{temp}$	Temperature correction factor for scintillators
$L_{\Delta}$	Restricted electronic stopping power
$k_{Q_{clin},Q_{msr}}^{f_{clin},f_{msr}}$	Output correction factor
$\Omega_{Q_{clin},Q_{msr}}^{f_{clin},f_{msr}}$	Field output factor
$L(E)$	Light yield
$K_{col}$	Collision kerma
$k_B$	Quenching parameter
$(s_{w,air})_Q$	Stopping power ratio
$W_{air}$	Mean energy expended in air per ion pair formed
$P$	Perturbation factors
$R_{CSDA}$	Range in the continuous slowing down approximation
$T$	Temperature
$R_T$	Scintillator response at a certain temperature
$\epsilon$	Efficiency of a Monte Carlo computation
$\sigma^2$	Variance of the mean in a Monte Carlo simulation
$\frac{\mu_{en}}{\rho}$	Mass energy-absorption coefficient
$\epsilon_{\lambda}^{meas}$	Sensitivity of a scintillator
$\alpha_{\lambda}$	Scintillator inherent sensitivity



# Contents

---

Summary (English) .....	i
Resumé (Danish) .....	iii
Acknowledgements .....	v
List of Publications and Presentations .....	vii
<b>1 Introduction .....</b>	<b>1</b>
1.1 Motivation .....	1
1.2 Hypothesis .....	3
1.3 Outline .....	3
References .....	4
<b>2 Theoretical framework .....</b>	<b>7</b>
2.1 Dosimetry in Radiotherapy .....	7
2.1.1 Absolute Dosimetry .....	8
2.1.2 Reference Dosimetry: TRS-398 .....	9
2.1.3 Relative Dosimetry: TRS-398/483 .....	11
2.2 Dosimetry Model .....	12
2.3 Scintillator Dosimetry .....	13
2.3.1 Ionization Quenching Effect .....	13
2.3.2 Stem removal: Cerenkov radiation and retarded fluorescence .....	15
2.3.3 Temperature Dependence .....	16
2.4 Scintillator Application in Small Field Dosimetry .....	17
References .....	18
<b>3 Monte Carlo .....</b>	<b>23</b>
3.1 Introduction .....	23
3.2 EGSnrc .....	24
3.2.1 Variance Reduction Techniques .....	24
3.2.2 Radiation Source: BEAMnrc .....	25

3.2.3	Fluence: <code>cavity</code> and <code>FLURZnrc</code> .....	27
3.2.4	Absorbed Dose and Dose Distributions: <code>egs_chamber</code> ...	28
3.2.5	Collision Kerma: <code>egs_kerma</code> and <code>g</code> .....	29
3.2.6	Light Yield and Cumulative Absorbed Dose per Electron Energy .....	33
	References .....	35
<b>4</b>	<b>Evaluation of the ionization quenching effect in organic plastic scintillators using kV x-rays and a modified Birks model with explicit account of secondary electrons.....</b>	<b>39</b>
4.1	Introduction .....	40
4.2	Materials and Methods.....	40
4.2.1	Organic Plastic Scintillator .....	40
4.2.2	Radiation Source and measurements .....	41
4.2.3	Computed spectra .....	44
4.2.4	Light Yield Analysis .....	44
4.2.5	Monte Carlo computations .....	45
4.3	Results .....	46
4.3.1	Scintillator measurements .....	46
4.3.2	Spectra .....	47
4.3.3	Light Yield.....	47
4.4	Discussion .....	49
	References .....	51
<b>5</b>	<b>Quantifying the ionization quenching effect in organic plastic scintillators used in MV photon dosimetry.....</b>	<b>55</b>
5.1	Introduction .....	56
5.2	Materials and Methods.....	57
5.2.1	Formalism.....	57
5.2.2	Field Output Factor.....	58
5.2.3	Light Yield.....	59
5.2.4	Ionization Quenching Correction Factor.....	59
5.2.5	Experimental set-up.....	60
5.3	Monte Carlo Calculations.....	60
5.4	Results .....	62
5.5	Cumulative Absorbed Dose .....	62
5.6	Ionization Quenching Correction Factor .....	63
5.7	Output Factors .....	63
5.8	Beam Quality Correction Factor .....	64
5.9	Discussion .....	65
	References .....	69
<b>6</b>	<b>Design of a dosimetric system for establishing traceable output factor measurement in radiotherapy MV photon beams .</b>	<b>73</b>

6.1	Materials and Methods.....	76
6.1.1	Output Factors TRS-483 .....	76
6.1.2	Monte Carlo Calculations.....	76
6.1.3	Temperature dependence: $k_{\text{temp}}$ .....	77
6.1.4	Stem Signal: Pipe Blinding Removal .....	77
6.1.5	Light Yield.....	80
6.1.6	Output correction factor .....	83
6.2	Results .....	85
6.2.1	Output Factors .....	85
6.2.2	Field size dependence of SP-1 .....	85
6.2.3	Calorimeter design .....	86
6.2.4	Ionization Quenching Correction Factor.....	88
6.2.5	Output Correction Factor .....	90
6.3	Discussion .....	90
6.4	Conclusions .....	93
	References .....	93
<b>7</b>	<b>Summary and Outlook .....</b>	<b>97</b>
7.1	Summary .....	97
7.1.1	Monte Carlo .....	97
7.1.2	Ionization quenching effect using kV x-rays.....	98
7.1.3	Ionization quenching effect in MV photon dosimetry.....	98
7.1.4	Design of dosimetric system for establishing output factors in MV photon beams .....	98
7.1.5	Main conclusions .....	99
7.2	Outlook.....	100
<b>A</b>	<b>C++ ausgab object .....</b>	<b>101</b>
A.1	egs_light_scoring.....	102



# Introduction

---

## 1.1 Motivation

According to the 2018 report by the World Health Organization (WHO) [1], cancer is the second leading cause of death worldwide, and in Denmark, 4 of the 10 diseases leading to death are cancer related. The three main cancer treatments are radiotherapy, chemotherapy and surgery either used individually or in combination with each other. During the last century, radiotherapy treatments have not only cured patients, but also insured a better life quality for those that are non-curable. In order to share clinical experiences and therefore improve treatments quality, it is of utmost importance that radiotherapy clinics worldwide are traceable to the same standard for absolute dose, the Gy. Therefore, calibration of cobalt machines, linear accelerators, and radiation detectors can be done uniformly. Moreover, the International Atomic Energy Agency (IAEA) as well as the American Association of Medical Physics (AAPM) have published specific guidelines, commonly known as code of practice (COP) [2, 3], describing how to determine the absorbed dose to water under different standard treatment conditions.

In an ongoing pursuit to deliver more accurate treatments to patients, modern radiotherapy techniques have changed significantly due to new technological advances. In techniques such as Intensity Modulated Radiation Therapy (IMRT) [4], Volumetric Modulated Arc Therapy (VMAT) [5], Tomotherapy [6], and Stereotactic Radiotherapy (SRT) [7], the dose is delivered to the patient through small or non-standard radiation fields. A more conform dose can be delivered to the tumor and therefore adjacent healthy tissue can be spared when such non-standard fields are used. However, the published guidelines [2, 3] up to when this project was conceived, do not cover treatment conditions using small or non-standard radiation fields, thereby introducing dosimetric challenges in regard to ensuring doses are delivered with the required uncertainty. A lack of standardized guidelines for small radiation fields have been hampering the precision of doses delivered in radiotherapy clinics. This was highlighted by Alfonso et al. [8], whom

reported discrepancies of more than 10% when measuring the absorbed dose for a small field size compared to the reference ( $10 \times 10 \text{ cm}^2$ ) with different radiation detectors. As a result, the authors recommended that a new set of guidelines for small and non-standard beams should be published.

9 years after a new formalism was recommended by Alfonso et al. [8], a joined protocol from the IAEA and the AAPM was issued: TRS-483 [2]. This COP gives guidelines on how to measure the absorbed dose under small or non-standard radiation conditions. For different radiation detectors and field sizes, recommendations on values of output correction factors for measuring the absorbed dose in small radiation fields with respect to reference conditions are given. Of the studied detectors, the fiber-coupled organic plastic scintillator is the only detector that does not require a correction for field sizes down to ( $0.4 \times 0.4 \text{ cm}^2$ ). However, the ionization quenching effect, present in all scintillating detectors, is not taken into account in the published data, on which the COP is based on. Therefore, a rigorous characterization of the ionization quenching and the fiber perturbation is still very much needed.

Primary standards, for direct calibration of detectors under small field configurations have not yet been developed. As pointed out in the COP [9], few PSLs based on calorimetry have made an attempt to determine the absorbed dose to water under small radiation field configurations for ionization chamber calibrations [10–12] down to  $3 \times 3 \text{ cm}^2$ . Higher corrections were obtained in those studies, yielding a 5% for field sizes down to  $3 \times 3 \text{ cm}^2$  and up to 60% for a field size of  $1.8 \times 1.8 \text{ cm}^2$ . Therefore, a method for determining the absorbed dose traceable to primary standards for small field dosimetry is yet to be implemented. An alternative route to this problem have been developed using the dose area product (DAP) concept. In this approach the beam profile across the calorimeter cross section needs to be well known in order to convert from dose to an area to dose to a point. Therefore, a third detector for measuring the dose profile needs to be used. Hence, the uncertainty for determining the absorbed dose to a point increases when using this approach [13].

The present work aims to design a calorimetry based dosimetric system for computing output correction factors with a sub-percent level of uncertainty. With the developed calorimeter, the ionization quenching effect for organic plastic scintillators used in small field conditions can be assessed. The well-characterized scintillator will be used as a reference detector for the determination of the output correction factor, thereby obtaining an uncertainty smaller than that reported in the COP. This approach will enable radiotherapy clinics in Denmark to have a detector-specific output correction factor, which means that treatments under these conditions will be more accurate. The outcome of this work will lead to a higher precision in delivered doses, ultimately offering a better treatment for cancer in Denmark.

## 1.2 Hypothesis

The overall objective is to design, characterize and apply an instrument that can establish traceability to the gray (Gy) in the international measurement system (SI) for small field dosimetry based on the following hypotheses:

1. The primary hypothesis is that a calorimeter-based instrument using ultra-pure graphite and organic scintillator technology as a transfer standard can be designed and constructed. Such instrument will allow for accurate (sub-percent standard uncertainty) dose measurements in small fields (down to  $1 \times 1 \text{ cm}^2$  or smaller) relative to conventional reference fields ( $10 \times 10 \text{ cm}^2$ ) for clinically relevant radiotherapy x-ray beams (4–18 MV x-rays).
2. The secondary hypothesis is that this instrument can be used to establish traceability for clinical dosimeter systems in use at hospitals in the form of generic correction factors and/or calibration of specific dosimeters.
3. The third hypothesis is that the instrument can be used to consolidate that special solid-state dosimeter systems in use at DTU (and partly developed by DTU) offer both minimal perturbation and a constant signal-per-dose for radiotherapy beams with different field sizes.

## 1.3 Outline

The present thesis contains 7 chapters and one appendix. The chapters are organized to document how complications were appearing while carrying out the project.

Chapter 1 presents an introduction to the thesis. This chapter gives an overview of the state of the art of this topic and conveys the importance. The hypothesis as well as general and specific objectives are presented followed by the outline of the thesis.

Chapter 2 exhibit the theoretical framework used in the thesis. A description of physics and logic behind radiotherapy is covered in this chapter. Tied with the purpose of this thesis, the physical scintillator operation principles are described as well as its complications. An outline of the three step dosimetric model is given using ionization chambers and organic plastic scintillators as examples. Finally it is described how the theory is used in the thesis.

Chapter 3 introduces the Monte Carlo method for radiation transport and introduces the EGSnrc toolkit. A detailed explanation of each of the applications available in EGSnrc, used in this thesis, is given. A Monte Carlo validation of the linear accelerator model was carried out obtaining good agreement with experimental measurements. An application for computing collision kerma, not available in EGSnrc distribution, is presented and validated against benchmark applications available in the same software. A modified ausgab object for the

computation of light yield in scintillators is introduced and validated against both, an analogue computation approach and experimental measurements available in the literature.

Chapter 4 describes an experiment for determining the quenching parameter, using fiber-coupled organic plastic scintillator followed by a validation of the Monte Carlo developed ausgab object. The chapter further presents in detail the procedures followed to obtain the quenching parameter for an organic plastic scintillator. Finally, the effect of ionizing quenching for MV dosimetry can be investigated.

Chapter 5 deals with the impact of ionization quenching effect for MV dosimetry as it was the outlook of the results presented in chapter 4. In this chapter a correction factor for ionization quenching is presented. The importance of taking the ionization quenching into account for direct measurements of output factors and beam quality correction factors is discussed in detail.

Chapter 6 proposes a dosimetric system capable of performing traceable output factor measurements. The proposed dosimetric system is based on graphite calorimetry with a scintillator as a transfer standard detector. The newly designed detector system, for use the transfer detector, is discussed. The designed detector is supported by Monte Carlo simulations and experimental measurements. However, for the graphite calorimeter, experimental measurements were not performed. The proposed dosimetric system employs all theory and results presented in the previous chapters.

Chapter 7 presents the summary of the thesis as well as future recommendations.

Finally the appendix explain in details how to create the ausgab object implemented for the computation of the light yield (discussed in chapter 2).

## References

- [1] TWS Sijabat. *World Health Statistics 2018: Monitoring health for the SDGs*. 2018.
- [2] International Atomic Energy Agency. IAEA Technical Report Series No.398. *Atomic Energy* (2000), 1–229.
- [3] PR Almond, PJ Biggs, and WF Hanson. AAPM 's TG – 51 Protocol for Clinical Reference Dosimetry of High-Energy Photon and Electron Beams. *Medical Physics* **26** (1999) (1999), 1–9.
- [4] IMRTCW Group et al. Intensity-modulated radiotherapy: current status and issues of interest. *International Journal of Radiation Oncology\* Biology\* Physics* **51** (4) (2001), 880–914.
- [5] K Otto. Volumetric modulated arc therapy: IMRT in a single gantry arc. *Medical physics* **35** (1) (2008), 310–317.

- 
- [6] TR Mackie et al. “Tomotherapy”. In: *Seminars in radiation oncology*. Vol. 9. 1. Elsevier. 1999, 108–117.
- [7] M Mitsumori et al. Initial clinical results of LINAC-based stereotactic radiosurgery and stereotactic radiotherapy for pituitary adenomas. *International Journal of Radiation Oncology\* Biology\* Physics* **42** (3) (1998), 573–580.
- [8] R Alfonso et al. A new formalism for reference dosimetry of small and nonstandard fields. *Medical Physics* **35** (11) (2008), 5179–5186.
- [9] H Palmans et al. Dosimetry of small static fields used in external beam radiotherapy: An IAEA-AAPM International Code of Practice for reference and relative dose determination. Technical Report Series No. 483. *Iaea TRS-483* (November) (2017).
- [10] S Duane. Evaluation of Uncertainties. **2016** (January) (2006), 1–15.
- [11] L de Prez. *Small field dosimetry in high energy photon beams based on water calorimetry*. Tech. rep. 2010.
- [12] A Krauss and RP Kapsch. Calorimetric determination of kQ factors for NE 2561 and NE 2571 ionization chambers in 5 cm× 5 cm and 10 cm× 10 cm radiotherapy beams of 8 MV and 16 MV photons. *Physics in Medicine & Biology* **52** (20) (2007), 6243.
- [13] S Dufreneix et al. Using a dose-area product for absolute measurements in small fields: a feasibility study. *Physics in Medicine & Biology* **61** (2) (2015), 650.



## CHAPTER 2

# Theoretical framework

---

In this section the theoretical concepts used in the thesis will be discussed. At first, an introduction and theory of radiotherapy physics will take place. Secondly, the dosimetry model will be explained, using as drivers the ionization chamber and organic plastic scintillators. Next, a description of scintillator dosimetry will take place followed by the application of organic plastic scintillator in small field dosimetry. Finally, a description is given of how the organic plastic scintillator is used in this thesis.

## 2.1 Dosimetry in Radiotherapy

In radiotherapy protocols the dose is reported in terms of absorbed dose to a point in water [1, 2]. This quantity is usually determined in primary standard laboratories (PSL) under conditions that can be reproduced in the clinic, called reference conditions. Radiation detectors under these conditions are calibrated and therefore can be used in the clinic with traceability to that PSL. Subsequently, the calibrated radiation detector is used to establish the absorbed dose to a point in water for reference conditions. The radiation detector commonly used as traceable detector under reference conditions is the ionization chamber (IC). This detectors is extensively used for this purpose. In radiotherapy treatments, the conditions are not usually the reference conditions and therefore an extra dosimetry step is needed in order to relate the absorbed dose under non-reference conditions to reference conditions. Hence the radiotherapy dosimetry can be separated into 3 steps; (i) absolute dosimetry at the PSL, (ii) transfer reference dosimetry from the PSL and the clinic, (iii) relative dosimetry carried out at the clinic in the actual treatment conditions. In the following sections these groups will be explained.

### 2.1.1 Absolute Dosimetry

The absorbed dose is defined as the mean deposited energy per mass in a finite volume. The most fundamental way of determining this quantity is through calorimetry and most of the PSLs, base their absolute dosimetry on calorimetry when used for radiotherapy. Calorimetry, is done mainly using two materials; water or graphite. Although the desirable quantity is the absorbed dose to water, water calorimetry is rather complicated as the water needs to be ultra-pure, at very low temperature (4 °C), using a water cell among other things. Since the graphite have a very similar heat defect it have become an appealing option, of several PSL for calorimetry, is graphite-based.

Two main operational modes are used for graphite-based calorimetry; the quasi-adiabatic and the isothermal mode. Both techniques require the assistance of sensitive electronics (for example Wheatstone bridges) in order to fulfill the conditions required by the method and measure the resistance induced in the thermistors by the irradiation [3]. The quasi-adiabatic mode operates with a constant heat and relates the energy deposited in the detection volume with the raise of temperature through the known heat capacity of the material. The second technique operates with a constant temperature. Electrical energy is used to maintain the components at a constant temperature, such that when the beam is on, the deposited energy in the detection volume is related to the dissipated power (calibrated by substitution) through the thermistors. Both operation modes need corrections due to impurities in the core, presence of thermistors, and heat transfer among others. These corrections are computed by solving the heat transfer equations and therefore the amount of heat that is absorbed purely in the core or other components can be determined. Some software have implemented the heat flow transport equations and have been widely use for this purpose such as COMSOL Multiphysics. Equations 2.1 and 2.2 determine the absorbed dose to the calorimeter core in quasi-adiabatic and isothermal modes respectively.

$$D_{\text{core}} = \frac{\Delta E_{\text{rad}}}{m_{\text{core}}} = c_{p,\text{core}} \Delta T \prod k_i \quad (2.1)$$

$$D_{\text{core}} = \frac{\Delta E_{\text{rad}}}{m_{\text{core}}} = \frac{\int_0^t (P_0 - P_i) dt}{m_{\text{core}}} \prod k_i \quad (2.2)$$

where  $E_{\text{rad}}$  is the deposited energy due to the irradiation processes,  $m_{\text{core}}$  is the mass of the calorimeter core,  $c_{p,\text{core}}$  is the specific heat capacity of the core material,  $T$  is the temperature rise in the core,  $P_0$  and  $P_i$  are the power dissipated in the thermistors at time  $t = 0$  and  $t = i$  and  $\prod k_i$  is the product of all correction factors.

A typical calibration is carried out in three steps [4]; (i) first the calorimeter core is placed at the reference depth under reference conditions (see section 2.1.2) and the absorbed dose is established, (ii) the traceable detector is placed at the same positions under the same conditions, (iii) and finally the detector is placed

in the clinical-like conditions and therefore a relationship between the absorbed dose and the detector response can be established

### 2.1.2 Reference Dosimetry: TRS-398

The widely adopted radiotherapy protocols [1, 2] establish the reference conditions depending on the beam quality of the radiation beam. The beam quality is a proxy for the spectrum of the beam. This quantity is an important characteristic for pulsed accelerator beams as spectral changes occur from machine to machine even for the same nominal energy. For radioactive sources, the spectrum is well known and therefore these are ideal as a reference beam quality (i.e  $^{60}\text{Co}$  for radiotherapy applications). The beam quality for photon beams is given in terms of the tissue phantom ratio  $\text{TPR}_{20,10}$  which is defined as the ratio of absorbed dose in two different conditions measuring at the same detector position; at  $20\text{ g/cm}^2$  and  $10\text{ g/cm}^2$ . Figure 2.1 shows a schematic representation of the  $\text{TPR}_{20,10}$ .

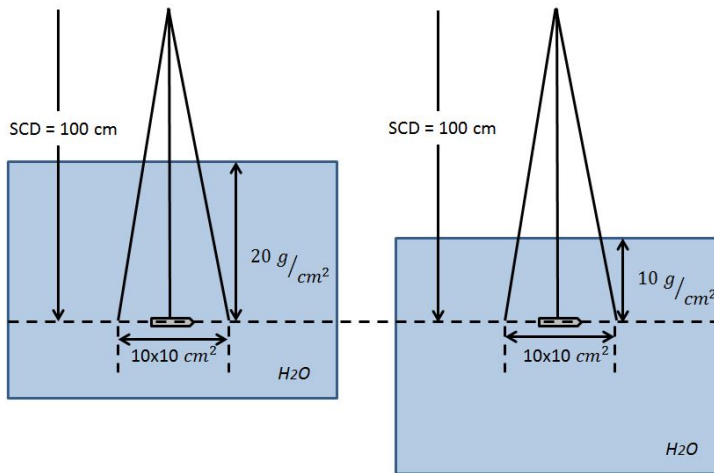


**Figure 2.1:** Diagram showing the definition of  $\text{TPR}_{20,10}$  as the ratio of the absorbed dose in the left configuration over the adsorbed dose of the right configuration for a fixed source-to-chamber distance (SCD)

Table 2.1, extracted from IAEA protocol [1], summarizes the defined reference conditions and the influence quantity.

Under reference conditions the absorbed dose to water  $D_w$ , for a beam quality  $Q$ , at the reference depth  $z_{\text{ref}}$ , in absence of the chamber is given by [1]:

$$D_w = M_Q N_{D,w,Q_0} k_{Q,Q_0} \quad (2.3)$$

**Table 2.1:** Definition of reference conditions. Table reproduced after reference [1].

Influence Quantity	Reference value or reference characteristics
Phantom material	Water
Chamber type	Cylindrical
Measurement depth $z_{\text{ref}}$	For $\text{TPR}_{20,10} < 0.7$ , $10 \text{ g/cm}^2$ (or $5 \text{ g/cm}^2$ ) For $\text{TPR}_{20,10} \geq 0.7$ , $10 \text{ g/cm}^2$
Reference point of the chamber	On the central axis at the center of the cavity volume
Position of the reference point of the chamber	At the measurement depth $z_{\text{ref}}$
SSD/SCD	100 cm
Field size	$10 \times 10 \text{ cm}^2$

where  $M_Q$  is the detector reading corrected by the magnitudes of interest,  $N_{D,w,Q_0}$  is the calibration coefficient in terms of absorbed dose to water for a beam quality  $Q_0$  and  $k_{Q,Q_0}$  is the beam quality correction factor that corrects for the difference between the beam quality  $Q_0$  that the detector was calibrated in, and the quality  $Q$ . For ionization chambers, the corrections are for differences in temperature and pressure than when the ionization chamber was calibrated, electrometer calibration, polarity effect and ion recombination [1]. The beam quality correction factor  $k_{Q,Q_0}$  is defined as:

$$k_{Q,Q_0} = \frac{N_{D,w,Q}}{N_{D,w,Q_0}} \quad (2.4)$$

For ionization chambers this factor can be written as:

$$k_{Q,Q_0} = \frac{N_{D,w,Q}}{N_{D,w,Q_0}} = \frac{D_{w,Q}/M_Q}{D_{w,Q_0}/M_{Q_0}} \quad (2.5)$$

Ideally, this factor should be measured for each ionization chamber to be used in the clinic by a PSL. Since well characterized linear accelerators are not widely available in PSLs, this factor can be theoretically computed as:

$$k_{Q,Q_0} = \frac{(s_{w,\text{air}})_Q}{(s_{w,\text{air}})_{Q_0}} \frac{(W_{\text{air}})_Q}{(W_{\text{air}})_{Q_0}} \frac{P_Q}{P_{Q_0}} \quad (2.6)$$

where  $s_{w,\text{air}}$  are the Spencer-Attix water-to-air stopping powers,  $W_{\text{air}}$  is the mean energy expended in air per ion pair formed,  $P$  represents the perturbation factors for the assumed cavity theory, and  $Q$  and  $Q_0$  represent the beam quality used and the reference quality respectively. Since the  $W_{\text{air}}$  has the same value for therapeutic photon beams, equation can be expressed as:

$$k_{Q,Q_0} \approx \frac{(s_{w,\text{air}})_Q P_Q}{(s_{w,\text{air}})_{Q_0} P_{Q_0}} \quad (2.7)$$

### 2.1.3 Relative Dosimetry: TRS-398/483

Relative dosimetry is used for computing the absorbed dose under non-reference conditions. The quantities involved are the tissue-phantom-ratio (TPR), the tissue-maximum-ratio (TMR), the percent-depth-dose (PDD), the traverse beam profiles and the field output factor (OF) [1]. For the OF, several authors found higher uncertainties in the clinical dosimetry as well as higher discrepancies between Monte Carlo (MC) and measured field output factors [5–7]. Based on the existing data, Alfonso et al. [8] recommended a protocol for measuring the field output factors in non-standard conditions. Starting from the recommended protocol [8] and the report 103 by the Institute of Physics and Engineering in Medicine (IPEM) [9] small radiation fields have been heavily investigated in the last 15 years [9–21]. The published results until 2015 were condensed in a code of practice (COP) and published by Palmans et al. [22].

Small field conditions are present if at least one of the following conditions take place [10, 21, 22]:

1. Lack of lateral charged particle equilibrium.
2. Partial source occlusion.
3. The detector size is or larger than the beam dimensions.

In photon beams the lack of lateral charged particle equilibrium happens if the half width or the radius of the beam is smaller than the range of the most energetic secondary electrons that contribute to the absorbed dose [22]. Based on this condition, the minimum radiation field radius, or half width, will be the value from which the ratio of the absorbed dose to water and the collision kerma in water at the center of the field is equal to 1.

The second condition takes place mainly due to the finite size of the primary photon beam source. When the field size is comparable to, or smaller than the size of the primary photon source, the collimator will block almost all the primary beam causing an overlapping of penumbra from the detector point of view of the detector. Therefore, this effect will produce a reduction in the beam output on the central axis compared to radiation fields that are not partially blocked.

The third condition is known as the detector volume averaging. The signal produced in the detector is proportional to the mean absorbed dose over its sensitive volume, therefore, it will be affected by the homogeneity of the absorbed dose over the detection volume. Since the quantity of interest is the absorbed dose to a point, exposing different sensitive volumes, to the same beam, will have a different output if the detection volume is of a similar size or smaller than the radiation field size.

The absorbed dose to water  $D_{w, Q_{\text{clin}}}^{f_{\text{clin}}}$ , for a clinical field size  $f_{\text{clin}}$  and quality  $Q_{\text{clin}}$ , is related to the absorbed dose to water  $D_{w, Q_{\text{msr}}}^{f_{\text{msr}}}$ , for a machine-specific

reference field size  $f_{\text{msr}}$  of quality  $Q_{\text{msr}}$  as:

$$D_{w, Q_{\text{clin}}}^{f_{\text{clin}}} = D_{w, Q_{\text{msr}}}^{f_{\text{msr}}} \Omega_{Q_{\text{clin}}, Q_{\text{msr}}}^{f_{\text{clin}}, f_{\text{msr}}} \quad (2.8)$$

where  $\Omega_{Q_{\text{clin}}, Q_{\text{msr}}}^{f_{\text{clin}}, f_{\text{msr}}}$  is the OF, and the machine-specific reference field for conventional accelerators is  $10 \times 10 \text{ cm}^2$ . The COP [22] defines this factor as:

$$\Omega_{Q_{\text{clin}}, Q_{\text{msr}}}^{f_{\text{clin}}, f_{\text{msr}}} = \frac{D_{w, Q_{\text{clin}}}^{f_{\text{clin}}}}{D_{w, Q_{\text{msr}}}^{f_{\text{msr}}}} = \frac{M_{Q_{\text{clin}}}^{f_{\text{clin}}}}{M_{Q_{\text{msr}}}^{f_{\text{msr}}}} k_{Q_{\text{clin}}, Q_{\text{msr}}}^{f_{\text{clin}}, f_{\text{msr}}} \quad (2.9)$$

where  $M$  is the detector response corrected by the possible quantities of interest and  $k_{Q_{\text{clin}}, Q_{\text{msr}}}^{f_{\text{clin}}, f_{\text{msr}}}$  is the output correction factor. This factor corrects for the difference of the detector and a small volume of water. Therefore, the output correction factor is defined as[22]:

$$k_{Q_{\text{clin}}, Q_{\text{msr}}}^{f_{\text{clin}}, f_{\text{msr}}} = \left[ \frac{D_{w, Q_{\text{clin}}}^{f_{\text{clin}}} / \overline{D}_{\text{det}, Q_{\text{clin}}}^{f_{\text{clin}}}}{D_{w, Q_{\text{msr}}}^{f_{\text{msr}}} / \overline{D}_{\text{det}, Q_{\text{msr}}}^{f_{\text{msr}}}} \right] \quad (2.10)$$

where  $\overline{D}_{\text{det}, Q_x}^{f_x}$  is the average absorbed dose in the detector sensitive volume. This factor is mainly computed by Monte Carlo (MC) simulations.

## 2.2 Dosimetry Model

Regardless of the type of radiation detector used, there are three main steps involved in a dosimetric detection system. These steps are associated with the energy absorption in the detection volume, the production of the signal and the signal acquisition. Figure 2.2 illustrates the three steps of a dosimetric system.

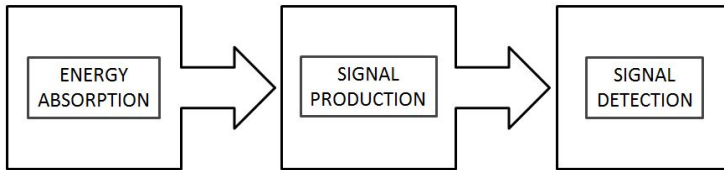


**Figure 2.2:** Illustration of the three steps in a dosimetric detection system

MC simulations of radiation transport are the gold standard for assessing the absorption step. Furthermore, this approach is used for correcting for possible processes in the detector not leading to energy absorption. MC does not take into account the signal production and detection as it is only involved in the first step. However, the MC method relies on the materials involved being well defined, as it needs the stopping powers for computing the deposited energy. Recently,

new recommended values of the ionization potential  $I$ , and the density correction factor  $\delta$ , were published for carbon, air and water in the International Commission on Radiation Units & Measurements (ICRU) report 90 [23]. Table 2.2 shows the

**Table 2.2:** Comparing advantages and disadvantages for ionization chambers and organic plastic scintillators in the three dosimetric steps.

Detector Type	Energy Absorption	Signal Production	Signal Detection
Ionization Chambers	$D_w \neq D_{ion}$ Perturbations $s_{w,air}$ Detector size vs. Point in Water Effective point of measurement Pressure and temperature	$W_{air}$	Recombination losses Leakage
Organic Plastic Scintillators	$D_w \approx D_{scint}$ for MV beams	Ionization quenching Temperature dependance	Stem signal Fiber degradation Signal to noise ratio Optical fiber coupling

behavior of two detectors used in radiotherapy; ionization chambers and organic plastic scintillators. These two detectors were chosen as they are well characterize for reference and relative dosimetry. As shown in table 2.2, ionization chambers have a very good signal production properties but it does not have a good energy absorption or signal detection, therefore it requires more corrections. However, these correction are well controlled and therefore ionization chambers are well characterized. On the other hand, the scintillator behaves almost like water in means of energy absorption, whereas it requires additional corrections step two and three.

The corrections needed when using ionization chambers are well known and described in the COP [1]. In the case of organic plastic scintillators, methods have been developed to correct for the stem signal have been developed [24]. However, no method has been proposed for the correction of the signal production in MV photon beams. In the following section, these two corrections for organic plastic scintillator will be discussed.

## 2.3 Scintillator Dosimetry

### 2.3.1 Ionization Quenching Effect

Birks [25] proposed one of the initial models to describe the light produced by a scintillator. Birks stated that the light production, in the scintillating material, depends on the energy deposition and the nature of the interacting ionizing radiation. It was noticed by Birks in 1951, that variations in the fluorescence response of a scintillator was proportional to the specific energy loss of the interacting

particles. A quantity of interest was the variation of light produced per unit path length as a function of the energy losses. This was described using the 'exciton' theory introduced by Bowen, Mikiewicz, and Smith [26] and states that the electronic energy excited by the ionizing radiation is transferred from molecule to molecule in the crystal. A single molecule therefore captures the transferred energy and light is emitted or quenched depending on the nature of the molecule. Based on that theory, Birks established that when an ionizing particle passes through a scintillating crystal it produces a local concentration of damage or ionized molecules. The damaged molecules quench the excitons and therefore act as quenching agents. The number of produced excitons is proportional to the specific energy loss as well as the concentration of damaged molecules. The specific light yield per unit path is expressed as:

$$\frac{dL}{dx} = \frac{A \frac{dE}{dx}}{1 + kB \frac{dE}{dx}} \quad (2.11)$$

where  $A$  is the number of excitons,  $B$  is the concentration of damaged molecules, and  $k$  is the probability of exciton capture by a damaged molecule relative to an undamaged molecule. The parameters  $k$  and  $B$  are treated as a single parameter,  $kB$ , as it is not possible to measure them independently. This parameter is adjustable and is currently used as a fitting parameter of experimental data. From Birks model, Chou [27] proposed to add a second adjustable parameter in order to get a better fit of the experimental measurements.

$$\frac{dL}{dx} = \frac{A \frac{dE}{dx}}{1 + kB \frac{dE}{dx} + C \left(\frac{dE}{dx}\right)^2} \quad (2.12)$$

Several authors also included the second term for a better fitting of the data [28–30]. Therefore, as discussed by Christensen and Andersen [30], a more generalized way of writing Birks formalism is:

$$\frac{dL}{dx} = \frac{A \frac{dE}{dx}}{1 + kB \frac{dE}{dx} + C \left(\frac{dE}{dx}\right)^2 + \dots} \quad (2.13)$$

where the original Birks model is equation 2.13 truncated in the first term.

In dosimetry, however, the differential light yield per unit path may not be a directly useful quantity. The total light yield produced in a scintillator is a more relevant quantity. Therefore, the total light yield when the electrons are fully stopped in the scintillating volume,  $L(E)$ , is given by:

$$L(E) = \int_0^E \frac{A}{1 + kB L_{\Delta}(E)} dE \quad (2.14)$$

where  $L_{\Delta}(E)$  is the restricted stopping power for an electron with kinetic energy  $E$  and a cut-off energy of  $\Delta$ . Equation 2.14 assumes that the scintillator is sufficiently 'thick' such that an electron with kinetic energy  $E$  will be fully absorbed in

the sensitive volume. Several authors have used equation 2.14 for computing the total light yield in a scintillator with the intention of expressing the scintillator sensitivity [31–33]. This assumption is not completely valid and depends on the energy range and the dimensions of the scintillator. For example, the continuous slowing down approximation (CSDA) range,  $R_{\text{CSDA}}$  for an electron of energy 0.5 MeV in polystyrene is 0.17 cm, therefore, polystyrene-based scintillators with a length less than the  $R_{\text{CSDA}}$  for that specific energy will have particles that will cross the scintillator without being fully absorbed in the sensitive volume.

This situation is usually the case in MV photon dosimetry, in which scintillators are small compared to the  $R_{\text{CSDA}}$  of secondary particles and therefore 'crossers' electrons are able to produce light without being fully absorbed in the scintillator sensitive volume. In order to account for all possible light productions a variation of Birks formalism is proposed in this work. This variation weights all energy depositions in the scintillator from all charged particles that interact in its sensitive volume. The total light yield,  $L(E)$  can be therefore expressed as:

$$L(E) = \sum_{i=1}^n \int_{E_{\min}}^{E_{\max}} \frac{A}{1 + kBL_{\Delta}(E_i)} dE_i \quad (2.15)$$

where  $n$  is the total number of electrons and  $E_{\min}$  and  $E_{\max}$  are the minimum and maximum energies respectively, in the spectrum of electron energy depositions  $dE$  in the scintillating volume.

### 2.3.2 Stem removal: Cerenkov radiation and retarded fluorescence

Cerenkov radiation occurs during irradiation in the optical plastic fiber, which is attached to the scintillator for transport of the scintillator light to a photomultiplier tube (PMT), and can severely jeopardize the light collection in typical MV photon dosimetry. Cerenkov radiation takes place when charged particles passes through a dielectric medium with a velocity higher than the velocity of light in that medium. This phenomenon is well investigated by AS Beddar, Mackie, and Attix [34] for several fiber tubes irradiated with electron beams. Under MV photon beam conditions, Archambault et al. [35] tested several methods of stem signal removal showing that the most efficient method was the chromatic removal proposed by Fontbonne et al. [24]. Several author have extensively used the chromatic removal method yielding a good agreement with expected data [36–42].

The chromatic removal method is able to resolve the light emitted from the optical fiber and the light emitted from the scintillator by using filters of different wavelengths; the blue (*Blue*) of 460 nm and the green (*Green*) of 540 nm. The contribution of these two wave lengths to the absorbed dose follows a linear relationship [24]. In order to convert electrical units to radiological units, a calibration in terms of absorbed dose is needed. Since the Cerenkov radiation

is a function of the energy, the amount of fiber that has been exposed and the incident angle of the radiation [34], two different scenarios are suggested for a chromatic removal Fontbonne et al. [24]:

1. The scintillator is centered in the beam and exposed to a reference field size  $10 \times 10 \text{ cm}^2$ .
2. The scintillator is centered in the beam and exposed to a reference field size  $40 \times 40 \text{ cm}^2$  with several turns of fiber inside the exposed area.

The second condition ensures that more optical fiber is exposed to the radiation field and therefore more Cerenkov radiation will be emitted. The exact amount of turns is not relevant, for a linear system, the only condition to be fulfilled is that more fiber is exposed to radiation.

Since the light produced in the scintillator and the Cerenkov originate from different processes, and the amount of produced light depends on these two effects the absorbed dose in each set-up is given by:

$$D_{1,2} = aGreen_{1,2} + bBlue_{1,2} \quad (2.16)$$

where *Green* and *Blue* represent the scintillator reading for a filtered green and blue wave length,  $a$  is the coefficient for converting from electrical to radiological units and is well known as the gain factor and  $\frac{b}{a}$  is the so called Cerenkov light ratio (CLR). Assuming that the absorbed dose in both conditions are the same, dividing equation 2.16 for the first condition over the same equation for the second condition resulting:

$$CLR = \left[ \frac{Green_1 - Green_2}{Blue_2 - Blue_1} \right] \quad (2.17)$$

For the determination of the gain factor, a detector calibrated in terms to absorbed dose to water is needed. Since this factor is constant between different conditions (same energy) relative measurements can be carried out without the need of a second detector calibrated in terms of dose to water.

### 2.3.3 Temperature Dependence

AS Beddar, Mackie, and Attix [43] reported that organic plastic scintillator have a negligible temperature dependence in temperatures from  $5 \text{ }^\circ\text{C}$  to  $50 \text{ }^\circ\text{C}$ . This study was mainly considering the fact that since the scintillator light comes from decays of excited states to the ground state, the change of the gap between them should be less than 1% around room temperature. However, the author published a correspondence about that work [44] as other studies reported significant changes in the response of organic plastic scintillators when the temperature changes [45]. Buranurak et al. [46] determined the changes in the response of organic plastic scintillators over a temperature range from  $15 \text{ }^\circ\text{C}$  to  $40 \text{ }^\circ\text{C}$ . The

results of that worked showed that the response in organic plastic scintillators can change in 0.55% per °C. Therefore, changes in the response of organic plastic scintillators when changing the temperature in clinical conditions should not be neglected and therefore needs to be corrected for. The model to correct for temperature changes proposed by [46] establishes that for a given temperature  $T$ , the scintillator response  $R(T)$ , can be described by:

$$R(T) = R_0(1 + \alpha(T - T_0)) \quad (2.18)$$

where  $R_0$  is the mean scintillator output at a given dose rate for the reference temperature,  $T_0 = 20$  °C, and  $\alpha$  is the linear temperature coefficient.

## 2.4 Scintillator Application in Small Field Dosimetry

The COP TRS-483 [22] states that the  $k_{Q_{\text{clin}}, Q_{\text{msr}}}^{f_{\text{clin}}, f_{\text{msr}}}$  is assumed to be equal to 1 for organic plastic scintillator. However, corrections for ionization quenching effect were not taken into account in the dataset compiled by this COP. The correction for the ionization quenching effect  $k_{\text{ioq}}$  can be computed using equation 6.6 as:

$$k_{\text{ioq}}^Q = \left[ \frac{L(E)_{kB=0}}{L(E)_{kB \neq 0}} \right]^Q = \left[ \frac{\sum_{i=1}^n \int_{E_{\text{min}}}^{E_{\text{max}}} A dE_i}{\sum_{i=1}^n \int_{E_{\text{min}}}^{E_{\text{max}}} \frac{A}{1+kBL_{\Delta}(E_i)} dE_i} \right]^Q \quad (2.19)$$

This factor corrects for the signal losses due to ionization quenching using Birks model as explained in section 2.3.1 and depends on the beam quality  $Q$ . For ideal organic plastic scintillators this factor is equal to 1. Determining this factor is a very hard task to do, as experimentally there are no ideal scintillator that can be used in order to quantify the losses due to quenching. However, for relative quantities, like the  $k_{Q_{\text{clin}}, Q_{\text{msr}}}^{f_{\text{clin}}, f_{\text{msr}}}$ , this factor can be determined in a combined experimental and MC way for an specific beam quality compared to a reference value. For determining the relative  $k_{\text{ioq}}$  three steps are needed; establishment of the absorbed dose, scintillator measurements and MC simulations of the energy absorption. When using a calorimeter, as explained in section 6.1.5.3, the absorbed dose to the calorimeter core  $D_{\text{core}}$  and the scintillator light yield  $L(E)$ , are related as:

$$\left[ \frac{D_{\text{core}} / L(E)}{D_{\text{core,MC}} / D_{\text{scint,MC}}} \right]_{Q_0}^Q = k_{\text{ioq}Q_0}^Q \quad (2.20)$$

where  $k_{\text{ioq}Q_0}^Q$  is the ionization quenching correction factor from a quality  $Q$  to a quality  $Q_0$ . This factor can then be used for computing the OF by inserting it in equation 2.9:

$$\Omega_{Q_{\text{clin}}, Q_{\text{msr}}}^{f_{\text{clin}}, f_{\text{msr}}} = \frac{M_{Q_{\text{scint,clin}}}^{f_{\text{clin}}}}{M_{Q_{\text{scint,msr}}}^{f_{\text{msr}}}} k_{\text{ioq}Q_{\text{msr}}}^{Q_{\text{clin}}} k_{Q_{\text{clin}}, Q_{\text{msr}}}^{f_{\text{clin}}, f_{\text{msr}}} \quad (2.21)$$

Using equation 2.21 the OF can be computed very precisely and therefore by using the scintillator, as a reference detector, the  $k_{Q_{\text{clin}}, Q_{\text{msr}}}^{f_{\text{clin}}, f_{\text{msr}}}$  can be computed in a clinical environment for several commercially available detectors.

This chapter presents the theoretical framework used in the thesis. The challenges that need to be faced when small fields take place. A three step dosimetric model is used to explain differences between ionization chambers and organic plastic scintillators. Considerations that need to be taken into account, when using fiber-coupled organic plastic scintillators, are explained in details. The advantages of using scintillators for small field dosimetry are highlighted. Finally, how organic plastic scintillator detectors, are used in this thesis, is explained.

## References

- [1] International Atomic Energy Agency. IAEA Technical Report Series No.398. *Atomic Energy* (2000), 1–229.
- [2] PR Almond, PJ Biggs, and WF Hanson. AAPM 's TG – 51 Protocol for Clinical Reference Dosimetry of High-Energy Photon and Electron Beams. *Medical Physics* **26** (1999) (1999), 1–9.
- [3] J Dures and A Ostrowsky. New constant-temperature operating mode for graphite calorimeter at LNE-LNHB. *Physics in Medicine and Biology* **50** (17) (2005), 4035–4052.
- [4] S Picard, DT Burns, and P Roger. Construction of an absorbed-dose graphite calorimeter. *Rapport BIPM* **1** (May) (2009).
- [5] GH Hartmann et al. ORIGINAL PAPER A new method for output factor determination in MLC shaped narrow beams (2007), 58–66.
- [6] IJ Das, GX Ding, and A Ahnesjö. Small fields: nonequilibrium radiation dosimetry. *Medical physics* **35** (1) (2008), 206–215.
- [7] M Heydarian et al. Physics in Medicine & Biology Related content Monte Carlo dosimetry study of a 6 MV stereotactic radiosurgery unit Monte Carlo dosimetry study of a 6 MV stereotactic radiosurgery unit (1998).
- [8] R Alfonso et al. A new formalism for reference dosimetry of small and nonstandard fields. *Medical Physics* **35** (11) (2008), 5179–5186.
- [9] M Aspradakis. Small Field MV Photon Dosimetry. *World Congress on Medical Physics and Biomedical Engineering, September 7-12, 2009, Munich, Germany* **44** (103) (2009), 854–854.
- [10] H Bouchard et al. Detector dose response in megavoltage small photon beams. I. Theoretical concepts. *Medical physics* **6033** (10) (2015), 3700–3710.

- [11] S Kumar et al. Breakdown of Bragg-Gray behaviour for low-density detectors under electronic disequilibrium conditions in small megavoltage photon fields. *Physics in Medicine and Biology* **60** (20) (2015), 8187–8212.
- [12] G Azangwe et al. Detector to detector corrections: A comprehensive experimental study of detector specific correction factors for beam output measurements for small radiotherapy beams. *Medical Physics* **41** (7) (2014).
- [13] A Ralston et al. Over-response of synthetic microDiamond detectors in small radiation fields. *Physics in Medicine and Biology* **59** (19) (2014), 5873–5881.
- [14] P Papaconstadopoulos, F Tessier, and J Seuntjens. On the correction, perturbation and modification of small field detectors in relative dosimetry. *Physics in Medicine and Biology* **59** (19) (2014), 5937–5952.
- [15] H Benmakhlouf and P Andreo. Spectral distribution of particle fluence in small field detectors and its implication on small field dosimetry. *Medical Physics* (2017).
- [16] J Lambert et al. A prototype scintillation dosimeter customized for small and dynamic megavoltage radiation fields. *Physics in Medicine and Biology* **55** (4) (2010), 1115–1126.
- [17] TS Underwood et al. Application of the Exradin W1 scintillator to determine Ediode 60017 and microDiamond 60019 correction factors for relative dosimetry within small MV and FFF fields. *Physics in Medicine and Biology* **60** (17) (2015), 6669–6683.
- [18] P Francescon et al. Variation of  $k_{Qclin}$ ,  $Q_{msr}$   $f_{clin}$ ,  $f_{msr}$  for the small-field dosimetric parameters percentage depth dose, tissue-maximum ratio, and off-axis ratio. *Medical Physics* **41** (10) (2014).
- [19] L Archambault et al. Toward a real-time in vivo dosimetry system using plastic scintillation detectors. *International Journal of Radiation Oncology Biology Physics* **78** (1) (2010), 280–287.
- [20] P Andreo. The physics of small megavoltage photon beam dosimetry. *Radiotherapy and Oncology* **126** (2) (2018), 205–213.
- [21] P Andreo and H Benmakhlouf. Role of the density, density effect and mean excitation energy in solid-state detectors for small photon fields. *Physics in Medicine and Biology* **62** (4) (2017), 1518–1532.
- [22] H Palmans et al. Dosimetry of small static fields used in external beam radiotherapy: An IAEA-AAPM International Code of Practice for reference and relative dose determination. Technical Report Series No. 483. *Iaea TRS-483* (November) (2017).
- [23] ICRU. *ICRU report 90 - Key Data for Ionizing-Radiation Dosimetry: Measurement Standards and Applications*. Vol. 14. 1. 2016, 1–118.

- 
- [24] JM Fontbonne et al. Scintillating fiber dosimeter for radiation therapy accelerator. *IEEE Transactions on Nuclear Science* **49 I** (5) (2002), 2223–2227.
- [25] JB Birks. Scintillation from organic crystals: Specific fluorescence and relative response to different radiation. *Proc. Phys. Soc A* **64** (10) (1951), 874–877.
- [26] EJ Bowen, ET Mikiewicz, and FW Smith. Resonance Transfer of Electronic Energy in Organic Crystals. *Proceedings of the Physical Society. Section A* (1949).
- [27] CN Chou. The Nature of the Saturation Effect of Fluorescent Scintillators. *Phys. Rev.* **87** (5 1952), 904–905.
- [28] L Torrisi. Plastic scintillator investigations for relative dosimetry in proton-therapy. *Nuclear Instruments and Methods in Physics Research, Section B: Beam Interactions with Materials and Atoms* **170** (3) (2000), 523–530.
- [29] LL Wang et al. Determination of the quenching correction factors for plastic scintillation detectors in therapeutic high-energy proton beams. *Physics in Medicine and Biology* **57** (23) (2012), 7767–7781.
- [30] JB Christensen and CE Andersen. Relating ionization quenching in organic plastic scintillators to basic material properties by modelling excitation density transport and amorphous track structure during proton irradiation Relating ionization quenching in organic plastic scintillators to (2018).
- [31] J Boivin et al. A systematic characterization of the low-energy photon response of plastic scintillation detectors. *Physics in Medicine and Biology* **61** (15) (2016), 5569–5586.
- [32] AM Frelin et al. Comparative Study of Plastic Scintillators for Dosimetric Applications. *IEEE Transactions on Nuclear Science* **55** (5) (2008), 2749–2756.
- [33] JF Williamson et al. Plastic scintillator response to low-energy photons. *Physics in Medicine and Biology* **44** (4) (1999), 857–871.
- [34] AS Beddar, TR Mackie, and FH Attix. Cerenkov light generated in optical fibres and other light pipes irradiated by electron beams. *Physics in Medicine and Biology* **37** (4) (1992), 925–935.
- [35] L Archambault et al. Measurement accuracy and Cerenkov removal for high performance, high spatial resolution scintillation dosimetry. *Medical Physics* **33** (1) (2006), 128–135.
- [36] M Guillot et al. Spectral method for the correction of the Cerenkov light effect in plastic scintillation detectors: A comparison study of calibration procedures and validation in Cerenkov light-dominated situations. *Medical Physics* **38** (4) (2011), 2140–2150.

- [37] AM Frelin et al. Spectral discrimination of Čerenkov radiation in scintillating dosimeters. *Medical Physics* **32** (9) (2005), 3000–3006.
- [38] AR Beierholm, LR Lindvold, and CE Andersen. Organic scintillators with long luminescent lifetimes for radiotherapy dosimetry. *Radiation Measurements* **46** (12) (2011), 1982–1984.
- [39] G Azangwe et al. Detector to detector corrections: A comprehensive experimental study of detector specific correction factors for beam output measurements for small radiotherapy beams. *Medical Physics* **41** (7) (2014).
- [40] L Archambault et al. Water-equivalent dosimeter array for small-field external beam radiotherapy. *Medical Physics* **34** (5) (2007), 1583–1592.
- [41] F Therriault-Proulx et al. Technical note: Removing the stem effect when performing Ir-192 HDR brachytherapy in vivo dosimetry using plastic scintillation detectors: A relevant and necessary step. *Medical Physics* **38** (4) (2011), 2176–2179.
- [42] S Buranurak and CE Andersen. Fiber optically coupled radioluminescence detectors: A short review of key strengths and weaknesses of BCF-60 and Al<sub>2</sub>O<sub>3</sub>:C scintillating-material based systems in radiotherapy dosimetry applications. *Journal of Physics: Conference Series* **860** (1) (2017).
- [43] AS Beddar, TR Mackie, and FH Attix. Water-equivalent plastic scintillation detectors for high-energy beam dosimetry: I. Physical characteristics and theoretical considerations. *Physics in Medicine and Biology* **37** (10) (1992), 1883–1900.
- [44] S Beddar. On possible temperature dependence of plastic scintillator response. *Medical physics* **39** (10) (2012), 6522–6522.
- [45] J Lambert et al. In vivo dosimeters for HDR brachytherapy: a comparison of a diamond detector, MOSFET, TLD, and scintillation detector. *Medical physics* **34** (5) (2007), 1759–1765.
- [46] S Buranurak et al. Temperature variations as a source of uncertainty in medical fiber-coupled organic plastic scintillator dosimetry. *Radiation Measurements* **56** (2013), 307–311.



# CHAPTER 3

## Monte Carlo

---

In this chapter, the Monte Carlo based applications used in this thesis are discussed, including a short introduction to Monte Carlo techniques and their use in medicine. The Monte Carlo toolkit EGSnrc has become one of the golden standards for solving the radiation transport equation for energies from 1 keV to 1 GeV. The applications from the EGSnrc toolkit, relevant for this thesis, are described followed by a discussion of their use and implementation. Finally, a validation of the implementations done in EGSnrc is provided..

### 3.1 Introduction

The Monte Carlo (MC) method has been demonstrated to be the most exact method for solving the equation of radiation transport [1, 2]. This mathematical method uses the known dominating probability distributions for each individual particle interaction in a specific media and simulate random trajectories of these individual particles [3, 4]. A particle history describes the path from particle creation until absorption or until it is discarded and will include many individual particle tracks. The MC approach relies on the generated track being completely random, and each individual particle track can be considered independent of the other tracks. Therefore, the physical quantities of interest (e.g. absorbed dose, air kerma, fluence) can be computed by using a large number of histories and extracting the average of these quantities.

By increasing the number of starting particles (histories) the statistics are improved, but at the cost of increased computational time, as the transport equation needs to be solved more times. Acquiring small uncertainties therefore causes long computational times, and as a result, several techniques have been developed for decreasing the computational time [5]. In these techniques, a variation of the statistical weight of particles is utilized and therefore, the physics of the simulation remains the same. These techniques are called variance reduction techniques (VRT) [1], and by implementing these, computations are optimized and become more efficient. The efficiency  $E$ , in MC computations is defined as:

$$\epsilon = \frac{1}{t \times \sigma^2} \quad (3.1)$$

where  $\sigma^2$  is the variance of the simulation and  $t$  is the computational time.

During the past 40 years, the MC method has become a powerful tool in medical physics [3, 4, 6, 7]. Moreover, current radiotherapy dosimetry protocols use data based on MC for computing several corrections needed in dosimetry [8–10]. One of the gold standard MC based software in medical physics is EGSnrc [11]. In the radiotherapy energy range, this software can achieve an uncertainty in absorbed dose computations of less than 0.1%. In this thesis all MC simulations were carried out using this software.

## 3.2 EGSnrc

EGSnrc is a MC based toolkit that was developed at the National Research Council in Canada (nrc) [12]. The acronym 'EGS' stands for electron (and positron) gamma shower, as these are the particles used by the program. The EGSnrc software has several applications that can be used for computing different physical quantities e.g. absorbed dose, fluence, stopping power ratios, to name a few. EGSnrc can simulate particles with kinetic energies from 1 keV up to 1 GeV. The source code of this program is written in `fortran`. However, several applications have been developed in `c++` and included in the program. Furthermore, some `c++` based `ausgab` objects have been developed such that they can run independently of the application. The advantage of such `ausgab` objects (AO) is that they can run with any `c++` based application, and therefore the user can obtain several outputs in one single MC run. The next section discusses different VRT techniques, followed by several sections discussing the relevant EGSnrc applications and their use.

### 3.2.1 Variance Reduction Techniques

EGSnrc has implemented several VRT to make computations more efficient, and these split into two different types: the approximate and the natural VRT. The approximate VRT should be used carefully as they do modify the physics of the simulation, therefore, only natural VRT were used in this work. To apply these techniques, the user defines the VRT factor, causing the statistical weight of particles to change accordingly. By applying these techniques appropriately, a simulation can be more than a thousand times faster for a fixed uncertainty. To find the most efficient way to implement these VRT, equation 3.1 can be used as an indicator: A simulation with a few particles is used for computing the efficiency  $E$ . By changing the VRT factor, the most efficient simulation will provide the preferable VRT factors. In this work only three VRT were used:

directional bremsstrahlung splitting (DBS), Russian Roulette, and photon cross section enhancement.

DBS is implemented in BEAMnrc application. For using this VRT, the user needs to specify a radius  $R_{\text{DBS}}$ , a source-to-surface (SSD)  $SSD_{\text{DBS}}$  distance and the splitting number  $N_{\text{DBS}}$ . When charged particles undergo bremsstrahlung or annihilation events, these events will be split  $N_{\text{DBS}}$  times. The generated photons will have a weight multiplied by  $N_{\text{DBS}}^{-1}$ . If the resulting particle aims to the  $R_{\text{DBS}}$ , the particle is kept otherwise the particle will be subjected to a Russian Roulette game.

The Russian Roulette VRT (also known as the Russian Roulette game) makes the simulation more efficient by killing charged particles that cannot reach the specified volume of interest. The user defines the Russian Roulette number  $N_{\text{RR}}$ . Particles are subjected to this with a survival probability of  $\frac{1}{N_{\text{RR}}}$  when the range is not sufficient to leave the current region or the particle is far away from the cavity. Particles that survive this game will take the statistical weight of those that were killed.

Cross section enhancement is a virtual increase of the photon-cross section by a user defined factor  $N_{\text{cse}}$ . The user also needs to specify the regions in which the technique is applied. To make an efficient usage of this technique, the user needs to create a surrounding volume with a distance to the cavity boundary in the order of the range of secondary particles. With this VRT the probability of creating electrons in the volume of interest is  $N_{\text{cse}}$  times higher. The resulting secondary particles when using this VRT will have a weight multiplied by  $\frac{1}{N_{\text{cse}}}$ .

### 3.2.2 Radiation Source: BEAMnrc

BEAMnrc is an EGSnrc application commonly used to simulate the accelerator or Cobalt machine head. BEAMnrc is based on `mortran` and has several pre-defined geometry modules, called component modules (CM). With the geometrical details of the accelerator's head, it is straightforward to create a model of the head using the CM. BEAMnrc allows the user to score phase space (phsp) files after any CM and continue with further simulations afterwards. The phsp files are planes in which all information about the particles e.g. momentum, energy, position, angular distribution are saved. Figure 3.1 shows a BEAMnrc preview of a typical linear accelerator head. The components above the dashed line is symbolized by the first phsp (phsp 1), and are fixed for any specific energy. This phsp is usually recorded just before the particles go through the collimation system, therefore, the user does not need to re-simulate the input for different field sizes every time. The second phsp (phsp 2) represents the phsp recorded after the collimation system. Usually this phsp is used as the particle source for different applications (as done in this work). The accelerator can be modelled if the company provides the user with the blue prints, describing the specific geometry and materials for the system. Some companies instead of blueprints provide a phsp file recorded

prior to the particles entering the collimation system (as phsp1). The latter is the case for the Varian TrueBeam phps files which are used in this work.

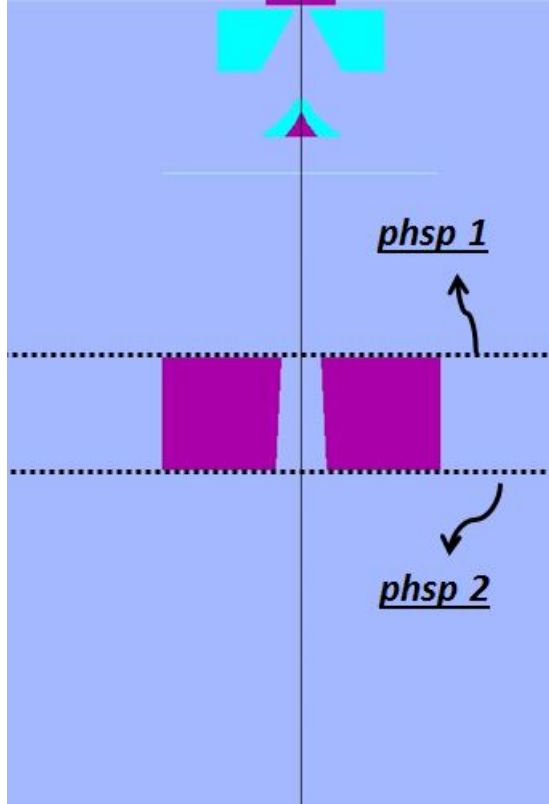


**Figure 3.1:** BEAMnrc view of a typical linear accelerator's head. The dashed lines represent the phase space files scored in these simulations.

The Varian TrueBeam phps files can be downloaded from the official Varian website ([varianforce](http://varianforce.com)). These phsp files were used as the radiation source in the BEAMnrc input file, and only the collimation system needed to be modelled in order to obtain phsp2. The phsp2 were used as the radiation source input files for the `egs_chamber` application (see section 3.2.4) which computes depth dose curves and lateral dose profiles. These two quantities were used to assess the quality of the accelerator model. The used beam qualities are shown in table 3.1.

In this work, fluctuations were observed when computing dose distributions using the Varian TrueBeam phps files. This problem arises as there is an intrinsic variance carried by the phps that cannot be reduced by using VRT. The nature of this problem is related to the density of particles in phsp and is called latent

**Table 3.1:** Beam quality characteristics.

Nominal Beam Energy	4 MV	6 MV	10 MV	15 MV	6 <sup>FFF</sup> MV	10 <sup>FFF</sup> MV
TPR <sub>20,10</sub>	0.620	0.667	0.738	0.762	0.631	0.704

variance (LV). Sempau et al. [13] proposed a formalism for estimating the intrinsic LV of phsp. Several authors have quantified the LV for different Varian TrueBeam phsp files [14, 15]. Alhakeem and Zavgorodni [15] explained that LV of phsp changes with measuring depth and scoring region size. Cronholm and Behrens [14] report that the intrinsic LV of Varian TrueBeam phsp for 4 energies were less than 1%. However, in this work, fluctuations of more than 2% were found in the plateau zone of lateral dose profiles. Therefore, a CM developed by Bush, Zavgorodni, and Beckham [16] was used in order to radially redistribute the particles randomly and consequently reduce the fluctuations in the absorbed dose. This CM was inserted before of the collimation system and therefore a radial redistribution of the particles can be done without changing the output. A critical validation of the phps was carried out as part of this thesis work (see Section 3.2.4).

### 3.2.3 Fluence: cavity and FLURZnrc

In EGSnrc FLURZnrc is the benchmark application for the computation of particle fluence. This application, however, has two main constraints: a geometry constraint and energy bin size constraint. For the geometry, it is only possible to build 2D geometries with a radial symmetry, therefore more complex geometries cannot be simulated using this application. For computation of the fluence, the stopping power is considered constant in the selected energy bin size. This approximation is true, if the energy bin size is sufficiently small. Therefore, for computing the fluence, the user should ensure a high energy resolution. Often, complex geometries and non-radial symmetry are used in experiments. The application cavity computes the fluence of electrons differential in energy in the detector sensitive volume. As it is c++ based, all the c++ libraries can be used for creating more complex geometries. This application enables the computation of the fluence in two ways; FLURZnrc-like and `stpwr`, where comparisons between them can be done. The method `stpwr` takes into account variation of the stopping power inside the selected energy bin.

### 3.2.4 Absorbed Dose and Dose Distributions: `egs_chamber`

The application `egs_chamber` was used to compute the absorbed dose. This application was developed by Wulff, Zink, and Kawrakow [17] and was therefore included in the EGSnrc distribution. In addition to those already available in the `c++` applications, new VRT were developed in the `egs_chamber` application: the photon cross section enhancement, the intermediate phase space, and the correlating sampling. With the combination of these three VRT, the detector perturbation factors can be computed in a more efficient way.

With the inclusion of the `ausgab` object, `egs_dose_scoring`, the absorbed dose to all regions in the simulation can be obtained very efficiently in one single run. This `ausgab` object also allows the computation of the absorbed dose in a voxelized geometry and followingly export an `ascii` file with the 3D dose distribution (`.3ddose`). This `ascii` file can be read and the isodose curves extracted. This `ausgab` object with a voxelized geometry was used for the validation of the `phsp` files.

To validate the `phsp` files, the voxel size was chosen to be  $0.1 \times 0.1 \times 0.1 \text{ cm}^3$  yielding a volume of  $V = 0.001 \text{ cm}^3$ . The resolution of the voxel was selected to be very small as the main application of this thesis is small field dosimetry (see section 2.1.3). As pointed out by Alhakeem and Zavgorodni [15] the LV of `phsp` files depends on the size of the scoring volume. Therefore, a selection of such small volume will provide a pessimistic representation of the model. This will ensure that the effects of fluctuations when computing absorbed dose in small scoring volumes are not overlooked. For the validation, the depth dose and off-axis dose profiles were compared with values extracted from smoothed curves used to feed the Varian Eclipse treatment planning system (TPS). The off-axis lateral dose profile was computed at 10 cm depth for all beam qualities.

Figure 3.2 and 3.3 show the depth dose and the off-axis dose profiles, respectively, for the used `phsp` (see table 3.1) as well as the relative discrepancies between the computed values and the values used in the Eclipse TPS. Figure 3.2 shows that for all beam qualities but the flattening free, the discrepancies are less than 2%, for points above the depth with the maximum dose ( $d_{\max}$ ). However, for all beam qualities the discrepancies at 10 cm and 20 cm depths are less than 2%. Since the beam qualifier,  $\text{TPR}_{20,10}$ , is related to the ratio of the absorbed dose at those two depths [8], therefore, the low discrepancies ensure that the spectrum obtained in both MC and the experiments are very similar. For the off-axis lateral dose profiles, all relative discrepancies are less than 1% in the plateau region, whereas for the shoulder of the profiles as well as for the penumbrae, discrepancies higher than 5% were found. The computations carried out in this work calculates the absorbed dose in the center of the beam. Therefore the contribution to the profile from the shoulders and the penumbrae is very small. Moreover, a comparison between the Monte Carlo computed and the experimentally determined  $\text{TPR}_{20,10}$  is shown in table 3.2. The relative discrepancies for all beam qualities are less than 1%, and the model is considered to be in good agreement with the

experimental data.

**Table 3.2:** Comparison between experimental and Monte Carlo beam qualities

Nominal Energy	Experimental	MC	uncertainty	rel. Disc (%)
4MV	0.620	0.6195	0.00124	0.160
6FFF	0.631	0.62785	0.00117	0.568
6MV	0.667	0.66622	0.00114	0.112
10FFF	0.704	0.70052	0.00112	0.561
10MV	0.738	0.73974	0.0012	-0.212
15MV	0.762	0.75472	0.00125	0.943

### 3.2.5 Collision Kerma: `egs_kerma` and `g`

The application `egs_kerma` and therefore a validation against a benchmark application was carried out in this work. Three physical quantities can be computed by this application: the collision kerma,  $K_{\text{col}}$ , the photon fluence differential in energy and the total photon fluence. The  $K_{\text{col}}$  is computed by scoring the photon fluence in a specified cavity and multiplying by its energy and mass energy absorption coefficients ( $\frac{\mu_{\text{en}}}{\rho}$ ). To make the computation process more efficient, an ascii file with the pre-computed  $\frac{\mu_{\text{en}}}{\rho}$  is needed. The same procedure is used in other EGSnrc applications such as `egs_brachy` or `egs_fac`.

The  $\frac{\mu_{\text{en}}}{\rho}$  are computed using the user code `g` which also computes the  $K_{\text{col}}$  for several materials. `g` was therefore used to validate the `egs_kerma` application as it is considered the benchmark. The validation was carried out in 2 parts: first the photon fluence is validated against `FLURZnrc` and second the  $K_{\text{col}}$  is validated against `g`. A geometry was constructed in `egs_kerma` with a radial symmetry for computing the photon fluence, and the same procedure was applied in `FLURZnrc`. An air cylinder (0.1 cm of thickness and 2 cm of diameter) was placed in air and exposed to a parallel 0.5 MeV photon beam of 3 cm radius. The photon energy fluence differential was computed and compared using both methods. Then the spectrum obtained by `FLURZnrc` was used to compute  $K_{\text{col}}$  in `g`. The resulting  $K_{\text{col}}$  was compared with the result from the `egs_kerma` application.

Figure 3.4 shows the computed energy photon fluence differential using the two applications, `egs_kerma` and `FLURZnrc`. The computed fluences are in excellent agreement, as is seen from Table 3.3. For both the total photon fluence and the collision kerma, the relative discrepancies between the two applications are less than 0.165%, and the `egs_kerma` application is considered validated.

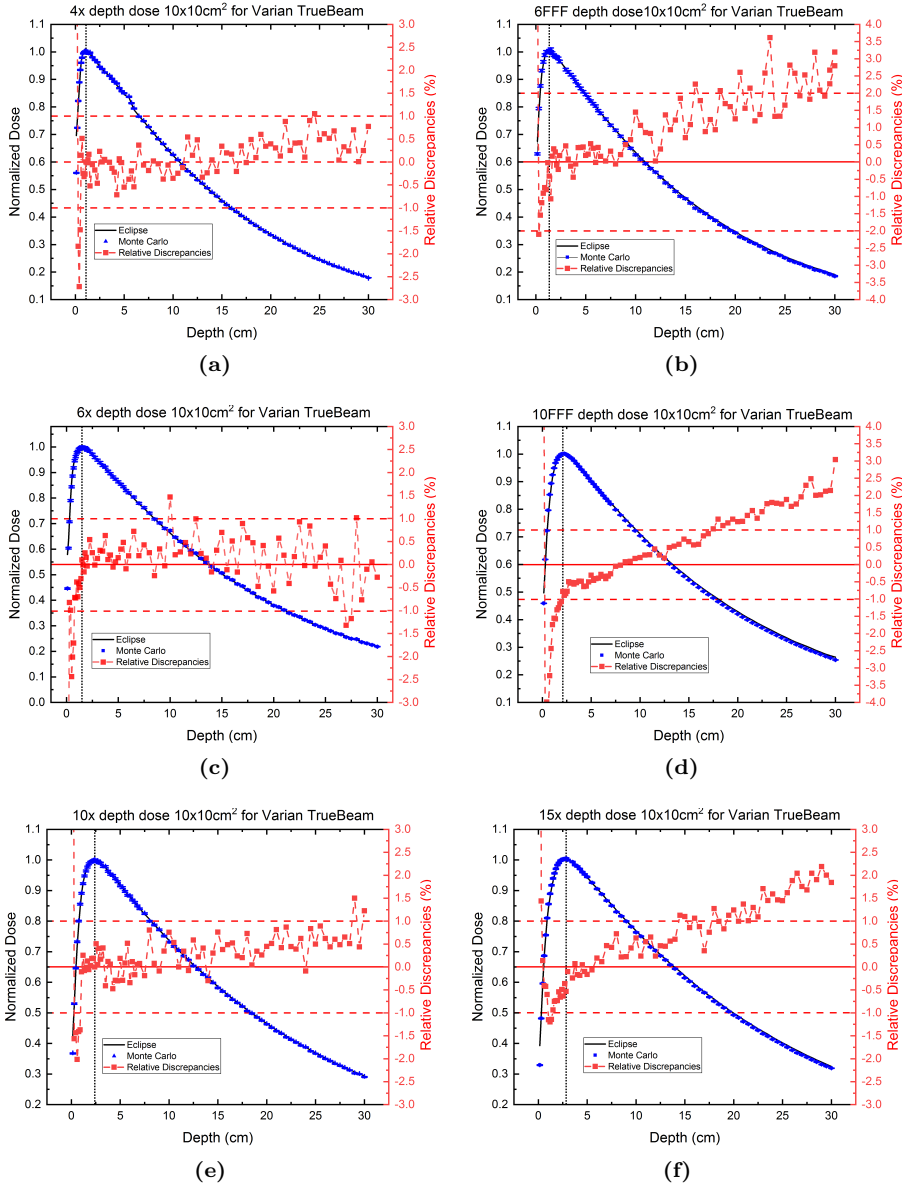
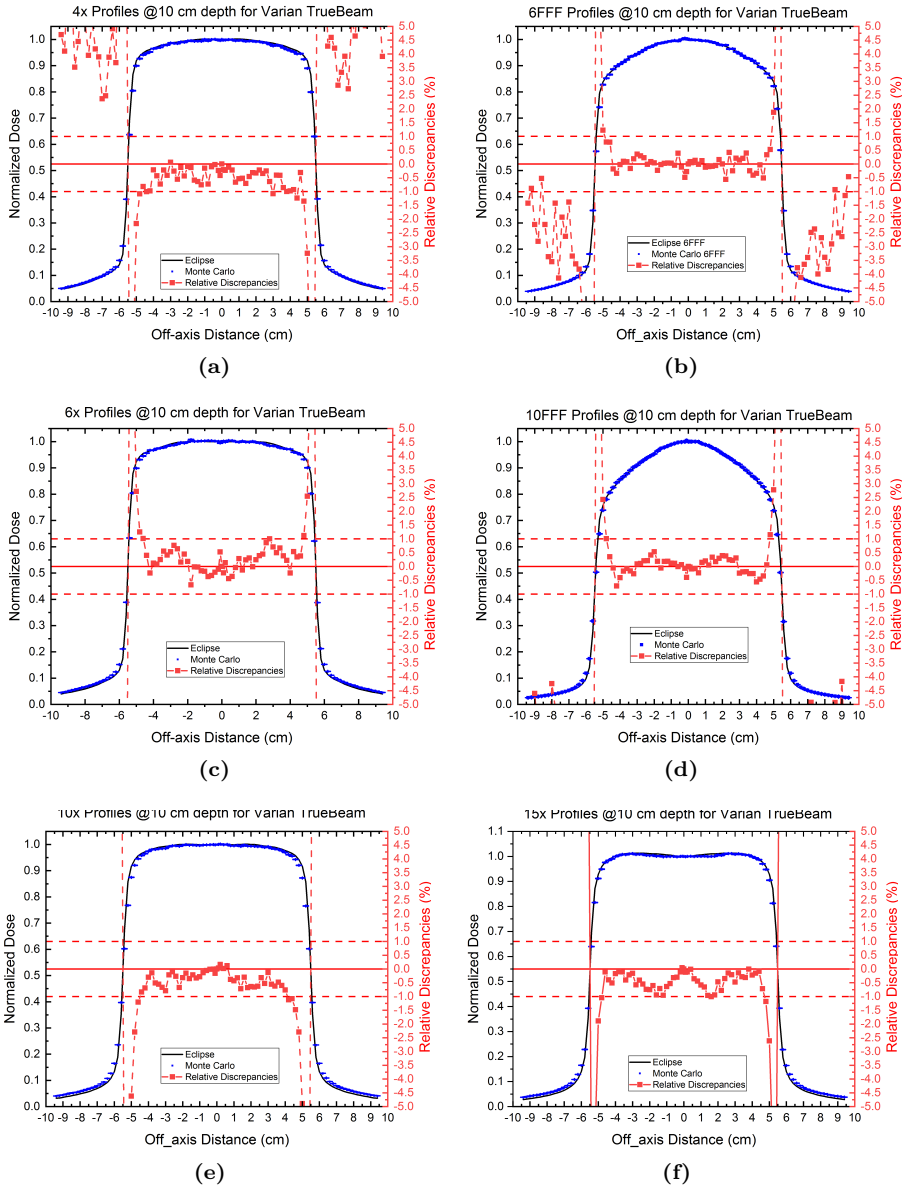
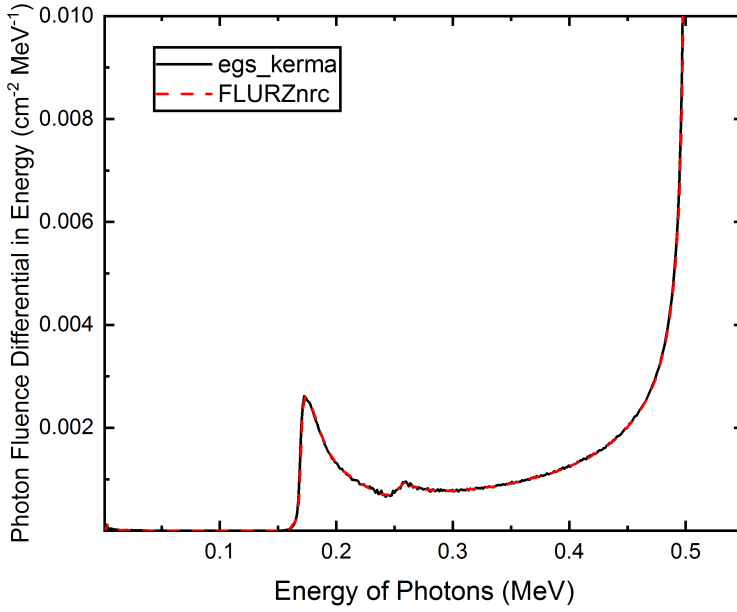


Figure 3.2: Depth dose profiles for different phps files.



**Figure 3.3:** Off-axis lateral dose profiles for different phsp files.



**Figure 3.4:** Photon fluence computed by `egs_kerma` and `FLURZnrc`

**Table 3.3:** Comparison between `egs_kerma` and `FLURZnrc`.

Quantities	<code>egs_kerma</code>	<code>FLURZnrc</code>	Discrepancies (%)
Total Photon Fluence	$0.99016 \pm 0.001 \%$	$0.9896 \pm 0.002 \%$	0.057
Collision Kerma	$2.35\text{E-}12 \pm 0.001 \%$	$2.35\text{E-}12 \pm 0.03 \%$	0.165

### 3.2.6 Light Yield and Cumulative Absorbed Dose per Electron Energy: `egs_light_scoring` & `egs_cum_dose_scoring`

Two `ausgab` objects were developed in order to score the relative light yield produced in a scintillator and the cumulative absorbed dose per electron energy; `egs_light_scoring` and `egs_cum_dose_scoring` respectively. These two `ausgab` objects are based on `egs_dose_scoring` `ausgab` object which is available in EGSnrc. Figure 3.5 shows how the `ausgab` objects are declared in input file of the `c++`-based application. As seen from figure 3.5 the `ausgab` objects are declared in the `ausgab` objects block in the input file.

```

:start ausgab object definition:

: start ausgab object:
  library = egs light scoring
  name = light yield in scintillator
  medium dose = no
  region dose = yes
  volume = 0.00157 # in cm3
  dose regions = 4
  normalization = 1
  kB = 0.019 # Ionization Quenching Parameter (MeV*cm-1)
: stop ausgab object:

: start ausgab object:
  library = egs dose scoring
  name = Cumulative absorbed dose till 1 MeV
  medium dose = no
  region dose = yes
  volume = 0.00157 # in cm3
  dose regions = 4
  normalization = 1
  C.D = 1 # Threshold of the electron energy in the spectrum
: stop ausgab object: # for computing the absorbed dose (MeV)

: stop ausgab object definition:

```

**Figure 3.5:** `Ausgab` Objects declaration

Two `ausgab` objects were developed in order to score the relative light yield produced in a scintillator and the cumulative absorbed dose per electron energy: `egs_light_scoring` and `egs_cum_dose_scoring` respectively. These two `ausgab` objects are based on `egs_dose_scoring` `ausgab` object, which is available in EGSnrc. Figure 3.6 shows how the `ausgab` objects are declared in the `objects` block in the input file of the `c++`-based application.

The `egs_cum_dose_scoring` AO introduces a variable, D.C, compared to `egs_dose_scoring`, which computes the cumulative absorbed dose. In the AO, a binary weighting function is declared. If the energy of the electrons inside the cavity are less than the value of C.D, the function takes the value 1, if not, it takes the value 0. The variable C.D can be interpreted as the upper energy limit

of the electron spectrum in which the absorbed dose will be computed. Moreover, if the energy of the electrons is higher than the selected C.D energy value, then that particle will not deposit its energy in the sensitive volume. Figure 3.6 shows a spectral representation of the C.D variable (the C.D was chosen to be 1 MeV in this example). The absorbed dose will then be computed by the AO using the electron spectrum up until the specified C.D energy value. By introducing several C.D energies, a cumulative absorbed dose curve can be obtained for the whole spectrum in the sensitive volume.

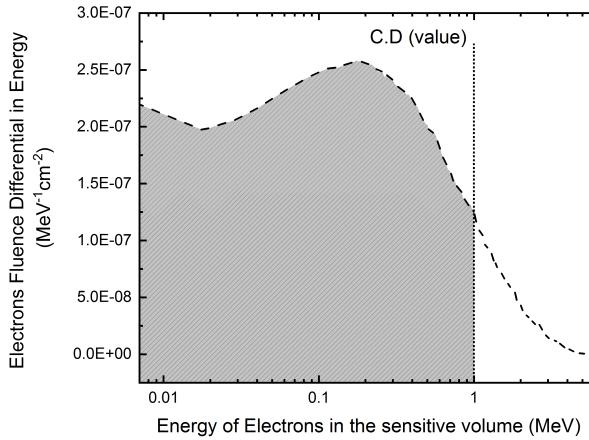


**Figure 3.6:** Cumulative absorbed dose output object representation.

The `egs_light_scoring` launches a variable  $kB$  which is the ionization quenching parameter (see section 2.3.1). This AO weights all the energy depositions using Birks formalism as explained in chapter 2 equation 6.6. The use of different  $kB$  values allows the user to obtain several relative light yield, and to fit the obtained values with experimental data. If  $kB$  is set to 0, the relative light yield will be as if the scintillator is 'ideal' i.e. as no quenching occurs. The validation of this AO was performed against an analogue approach of computing the light yield. In addition, computation of the light yield and comparison with published experimental data was also carried out. How to create `egs_light_scoring` AO from `egs_dose_scoring` AO can be found in the appendix A of this thesis.

Two tests were performed in order to validate the `egs_light_scoring` AO; AO: a test against the analogue approach of solving Birks equation, and a test against published experimental data. For both tests, a phantom sufficiently big was simulated in order to ensure that all the delivered energy was deposited in the phantom. Mono-energetic electron beams emitted by an isotropic point source placed in the center of the phantom were used as the radiation source. Several

energies from 10 to 600 keV. were used. The ratio of the light yield to the deposited energy was computed for the beam energies used. Figure 3.7 shows a comparison for both approaches.

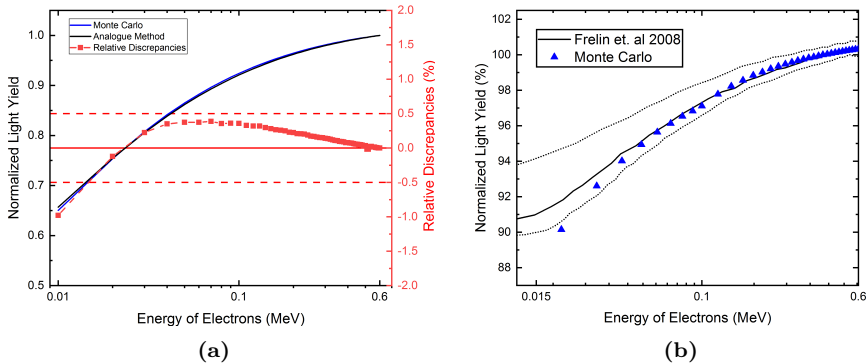


**Figure 3.7:** Validation of `egs_light_scoring` against an analogue computation method (a) and published experimental measurements (b)

The relative discrepancies between the analogue method and the Monte Carlo based method are less than 0.95% for all energies. The figure shows that with the increase in energy both methods converge to the same value. Higher discrepancies are observed for lower energies, as the resolution of the energy bin for computing the light yield in the analogue method was 1 keV. Since the shape of the stopping power changes abruptly for small energy changes, the value of stopping power within 1 keV in the low energy range change a few %. Therefore, a discrepancy of approximately 1% is expected. To compare with published experimental data, the data was digitized and extracted from Frelin et al. [18] (see figure 10 for UPS-974) but a direct relative comparison of discrepancies between values was not performed. However, the computed MC values are within the uncertainty for all energies above 20 keV. In Frelin et al. [18], the author observed an inflection of the data for very low energies due to the high sensitivity of the experimental system for low energy.

Figure 3.7 shows a good agreement between the implemented Monte Carlo-based method of computing the light yield, both the expected and the experimentally determined. Therefore, the `egs_light_scoring` is considered validated.

## References

- [1] T Jenkins, W Nelson, and A Rindi. *Monte Carlo transport of electrons and photons*. Ettore Majorana international science series: Physical sciences. Plenum Press, 1988.

- 
- [2] F Verhaegen and J Seuntjens. Monte Carlo modelling of external radiotherapy photon beams. *Physics in medicine & biology* **48** (21) (2003), R107.
  - [3] P Andreo. Monte Carlo Techniques in Medical Radiation Physics. **36** (7) (1991), 861–920.
  - [4] DW Rogers, M Carlo, and M Carlo. The Role of Monte Carlo Simulation of Electron Transport in Radiation Dosimetry. **42** (1991).
  - [5] D Sheikh-bagheri et al. Monte Carlo Simulations : Efficiency Improvement Techniques and Statistical Considerations (Mc) (2006), 71–91.
  - [6] P Andreo. Monte Carlo simulations in radiotherapy dosimetry. *Radiation Oncology* **13** (1) (2018), 121.
  - [7] D Rogers. Fifty years of Monte Carlo simulations for medical physics. *Physics in Medicine & Biology* **51** (13) (2006), R287.
  - [8] International Atomic Energy Agency. IAEA Technical Report Series No.398. *Atomic Energy* (2000), 1–229.
  - [9] PR Almond, PJ Biggs, and WF Hanson. AAPM ’ s TG – 51 Protocol for Clinical Reference Dosimetry of High-Energy Photon and Electron Beams. *Medical Physics* **26** (1999) (1999), 1–9.
  - [10] H Palmans et al. Dosimetry of small static fields used in external beam radiotherapy: An IAEA-AAPM International Code of Practice for reference and relative dose determination. Technical Report Series No. 483. *Iaea TRS-483* (November) (2017).
  - [11] I Kawrakow. Accurate condensed history Monte Carlo simulation of electron transport. I. EGSnrc, the new EGS4 version. **485** (2000) (2000).
  - [12] I Kawrakow et al. *The EGSnrc code system: Monte Carlo simulation of electron and photon transport*. Tech. rep. PIRS-701. National Research Council Canada, 2017.
  - [13] J Sempau et al. Monte Carlo simulation of electron beams from an accelerator head using PENELOPE. *Physics in Medicine & Biology* **46** (4) (2001), 1163.
  - [14] R Cronholm and C Behrens. OC-0436: On the latent variance of the vendor supplied TrueBeam phase space files. *Radiotherapy and Oncology* **106** (2013), S168.
  - [15] E Alhakeem and S Zavgorodni. Evaluation of latent variances in Monte Carlo dose calculations with Varian TrueBeam photon phase-spaces used as a particle source. *Physics in Medicine & Biology* **63** (1) (2017), 01NT03.
  - [16] K Bush, S Zavgorodni, and W Beckham. Azimuthal particle redistribution for the reduction of latent phase-space variance in Monte Carlo simulations. *Physics in Medicine & Biology* **52** (14) (2007), 4345.

- 
- [17] J Wulff, K Zink, and I Kawrakow. Efficiency improvements for ion chamber calculations in high energy photon beams. *Medical Physics* **35** (4) (2008), 1328–1336.
- [18] AM Frelin et al. Comparative Study of Plastic Scintillators for Dosimetric Applications. *IEEE Transactions on Nuclear Science* **55** (5) (2008), 2749–2756.



## CHAPTER 4

# Paper 1 (Submitted to Radiation and Measurements)

---

### **Evaluation of the ionization quenching effect in organic plastic scintillators using kV x-rays and a modified Birks model with explicit account of secondary electrons**

#### **Abstract**

Organic plastic scintillators are attractive for several applications in medical dosimetry due to their high degree of water equivalence and their minimal perturbation of the radiation field. There is, however, a non-proportionality between the produced scintillation light and the absorbed energy for electrons below about 125 keV. This ionization quenching can be described by Birks formalism. In this work, an improved version of Birks formalism was developed. The model explicitly accounts for the light yield from secondary electrons and the model therefore can take advantage of the detailed electron spectra computed by Monte-Carlo techniques. The use of the model is demonstrated by comparison of modelling results and scintillator measurements of air kerma in a series of well-characterized, low energy x-rays beams with generating potentials from 60 kV to 300 kV (mean photon energies from 38 to 158 keV). The new model predicted the scintillator light production in good agreement with the experimental data. The model opens up for improved evaluations of the influence of quenching losses in MV photon beam dosimetry and other medical applications.

## 4.1 Introduction

Organic plastic scintillators have been widely used for medical applications in the last decade [1–5] mainly driven by their high degree of water equivalence and their minimal perturbation of the radiation field in megavoltage radiotherapy beams [6, 7]. These attractive features are rooted in the similarity between water and the scintillator base material (for example polystyrene) with respect to electronic density and atomic composition [6, 7]. However, a non-proportionality between the scintillator signal and the deposited energy has been observed for electrons below approximately 125 keV [8–10] and for heavy charge particles [11, 12]. This non-proportionality of the scintillator light production is also known as ionization quenching [13].

Ionization quenching is commonly described by the semi-empirical, unimolecular model proposed by Birks [13]. In this model, the light yield of the scintillator depends on the ionization density of the charged particles expressed by the stopping power of the particles in question. The model introduces an ionization quenching parameter ( $kB$ ), also known as Birks parameter, which quantifies the relation between light production and stopping power.

Several authors have evaluated ionization quenching effects for different materials using the Birks formalism applied to electrons [3, 9, 10, 14, 15] under simplifying assumptions, such as that the electrons stop completely in the scintillating material or that the scintillator behaves as a large cavity detector [3, 9]. These simplifying assumptions hinder the evaluation of ionization quenching in sub-mm sized scintillators used for megavoltage radiotherapy dosimetry.

In this paper, we therefore developed an extended version of Birks formalism that applies to the full spectrum of charged particles (both primaries and secondaries) without further assumptions. We implemented the quenching model in an application of the Monte Carlo based software EGSnrc [16], and we demonstrated the use of the code by extraction of quenching parameters upon comparing modelling results with scintillator measurements in well-characterized kV x-ray beams subject to detailed Monte-Carlo modelling of radiation transport.

## 4.2 Materials and Methods

### 4.2.1 Organic Plastic Scintillator

The organic plastic scintillator (diameter = 1 mm, length = 2 mm) was a BCF-60 polystyrene-based scintillating fiber (Saint Gobain, France) with a green (530 nm) wavelength emission. It was attached to a 15 m long polymethylmethacrylate (PMMA) ESKA Premier GH4001-P optical fiber cable (1 mm diameter, Mitsubishi, Japan). The scintillator light was recorded with an ME40 (DTU Nutech, Denmark) in-house developed instrument containing H5784 photo multiplier tubes (Hamamatsu, Japan). This system has been used [4, 17, 18] previously

and compared with the commercially available scintillator system W1 (Standard Imaging, USA) [19].

Figure 4.1 shows the geometrical as well as the material composition of the scintillator. For simplicity and to focus on details, only 1 cm of the optical fiber is shown.

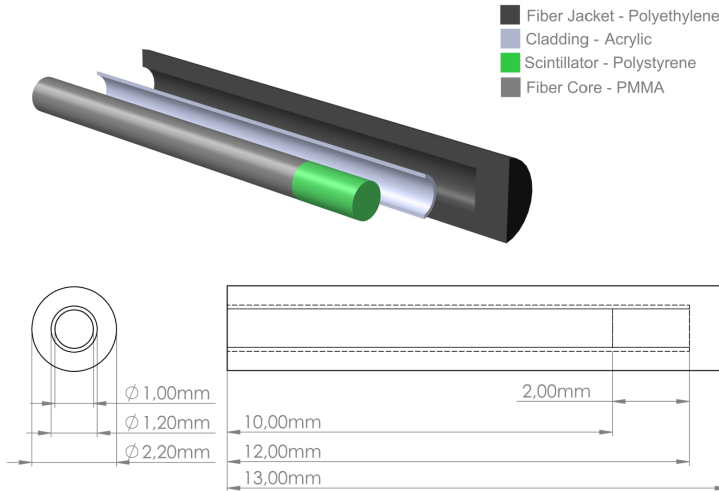


**Figure 4.1:** Geometrical and material composition of the organic plastic scintillator.

## 4.2.2 Radiation Source and measurements

The scintillator was exposed to 11 different medium-energy x-rays beams made available at the Italian National Metrology Institute of Ionizing Radiation (ENEA-INMRI) which acts as Primary Standard Laboratory. The beams were provided by a Titan Isovolt 450 x-rays bipolar tube (General Electric, USA). The half-value layer (HVL) of each x-ray beam quality was experimentally determined, whereas the mean energy of each beam was estimated using a software that simulates continuous x-ray spectra [20]. Table 4.1 shows the characteristics as well as the added filtration for each beam.

The air kerma was established with the Italian Primary Standard of air kerma at medium energy x-rays, an Attix-Type Victoreen model 451 free-air chamber. For each irradiation, the ionization current readings from a commercially available transmission-type monitor chamber (PTW model TB786) were used to both control for the influence of possible fluctuations of the x-ray tube output, and as a means to transfer the quantity air kerma which is established when using the primary standard. The degree of equivalence of the ENEA primary stan-

standard and other international primary standards of air kerma measurements in medium-energy x-ray beams is available on the BIPM key-comparison database and in [21]. Figure 4.2 shows the set-up of the experiment for irradiation with the organic plastic scintillator.

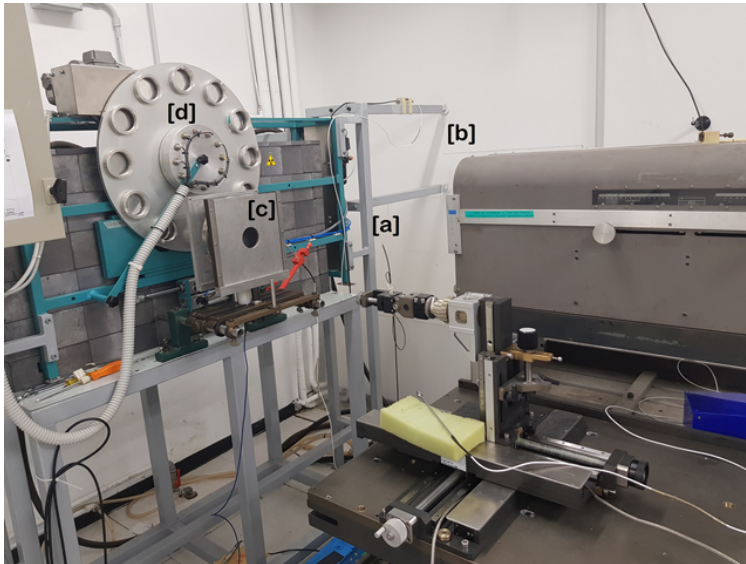


**Figure 4.2:** Experimental set-up. The organic plastic scintillator is positioned at the reference distance (a). The free-air ionization chamber off the beam (b). The transmission-type monitor chamber, in a sandwich made with a set of two collimators (c). The carousel with some of the x-rays filtration used (d).

The measurements were carried out in runs of 90 seconds. First, the air kerma was established at the reference distance of 100 cm from the x-rays tube, using the Attix-type chamber. A correspondence was set between the monitor chamber current reading and the air kerma rate as determined using the Attix-type chamber, which dimensionally is similar to an air-kerma calibration coefficient. For irradiations of the scintillator, the total irradiation time was divided into three integration times of 30 seconds each. The procedure was repeated three times in order to obtain the desirable uncertainty. After the kerma in air was established, the monitor chamber was calibrated for that specific beam quality. As a third step, the scintillator was positioned at the reference distance. Finally the air kerma was re-established and therefore any variations on the output of the tube are accounted for in the uncertainty budget. The PMT gain was set to be 0.7 for all the beam qualities. The integration time was set according to the beam quality in order to avoid the saturation of the charge collection.

As described by Williamson et al. [10] and Boivin et al. [15] the sensitivity of

the scintillator  $\epsilon_\lambda^{\text{meas}}$  when exposed to a beam of quality  $\lambda$  can be obtained by:

$$\epsilon_\lambda^{\text{meas}} = \left[ \frac{(I_{\text{scint}} - I_{d,\text{scint}}) - (I_{\text{fiber}} - I_{d,\text{fiber}})}{\dot{K}_{\text{air}}} \right] \quad (4.1)$$

where  $I_{\text{scint}}$  is the current generated in the scintillator during irradiation and  $I_{d,\text{scint}}$  is the background or dark current generated without irradiations. The Cerenkov and fluorescence signals are removed by subtracting the current generated when the scintillator is out of the radiation beam i.e. the fiber is the one being irradiated, and its respective background ( $(I_{\text{fiber}} - I_{d,\text{fiber}})$ ). The  $\dot{K}_{\text{air}}$  is the air kerma rate established by the free in air ion chamber .

The nominator of equation 4.1 is the light yield of the scintillator and is related to the dose as:

$$\epsilon_\lambda^{\text{meas}} = [L_{\text{det}}/K_{\text{air}}]_\lambda^{\text{meas}} = \alpha_\lambda [D_{\text{det}}/K_{\text{air}}]_\lambda^{\text{MC}} \quad (4.2)$$

where  $\alpha_\lambda = [L_{\text{det}}/D_{\text{det}}]$  is the inherent sensitivity of the scintillator. This parameter relates to the physical processes that lead to the absorption. Differences between the light yield of the scintillator and the absorbed dose are associated to the quenching effect. The term inside the brackets in the right part of the equation is the ratio between the absorbed dose to the scintillator and the air kerma in an air volume of the same size of the sensitive volume of the scintillator. This term is realized by Monte Carlo computations.

**Table 4.1:** Beam quality characteristics. RQR are Radiodiagnostic Quality Radiation beams defined in the IAEA report TRS-457, the CCRI qualities are defined by [22], and the H qualities are from the high dose-rate series from the ISO4037-1 norm.

Beam Quality	Experimental		Extracted from Spectrum			
	Dose rate (mGy s <sup>-1</sup> )	Added Filtration (mm Al or mm Cu)	HVL1 (mm Al or mm Cu)	HVL1 (mm Al or mm Cu)	$E_{\text{mean}}$ (keV)	HVL ratio <sup>1</sup>
RQR5	1.921	3.19 (Al)	2.6 (Al)	2.56 (Al)	40.1	1.016
RQR6	2.549	3.39 (Al)	3.02 (Al)	2.98 (Al)	43.9	1.013
RQR7	3.161	3.57 (Al)	3.47 (Al)	3.43 (Al)	47.4	1.012
RQR8	3.385	3.7 (Al)	3.95 (Al)	3.86 (Al)	50.5	1.023
RQR9	3.887	4.13 (Al)	4.98 (Al)	4.87 (Al)	56.3	1.023
RQR10	3.94	4.72 (Al)	6.54 (Al)	6.35 (Al)	63.8	1.030
CCRI135	2.563	2.225 (Al) + 0.23 (Cu)	0.487 (Cu)	0.472 (Cu)	67.2	1.032
CCRI180	2.354	3.16 (Al) + 0.49 (Cu)	0.978 (Cu)	0.988 (Cu)	84.3	0.990
H200	1.898	4.26 (Al) + 1.11 (Cu)	1.614 (Cu)	1.65 (Cu)	101	0.978
H250	2.134	4.18 (Al) + 1.63 (Cu)	2.443 (Cu)	2.51 (Cu)	122	0.973
H300	2.026	4.0 (Al) + 2.48 (Cu)	3.34 (Cu)	3.43 (Cu)	147	0.974

<sup>1</sup>Ratio between the experimental HVL and the HVL extracted from the spectrum.

### 4.2.3 Computed spectra

The SpekCalc software was used to generate the primary photon beam [20, 23]. This software used a semi-analytical model based on a deterministic model for tungsten anode over the tube potentials of the range of 40-300 kVp and anode angles from 6 to 30 degrees. The user defines the maximum energy, the minimum energy, anode angle and the thickness of each of the materials that are present in the filter. From the generated spectrum the first and second HVL as well as the mean energy of the spectrum can be extracted. The extracted first HVL values and, where available, the second HVL were compared with the experimental values as a validation of the simulated spectrum. The extracted HVL as well as the mean energy of each spectra are shown in Table 4.1.

### 4.2.4 Light Yield Analysis

The production of light by electrons traversing a thin slab of scintillator material can be described by the semi-empirical model proposed by Birks [13]:

$$\frac{dL}{dx} = \frac{A \frac{dE}{dx}}{1 + kB \frac{dE}{dx}} \quad (4.3)$$

where  $dL$  is the light yield for a single primary electron per unit of path length  $dx$  in the scintillating material with the ionization density (e.g. expressed as the total, unrestricted stopping power  $\frac{dE}{dx}$ ), and where  $A$  is the scintillator efficiency and  $kB$  is a quenching parameter. Ideally, these two model parameters ( $A$  and  $kB$ ) are constant such that the quenching for a specific scintillator can be described over a wide range of irradiation conditions.

The above model equation implicitly assumes that the scintillator is sufficiently "thick" such that  $dL$  includes both the light from the primary electron moving  $dx$  and the light from all the secondaries set in motion during that step. In this manuscript, we extend the application of Birks law to explicitly account for secondary electrons. This means that  $dL$  is now the light yield for each individual electron regardless if its primary or secondary without contributions from new secondaries produced during the step  $dx$ . In this modified version of Birks law we use the restricted stopping, with a threshold  $\Delta = 1$  keV, as a measure of ionization density ( $\frac{dE}{dx}$ ). This extension facilitates the application of Birks law for Monte-Carlo computed electron spectra as described in the next session. This approach allows a detailed evaluation of quenching for situations where the scintillator is thin compared with the range of the secondary electrons or when the scintillator is used for dosimetry under conditions where there is no charge-particle equilibrium.

The new model specifically computes the light emitted,  $L$ , by all primary and

secondary electrons crossing (or stopping in) the scintillator as:

$$L = \sum_{i=1}^n \int_{E_{\min}}^{E_{\max}} \frac{A}{1 + kB L_{\Delta}(E_i)} dE_i \quad (4.4)$$

where  $n$  is the total number of electrons,  $L_{\Delta}(E)$  is the restricted stopping power for an electron with kinetic energy  $E$ , and  $E_{\min}$  and  $E_{\max}$  are the minimum and maximum energies in the spectrum of electron energy depositions  $dE$  in the scintillating volume.

## 4.2.5 Monte Carlo computations

The Monte Carlo-based software EGSnrc was used for the computations of the inherent sensitivity of the scintillator [16]. The main used applications were `egs_chamber` [24], `cavity` and `egs_kerma`. The latter is not distributed yet in the EGSnrc distribution package and is a simplified version of `cavity`. An `ausgab` object was developed for computing the light yield. This `ausgab` object based on the current `egs_dose_scoring` available in the distribution of EGSnrc works with all the applications based on C++.

The developed `ausgab` object; `egs_light_scoring` takes into account every deposition of charged particles by weighting them according to the Birks formalism as shown in equation 4.4. This approach accounts for every charged particle energy deposition inside the scintillating sensitive volume and no assumption of full absorption is required. The user defines the quenching parameter.

The collision air kerma was obtained by using the application `egs_kerma`. This quantity is determined by computing the photon fluence differential in energy and multiplying it by the mass energy-absorption coefficients. The same procedure is done in the `cavity` application but only for 2D geometries.

The `cavity` application was used to score the charged-particle fluence in the scintillator sensitive volume. Since charged-particles are responsible for the absorbed dose, it is extremely of high importance to obtain the charged-particle spectrum in which the scoring volume is exposed to.

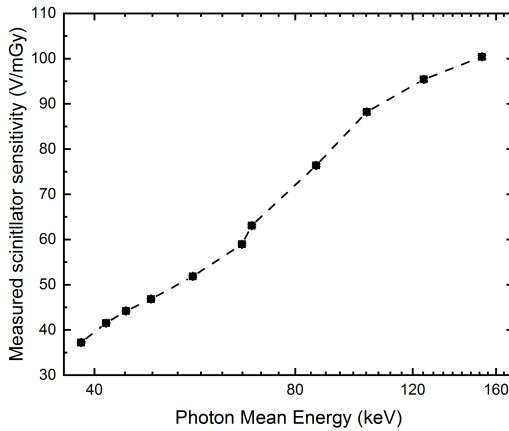
A parallel beam with the spectra computed by SpekCalc was used as a radiation source for all the computations. The beam was set with circular shape with 10 cm of diameter. The cut-off energies as well as the secondary threshold was set to be the lowest possible in EGSnrc; 1 keV. The transport parameters were chosen to be the default ones except for the photon cross section that was set to be the re-normalized cross sections [25] as it is the main photon interaction process in this energy range. The Russian Roulette and the cross section enhancement were used as variance reduction techniques for the computation of the absorbed doses and the light yields.

## 4.3 Results

### 4.3.1 Scintillator measurements

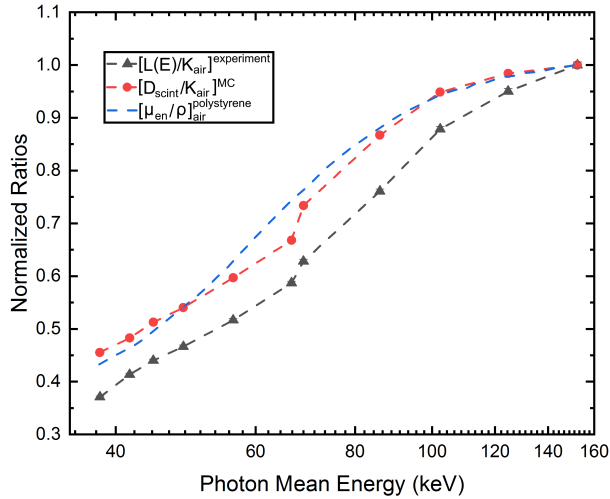
The measured sensitive of the scintillator is shown in figure 4.3. For all the measurements, the contribution from the dark current and the signal from the exposed fiber cable (i.e. the stem signal) was found to be less than 6% of the scintillator signal recorded by the instrument. The uncertainty of the scintillator measurements were estimated to be less than 2%. The uncertainty in the determination of the air kerma was less than 0.38%. The data show that the sensitivity increases with beam energy. Since the ratio of the mass absorption coefficients for polystyrene to air is flat for energies above 150 keV, it is expected that the sensitivity has reached linearity with respect the energy.

Figure 4.4 shows the ratios obtained by measurements and Monte Carlo normal-



**Figure 4.3:** Measured scintillator sensitive for different x-rays qualities

ized to the higher energy. The black triangles represent the measured sensitivity  $\epsilon_{\lambda}^{\text{meas}}$ . The red circles represent the conversion of air kerma, in absence of the scintillator, to the absorbed dose to the scintillator sensitive volume identified by Monte Carlo. The dash blue lines represent the ratio of mass absorption coefficients for polystyrene to air of mono-energetic beams that cover the energy range of interest. This ratio was included in the plot as it has been widely used in the literature for determining the absorbed dose in the scintillator [3, 15, 26]. The figure shows that both the ratio of absorbed dose to the conversion factor as well as the mass attenuation coefficients are higher than the measured sensitivity. The differences between the sensitivity and the conversion factor decrease as the mean energy of the beam quality increases.



**Figure 4.4:** Normalized ratios for different x-rays qualities. The measured sensitivity (black triangles), Monte Carlo conversion factors (red circles) and the mass energy absorption coefficients (dashed blue lines).

### 4.3.2 Spectra

The photon normalized fluence inside the bare volume of air, as well as the electronic normalized fluence inside the scintillator sensitive volume, for the three used x-rays series table 4.1, are shown in figure 4.5. The figure shows the variety of spectra shapes for the different x-rays series. For the photon normalized fluences the characteristic x-rays of tungsten are well captured in the spectrum. The electronic fluence showed high variability with respect to the spectrum shape and the mean energy. However, the series H showed more consistency between them than the other used x-rays series.

### 4.3.3 Light Yield

The light yield using different  $kB$  parameter values for all the used beam qualities are shown in figure 4.6. The pattern area represents the uncertainty of the experimental measurements. The uncertainties of all the computations were less than 0.25%. In the uncertainty of the experimental measurements, differences between the experimental HVL and the HVL extracted from SpekCalc were taken into account. Therefore, there is a higher contribution to the uncertainty from the conversion of air kerma to absorbed dose in the scintillator.

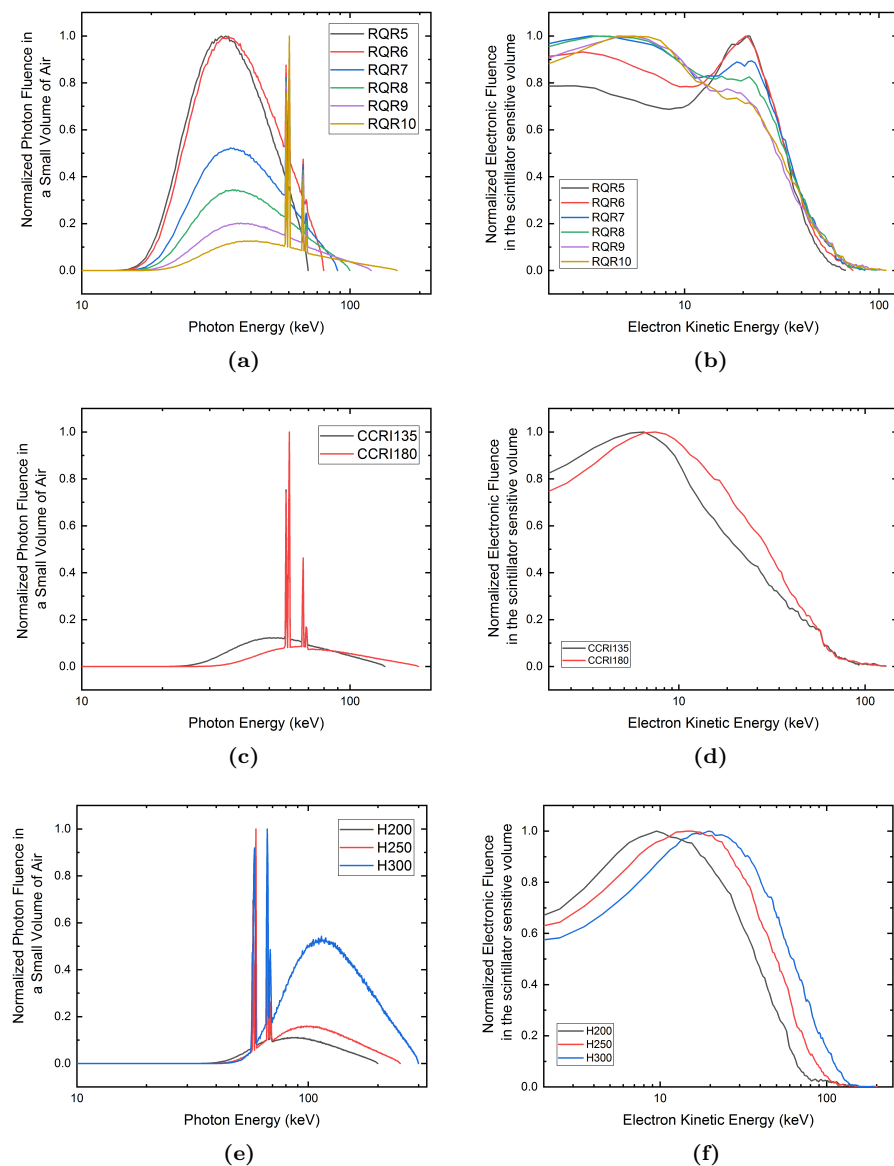


**Figure 4.5:** Normalized fluence of photons in a small volume of air and electrons in the scintillator sensitive volume for the three different used x-rays series; RQR(a,b), CCRI(c,d) and H(e,f).

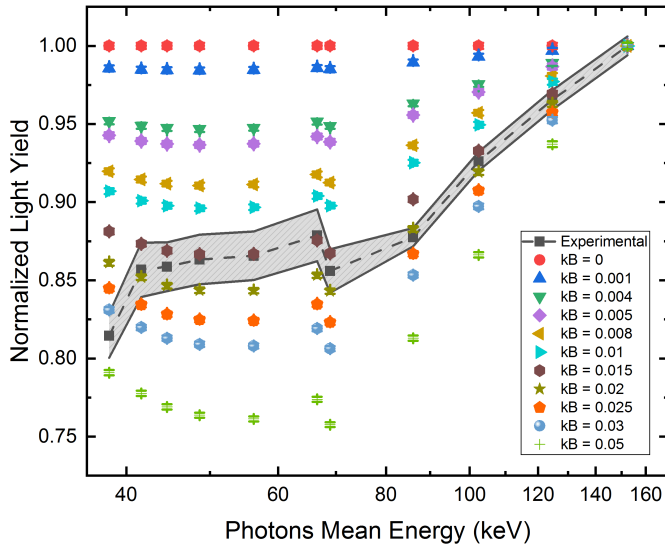


**Figure 4.6:** Normalized light yield for different quenching parameters ( $kB$ ) and the experimental measurements corrected by Monte Carlo.

## 4.4 Discussion

The data show that the method implemented for computing the light yield based on Monte Carlo is a more realistic way to tackle the ionization quenching effect compared to studies carried out so far [3, 15]. This method relies only on the spectrum of charged particles and applies the Birks model to explain all the energy depositions that do not lead to signal production. Approximations such as full absorption of the electrons in the scintillator, usage of mono-energetic photon beams, and used of large cavity theory [10, 14, 15, 27] are not required in this model. Therefore, a more "realistic" quenching investigation was carried out in the present work. An important feature of the new approach is that it will allow for the evaluation of the influence of quenching in MV-photon dosimetry where it cannot be assumed that the secondary electrons stop within the sub-mm sized scintillator. An example where this is relevant is for evaluation of the influence of ionization quenching on scintillator-based field output factor measurements in small MV photon beams [28].

Differences of up to 8%, between the two commonly used ways of computing the conversion factors, can be seen in figure 4.4. The mass attenuation coefficients are computed for mono-energetic beams whereas the absorbed dose to the scintillator as well as the collision air kerma are computed for the specific spectrum of that beam quality.

The electronic spectra computed in the scintillator cavity was found to be

extremely different for the same x-rays quality series. However, for the more energetic series; H, the spectra have the same shape and the differences are purely due to the energy. In all cases more than the 90% of the spectra are shifted towards the very low energy. It was found that for beam qualities with a very similar mean energy, the electronic spectrum inside the cavity can be very different. Since the energy depositions are made by electrons, neither the mean energy of photons nor the first HVL are a good indicator of the beam quality.

The conversion factor from air kerma to absorbed dose to the scintillator seems to be more sensitive to lower than to higher energies. Figure 4.6 shows that the uncertainty bars are bigger the lower the energy. From the beam quality with mean energy 84 keV (CCRI-180), the changes in the HVL are less significant for the conversion factor. The Birks model provides a good fit to the data. All the data points can be described by one unique  $kB$  parameter, but the lowest energy beam quality, within uncertainties. The  $kB$  value that fits the data better is between  $0.015$  and  $0.02$   $\text{cm MeV}^{-1}$ .

A breakdown of the Birks model has been observed by Boivin et al. [15] reporting different  $kB$  values for different mean photon beam energies. In this work we found that the mean energy of the photon beam is not a good descriptor of the beam. Moreover, there is no direct relationship between the mean energy of the photon beam and the electron spectrum scored in the scintillator cavity. Therefore the variations in the  $kB$  should be reported against electron energy as they are the responsible of the ionization quenching. A range of  $kB$  values have been reported in the literature;  $0.0005$  to  $0.094$   $\text{cm MeV}^{-1}$  for polystyrene-based scintillators [10, 14, 27]. The  $kB$  value obtained in the present work is in agreement with the range observed in the literature.

## Conclusions

A more generalized method, based on Birks formalism, has been developed for describing the ionization quenching effect for organic plastic scintillators. Unlike previous studies in the literature, this method uses the full spectrum of charged particles and the restricted lineal electronic stopping power. We demonstrated how this model can be used, and we found that with a detailed Monte Carlo modelling of the experimental situation, we could account for the measured scintillator response over the range of energies from 38 to 158 keV. An important feature of the new approach is that it will allow for the evaluation of the influence of quenching in MV-photon dosimetry where it cannot be assumed that the secondary electrons stop within the sub-mm sized scintillator.

## Acknowledgement

This work was supported by the Danish Council for Independent Research (grant FTP, DFF-4184-00151). Special thanks to Ernesto Mainegra for the help with Monte Carlo simulations.

## References

- [1] F Therriault-Proulx, S Beddar, and L Beaulieu. On the use of a single-fiber multipoint plastic scintillation detector for  $^{192}\text{Ir}$  high-dose-rate brachytherapy. *Medical Physics* **40** (6) (2013).
- [2] TS Underwood et al. Application of the Exradin W1 scintillator to determine Ediodo 60017 and microDiamond 60019 correction factors for relative dosimetry within small MV and FFF fields. *Physics in Medicine and Biology* **60** (17) (2015), 6669–6683.
- [3] F Lessard et al. Validating plastic scintillation detectors for photon dosimetry in the radiologic energy range. *Medical Physics* **39** (9) (2012), 5308–5316.
- [4] P Sibolt et al. Time-resolved plastic scintillator dosimetry in a dynamic thorax phantom. *Radiation Measurements* **106** (2017), 373–377.
- [5] E Simiele et al. Spectral characterization of plastic scintillation detector response as a function of magnetic field strength. *Physics in Medicine & Biology* **63** (8) (2018), 085001.
- [6] AS Beddar. Water equivalent plastic scintillation detectors in radiation therapy. *Radiation Protection Dosimetry* **120** (1-4) (2006), 1–6.
- [7] MA Clift, RA Sutton, and DV Webb. Water equivalence of plastic organic scintillators in megavoltage radiotherapy bremsstrahlung beams. *Physics in Medicine and Biology* **45** (7) (2000), 1885–1895.
- [8] S Non-proportionality et al. Design of a Facility for Measuring. **55** (3) (2008), 1753–1758.
- [9] AM Frelin et al. Comparative Study of Plastic Scintillators for Dosimetric Applications. *IEEE Transactions on Nuclear Science* **55** (5) (2008), 2749–2756.
- [10] JF Williamson et al. Plastic scintillator response to low-energy photons. *Physics in Medicine and Biology* **44** (4) (1999), 857–871.
- [11] LL Wang et al. Determination of the quenching correction factors for plastic scintillation detectors in therapeutic high-energy proton beams. *Physics in Medicine and Biology* **57** (23) (2012), 7767–7781.

- [12] J Brage Christensen et al. Quenching-free fluorescence signal from plastic-fibres in proton dosimetry: Understanding the influence of Čerenkov radiation. *Physics in Medicine and Biology* **63** (6) (2018).
- [13] JB Birks. Scintillation from organic crystals: Specific fluorescence and relative response to different radiation. *Proc. Phys. Soc A* **64** (10) (1951), 874–877.
- [14] L Peralta and F Rêgo. Response of plastic scintillators to low-energy photons. *Physics in Medicine and Biology* **59** (16) (2014), 4621–4633.
- [15] J Boivin et al. A systematic characterization of the low-energy photon response of plastic scintillation detectors. *Physics in Medicine and Biology* **61** (15) (2016), 5569–5586.
- [16] I Kawrakow. Accurate condensed history Monte Carlo simulation of electron transport. I. EGSnrc, the new EGS4 version. **485** (2000) (2000).
- [17] AR Beierholm, LR Lindvold, and CE Andersen. Organic scintillators with long luminescent lifetimes for radiotherapy dosimetry. *Radiation Measurements* **46** (12) (2011), 1982–1984.
- [18] G Azangwe et al. Detector to detector corrections: A comprehensive experimental study of detector specific correction factors for beam output measurements for small radiotherapy beams. *Medical Physics* **41** (7) (2014).
- [19] AR Beierholm, CF Behrens, and CE Andersen. Dosimetric characterization of the Exradin W1 plastic scintillator detector through comparison with an in-house developed scintillator system. *Radiation Measurements* **69** (2014), 50–56.
- [20] GG Poludniowski. Calculation of x-ray spectra emerging from an x-ray tube. Part II. X-ray production and filtration in x-ray targets. *Medical Physics* **34** (6Part1) (2007), 2175–2186.
- [21] DT Burns, C Kessler, and JP Mccaffrey. Key comparison BIPM.RI(I)-K3 of the air-kerma standards of the ENEA, Italy and the BIPM in medium-energy x-rays. **48** (2014), 1–15.
- [22] CCEMRI(I). Qualités de rayonnement (1972), R15–R16.
- [23] GG Poludniowski and PM Evans. Calculation of x-ray spectra emerging from an x-ray tube. Part I. Electron penetration characteristics in x-ray targets. *Medical Physics* **34** (6Part1) (2007), 2164–2174.
- [24] J Wulff, K Zink, and I Kawrakow. Efficiency improvements for ion chamber calculations in high energy photon beams. *Medical Physics* **35** (4) (2008), 1328–1336.
- [25] L Sabbatucci and F Salvat. Theory and calculation of the atomic photoeffect. *Radiation Physics and Chemistry* **121** (2016), 122–140.

- 
- [26] AS Beddar, TR Mackie, and FH Attix. Cerenkov light generated in optical fibres and other light pipes irradiated by electron beams. *Physics in Medicine and Biology* **37** (4) (1992), 925–935.
- [27] AM Frelin et al. Comparative Study of Plastic Scintillators for Dosimetric Applications. *IEEE Transactions on Nuclear Science* **55** (5) (2008), 2749–2756.
- [28] H Palmans et al. Dosimetry of small static fields used in external beam radiotherapy: An IAEA-AAPM International Code of Practice for reference and relative dose determination. Technical Report Series No. 483. *Iaea TRS-483* (November) (2017).



## CHAPTER 5

# Paper 2 (Submitted to Radiation and Measurements)

---

## **Quantifying the ionization quenching effect in organic plastic scintillators used in MV photon dosimetry**

### **Abstract**

Miniature organic plastic scintillators attached to optical fiber cables have found important uses in medical dosimetry, in particular for small-field dosimetry and field output factor measurements in megavoltage linear accelerator beams. Plastic scintillators are well suited for these applications due to their high degree of water equivalence and their small size. Plastic scintillators, however, are known to suffer from ionization quenching, meaning that the light production per absorbed dose decreases if the dose deposition is caused by low energy electrons. As MV beams also lead to dose deposition by low energy electrons, ionization quenching will also affect, for example, field output factor measurements in MV beams if the fraction of dose delivered by low energy electrons changes with field size or beam quality. While the influence of ionization quenching on scintillator dosimetry in beams of heavy charge particles or kV x-ray has been subject to much research, the effect in MV beams is less well studied, and it is often implicitly assumed that there is no effect. The purpose of this work therefore was to quantify the influence of ionization quenching on plastic scintillators, specifically BCF-60, for the two application in MV photon dosimetry: (i) field output factor measurements for field sizes from

$0.5 \times 0.5 \text{ cm}^2$  to  $10 \times 10 \text{ cm}^2$  for a 6 MV beam and (ii) ionization chambers beam quality correction factor ( $k_Q$ -factors) measurements for beams between 4 MV and 15 MV at a fixed  $10 \times 10 \text{ cm}^2$  field size. The quenching was quantified using Monte Carlo modelling of the MV beams, a variation of Birks formalism that accounted for the detailed dose deposition by secondary electrons, and quenching parameters established previously using experiments in kV x-ray beams. This enabled the computation of the light yield in a "quenching free" scintillator and therefore a computation of a correction factor due to ionization quenching. Ionization quenching was found to have a small but statistically significant influence on both of the studied applications:  $(0.6 \pm 0.2)\%$  for the field output factor measurements between  $0.5 \times 0.5 \text{ cm}^2$  and  $10 \times 10 \text{ cm}^2$  and about  $(2 \pm 0.4)\%$  for the  $k_Q$ -factor application for beams between 4 MV and 15 MV. The modelling results were in agreement with experimental measurements. The results support that the ionization quenching effect has a small effect on field-output factor measurements and it can probably be neglected during clinical measurements. For direct scintillator-based measurements of beam quality correction factors for ionization chambers, ionization quenching is larger and this effect needs to be accounted for if anyone wants to measure or verify ionization chamber  $k_Q$ -factors using organic plastic scintillators.

## 5.1 Introduction

Fiber-coupled organic plastic scintillators have found important uses in medical dosimetry [1, 2], in particular for small-field dosimetry and field output factor measurements in megavoltage linear accelerator beams [3–7] and in-vivo dosimetry during radiotherapy [8–10]. Two key features of organic plastic scintillators are their small size (1 mm characteristic dimension) and their high degree of water-equivalence with respect to atomic composition and electron density. These features mean that in MV photon beams, organic plastic scintillators are virtually perturbation free as they interact with the radiation field much like water. There will therefore be little difference between the absorbed dose to a scintillator and to a small water voxel placed in the same position in a water phantom without any detector [11–13]. This is of particular importance for small field dosimetry where the charge-particle equilibrium is not fully established, and organic plastic scintillators can therefore potentially be used to determine the output correction factor of other detectors in such non-reference irradiation configurations [4, 14]. In line with this, the Technical Series Report 483 (TRS-483) [7] by the International Atomic Energy Agency (IAEA) and AAPM (American Association of Physicists in Medicine) can therefore prescribe the output correction factor for organic plastic detectors in MV photon beams to be equal to unity for small radiation fields.

Accurate fiber-coupled organic plastic scintillator dosimetry, however, requires control of some of the less ideal features of these detectors. The scintillator signal

changes with temperature [15, 16], but the influence of this will be neglectable by application of a simple temperature correction or by maintaining a constant temperature during the measurement session. The main issue of scintillator dosimetry is to separate the scintillator light from the undesirable stem signal produced in the optical cable by the primary beam and scattered radiation [17, 18]. This stem signal is a combination of fluorescence and Cerenkov radiation, that can be accounted for by different experimental approaches such as the chromatic removal, temporal gating, simple filtration among others [18–21]. Finally, there is the problem that plastic scintillators are known to suffer from ionization quenching, which is the subject of the present work.

Ionization quenching is the phenomenon that the scintillator light production per absorbed dose decreases when the dose deposition is caused by charged particles with a higher ionization density. As an example, this means that low energy electrons (e.g. below 125 keV) will tend to produce less light per absorbed dose than high energy electrons (e.g. above 1 MeV). As MV beams also lead to dose deposition by low energy electrons, ionization quenching will also affect field output factor measurements in MV beams if the fraction of dose delivered by low energy electrons changes with field size or beam quality.

While the influence of ionization quenching on scintillator dosimetry in beams of heavy charge particles or kilovoltage x-ray has been subject to much research [22–28], the effect in MV beams is less well studied, and it is often implicitly assumed that there is no effect [7]. The purpose of this work therefore was to quantify the influence of ionization quenching on plastic scintillators for two potentially important applications in MV photon dosimetry: (i) field output factor measurements for field sizes from  $1 \times 1 \text{ cm}^2$  to  $10 \times 10 \text{ cm}^2$  for a 6 MV beam and (ii) ionization chambers beam quality correction factor ( $k_Q$ -factors) for beams between 4 MV and 15 MV at a fixed  $10 \times 10 \text{ cm}^2$  field size. The used organic plastic scintillator was made of BCF-60 (Saint Gobain fiber) fiber as it has been used in several studies for MV photon dosimetry [3, 4, 6, 8, 9]. The study is based on detailed Monte Carlo modelling of the MV beams, Birk’s formalism and quenching parameter previously obtained for this scintillator material. Moreover, experimental measurements were carried out in order to validate the Monte Carlo computations.

## 5.2 Materials and Methods

### 5.2.1 Formalism

#### 5.2.1.1 Beam Quality Correction Factor for Ionization Chambers

For reference dosimetry in MV photon beams, the IAEA [29] recommends ionization chambers to be used for establishing the dose in the clinic. An important feature of ionization chambers are their high degree of stability and from that

perspective they are ideal as transfer instruments between calibration laboratories and end users. Air-filled ionization chambers, however, require correction for the beam quality, even for reference conditions where charge-particle equilibrium is nearly fully developed. The IAEA therefore defines a beam quality correction factor,  $k_{Q,Q_0}$ , that can be used to predict the calibration coefficient  $N_{D,w,Q}$  for a beam quality  $Q$  from a calibration coefficient  $N_{D,w,Q_0}$  obtained for a beam quality  $Q_0$ :

$$k_{Q,Q_0} = \frac{N_{D,w,Q}}{N_{D,w,Q_0}} = \frac{D_{w,Q}/M_Q}{D_{w,Q_0}/M_{Q_0}} \quad (5.1)$$

where  $D_w$  represents the absorbed dose to a point in water and  $M$  is the detector reading. Calibration laboratories provide the calibration coefficient at beam quality  $Q_0$  which is normally either  $^{60}\text{Co}$  or linear-accelerator MV photon beams of a defined quality.

Given their high-degree of water equivalence, organic plastic scintillators may potentially be used to validate the consistency of ionization chambers  $k_{Q,Q_0}$ -factors. In this work, we test this hypothesis. To facilitate this work we apply the concept of  $k_{Q,Q_0}$  for ionization chambers also to scintillators in a straightforward manner. The  $k_{Q,Q_0}$  for scintillators includes corrections for energy absorption properties of the scintillator material, the detector perturbation and ionization quenching.

## 5.2.2 Field Output Factor

To convert from the established dose under reference conditions to smaller field sizes, hospitals need small detectors. As small fields often involve measurements far from charge-particle equilibrium, these detectors require significant corrections to give the correct value. The recent IAEA/AAPM code of practice [7] defines the output factor  $\Omega_{Q_{\text{clin}},Q_{\text{msr}}}^{f_{\text{clin}},f_{\text{msr}}}$  (OF) and how it can be obtained from the detector response,  $M$  using tabulated correction factors,  $k_{Q_{\text{clin}},Q_{\text{msr}}}^{f_{\text{clin}},f_{\text{msr}}}$ :

$$\Omega_{Q_{\text{clin}},Q_{\text{msr}}}^{f_{\text{clin}},f_{\text{msr}}} = \frac{D_{w,Q_{\text{clin}}}^{f_{\text{clin}}}}{D_{w,Q_{\text{msr}}}^{f_{\text{msr}}}} = \frac{M_{Q_{\text{clin}}}^{f_{\text{clin}}}}{M_{Q_{\text{msr}}}^{f_{\text{msr}}}} k_{Q_{\text{clin}},Q_{\text{msr}}}^{f_{\text{clin}},f_{\text{msr}}} \quad (5.2)$$

where  $M$  is the detector response corrected for basic influencing factors,  $Q$  represents the beam quality,  $f$  represents the field size, and indices clin and msr are the clinical and the machine-specific reference beams, respectively. The machine-specific reference field size is a  $10 \times 10 \text{ cm}^2$  field for conventional linear accelerators.

This IAEA/AAPM code of practice [7] states that the output correction factor for a polystyrene-based organic plastic scintillator is equal to unity under the implicit assumption that ionization quenching does not change with field size. According to this code of practice, field output factors can therefore be acquired

directly as the ratio of the absorbed dose to the scintillator sensitive volume for clinical and the reference field sizes.

### 5.2.3 Light Yield

The light yield [30] produced in the scintillator was theoretically estimated by using a Monte Carlo based variation of Birks formalism [31]. This variation uses the full spectrum of secondary particles (i.e primary and secondaries) for the estimation of the light yield. This approach was previously validated, for BCF-60 organic plastic scintillators, using kV x-rays beams [31]

Birks [30] relates the light yield  $dL$  per path unit length  $dx$  with the ionization density  $dE/dx$  as:

$$\frac{dL}{dx} = \frac{A \frac{dE}{dx}}{1 + kB \frac{dE}{dx}} \quad (5.3)$$

where  $A$  is the scintillator efficiency and  $kB$  is the quenching parameter. Using the proposed approach [31], light yield produced in the scintillator  $L(E)$  can be computed as:

$$L(E) = \sum_{i=0}^n \int_{E_{min}}^{E_{max}} \frac{A}{1 + kB L_{\Delta i}} dE_i \quad (5.4)$$

where  $n$  represents the number of charged particles interacting in the scintillator sensitive volume,  $E_{min}$  and  $E_{max}$  are the minimum and maximum energy of the these particles that deposit energy along the scintillator sensitive volume and  $L_{\Delta}$  is the restricted linear electronic stopping power with an energy  $\Delta$  cut-off value.

### 5.2.4 Ionization Quenching Correction Factor

As discussed in the introduction, the ionization quenching effect is caused by processes not leading to a signal production [2]. This problem is magnified for very low energy electrons that have a high electronic stopping power. Regardless the energy range of the problem in question, there will always be a non negligible contribution to the dose from those low energy electrons. The ionization quenching correction factor  $k_{ioq}$  can be therefore defines as:

$$k_{ioq} = \left[ \frac{L(E)_{ideal}}{L(E)_{quench}} \right]^{f_{clin, Q_{clin}}} \quad (5.5)$$

where  $L(E)_{quench}$  and  $L(E)_{ideal}$  represent the scintillator light yield as defined in equation 5.4 with and without quenching effect, respectively, and  $f_{clin}$  represents the clinical field size for a beam quality  $Q_{clin}$ . This parameter corrects for those processes that do not lead to light production.

### 5.2.5 Experimental set-up

A Varian TrueBeam linear accelerator, available at the Technical University of Denmark (DTU) dosimetry laboratory, was used as a radiation source. Table 5.1 shows the beam qualities that were used in this work. The experimental set-up for the measurement of the beam quality correction factors was done in a source-to-axis-distance configuration (SAD) at 10 cm of depth in a water phantom of  $30 \times 30 \times 30 \text{ cm}^3$ . In order to determine the absorbed dose to a point in water an ionization chamber farmer-type (IBA FC-65G SN857) calibrated by the National Metrology Institute of Germany (PTB) was used. This ionization chamber was calibrated for MV beam qualities ( $\text{TPR}_{20,10}$ ) from 0.638 to 0.799, and  $^{60}\text{Co}$ . With this ionization chamber the absorbed dose to a point in water was determined and therefore a ratio of the absorbed dose to a point in water and the scintillator reading can be obtained in a  $k_{Q,Q_0}$ -fashion using equation 5.1.

The scintillating material was a BCF-60 (Saint Gorbain Fiber) based on Polystyrene (density of  $1.06 \text{ g/cm}^3$ ) with a sensitive volume of  $0.00157 \text{ cm}^3$  (1 mm diameter, 2 mm height) and the light guider optical fiber is based on PMMA. The scintillator was positioned at 10 cm depth in isocentric configuration perpendicular to the radiation source (source to surface distance of 90 cm) as it was done in the experiment.

The scintillator was placed at the reference position like the ionization chamber. The chromatic removal method was used for removing the stem signal created in the fiber [19]. In this method the light is filtrated and only the blue and the green wavelengths are used. Using the acquired light signal in those two channels in two different configurations the Cerenkov radiation can be suppressed with high precision [17, 20].

The output factors measurements were carried out at DTU dosimetry laboratory in a SAD configuration at 10 cm depth as for the beam quality correction factor measurements. The experimental data, for output factors, used in this work was previously measured (Anders Beierholm, personal communication) using the protocol described [32]. The used field sizes were  $1 \times 1$ ,  $2 \times 2$ ,  $3 \times 3$ ,  $4 \times 4$ ,  $5 \times 5$ ,  $6 \times 6$ ,  $8 \times 8$  and  $10 \times 10 \text{ cm}^2$ .

## 5.3 Monte Carlo Calculations

The Monte Carlo EGSnrc toolkit was used for the simulation of the radiation transport as well as for the computation of energy depositions [33]. The ICRU90 [34] recommendation values were taken into account in the simulations. The production of secondary generation threshold, as well as the cutoff energies, was set to 0.001 MeV for photons and 0.512 MeV for electrons. The default EGSnrc parameters were used for the radiation transport except for the photon cross section database in which the renormalized photon cross sections were used (mcdfxcom).

Varian Truebeam phase space files (phsp) were downloaded from the official Varian website and used as a radiation source (<https://varian.force.com/>). With the provided blueprints, the collimation system was simulated and phps were generated with the desirable field sizes. No variance reduction techniques (VRT) were used. The generated phsp were obtained at 90 cm distance from the source. These phsp files were further validated against experimental measurements to certify how well the model predicts the experiments. Table 5.1 shows the energy of the generated phsp as well as the beam quality  $\text{TPR}_{20,10}$  for the specific field size of these beams.

**Table 5.1:** Beam quality characteristics.

Nominal Beam Energy	$\text{TPR}_{20,10}$	
	Experimental	Monte Carlo
4 MV	0.623	0.620
6 MV	0.668	0.666
10 MV	0.738	0.740
15 MV	0.763	0.755

The absorbed dose to a point in water and in the scintillator sensitive volume, were computed using the *egs\_chamber* application [35]. The small volume of water, representing the "point in water" was a cylinder with a volume of 0.000785 cm<sup>3</sup> (1 mm diameter, 1mm height). Together with *egs\_chamber* application, two *ausgab* objects (AO), based on *egs\_dose\_scoring*, were developed. These *ausgab* objects; *egs\_light\_scoring* and *egs\_cumulative\_dose\_scoring*, compute the light yield, as defined in equation 5.4. The light yield was computed using a quenching parameter previously obtained [31]. The *egs\_cumulative\_dose\_scoring* computes the contribution of low-energy electrons to the dose in the cavity. We call the latter for the cumulative absorbed dose. For a given electron energy  $E$ , the cumulative absorbed dose is the dose to the cavity when only electrons with kinetic energy below  $E$  are considered. Figure 5.1 gives a graphical representation the *egs\_cumulative\_dose\_scoring* working mechanism. By covering the whole spectrum the cumulative absorbed dose as a function of electron energy can be determined as shown in figure 5.2. These *ausgab* objects run independently of the application, therefore, they can be used together with all the C++-based applications in EGSnrc. Russian roulette and the cross section enhancement were used as a variance reduction techniques.

The in-house developed organic plastic scintillator [36] was fully simulated using blueprints. The set-up for Monte Carlo computations was the same as the experimental one.

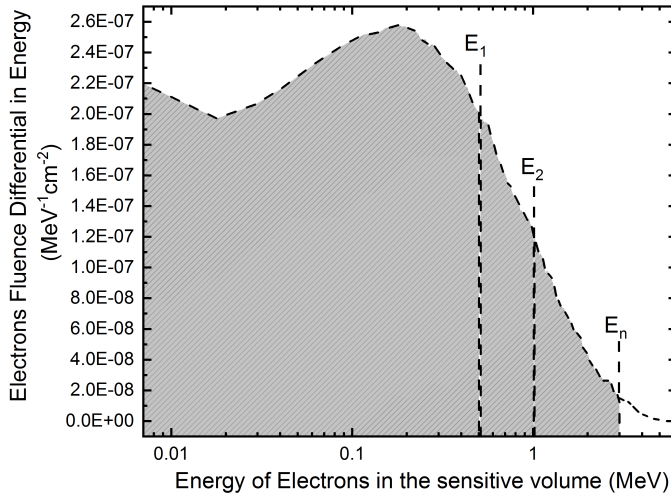


**Figure 5.1:** Representation of the `egs_cumulative_dose_scoring` AO working principle.

## 5.4 Results

### 5.5 Cumulative Absorbed Dose

The cumulative absorbed dose was computed as a means of quantifying the contribution of low energy electrons to the total energy deposited in the scintillator sensitive volume. Figure 5.2 shows the cumulative absorbed dose per electron energy for the two studied scenarios; with a fixed radiation field size and changing the energy, and with a fixed energy and varying the field size. The  $^{60}\text{Co}$  was included as it is a well known spectrum therefore it is used by primary standards as the reference beam quality for calibrations. All the Monte Carlo computations were done with an uncertainty of less than 0.125% and with a coverage factor  $k = 1$ .

The lower cumulative dose curves represent the harder spectra since for a given energy cut-off value less contribution, to the overall absorbed dose, will be received from all the electrons with energies up to that cut-off value. This behaviour can be seen in figure 5.2 in which the small the field size and the higher energy, the harder is the spectrum. For an energy of 100 keV, the difference between the cumulative absorbed doses are bigger when changing the energy than when changing the field size, yielding a 3.13% between  $0.5 \times 0.5 \text{ cm}^2$  and  $10 \times 10 \text{ cm}^2$ , and 5.64% from 6 MV and 15 MV. Therefore, a higher impact of the ionization

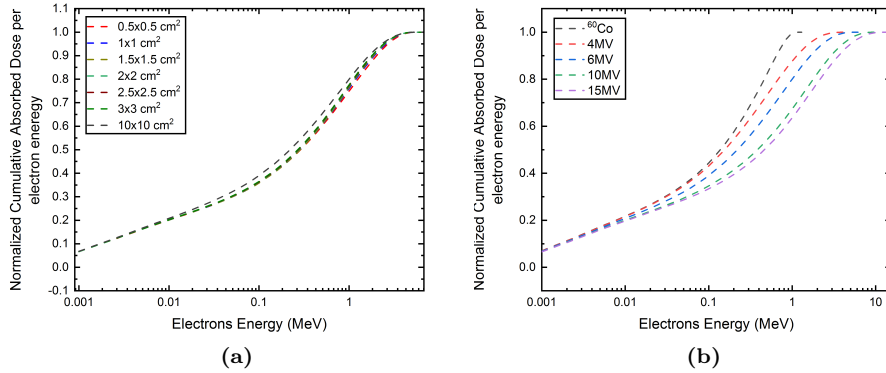


**Figure 5.2:** Cumulative absorbed dose per electron energy for different field sizes and energy of 6MV (a), and different energies and a field size of  $10 \times 10 \text{ cm}^2$  (b)

quenching is expected to take place when changing the energy.

## 5.6 Ionization Quenching Correction Factor

The ionization quenching correction factor,  $k_{ioq}$ , computed using equation 6.7, is shown in figure 5.3. All Monte Carlo uncertainties in the computations were less than 0.19% ( $k = 1$ ). As predicted from figure 5.2 the lower values of  $k_{ioq}$  are found for the more energetic beams (figure 5.3 b). The data shows a larger difference in the  $k_{ioq}$  when changing the energy compared to changing the field size for a fixed energy, 2.11% between 4 MV and 15 MV, and 0.6% between  $0.5 \times 0.5 \text{ cm}^2$  and  $10 \times 10 \text{ cm}^2$ .

The results shown in figure 5.3 are in concordance with those shown in figure 5.2. For the radiation field with more low energetic electrons, the losses due to ionization quenching are bigger. This is an expected result as the ionization quenching is a function of the inverse of  $L_{\Delta}$  (see equation 5.3), the lower the energy of the electrons the higher the stopping power and therefore the lower the light yield. The result suggests that the ionization quenching will have a bigger impact when measuring the  $k_{Q,Q_0}$  than when measuring the OF.

## 5.7 Output Factors

The measured output factors and those simulated by Monte Carlo with and without the ionization quenching effect included ( $0 \text{ cm MeV}^{-1}$  and  $0.019 \text{ cm MeV}^{-1}$ )

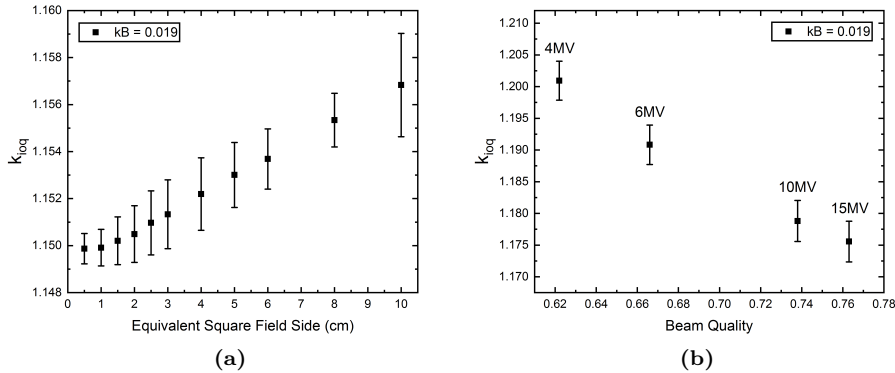


**Figure 5.3:** (a) Normalized ionization quenching corrector factor for different field sizes and energy of 6MV, and (b) different energies and a field size of  $10 \times 10 \text{ cm}^2$

are shown in figure 5.4 upper panel. The relative discrepancies between the experimental measured output factors and the computed are shown in the bottom panel of figure 5.4. All the Monte Carlo computations were done with an uncertainty of less than 0.19% ( $k = 1$ ). The relative discrepancies between the computed output factors, for the two ionization quenching parameters, and the experimental values are less than 1% for all used field sizes.

This result was expected as the impact of ionization quenching, between the smaller field size  $0.5 \times 0.5 \text{ cm}^2$  and the reference  $10 \times 10 \text{ cm}^2$  was less than 0.6% (see figure 5.3). Since the output factors is defined as the ratio of the detector response for a field size and the reference field size (see equation 5.2), a good agreement with experimental measurements was expected.

## 5.8 Beam Quality Correction Factor

The beam quality correction factors, with 6 MV as the reference, are shown in figure 5.5 for the four beam qualities listed in table 5.1. The relative discrepancies between the experimental values and those computed by Monte Carlo are shown in the bottom panel of the figure. For both the computation of the absorbed dose and the light yield the Monte Carlo uncertainties were less than 0.19% ( $k = 1$ ). For the experimental measurements, the higher contribution to the uncertainty comes from the calibration coefficient of the ionization chamber (0.4%).

The figure 5.5 shows that the relative discrepancies between the experimental determined beam quality correction factors and the ones computed by Monte Carlo for a  $kB = 0.019 \text{ cm MeV}^{-1}$  agreed within 0.5%. Nevertheless, for the ideal scintillator ( $kB = 0 \text{ cm MeV}^{-1}$ ) discrepancies up to 2% were obtained. However,

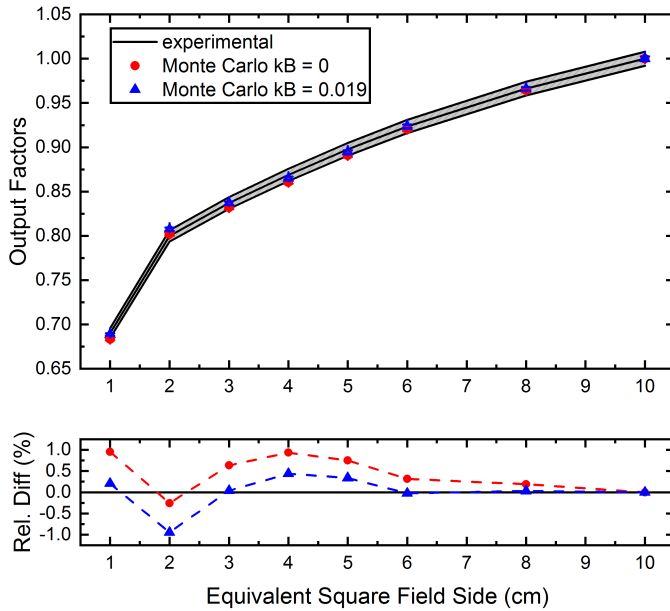


**Figure 5.4:** Output factors measured and simulated by Monte Carlo using as ionization quenching parameters  $0 \text{ cm MeV}^{-1}$  and  $0.019 \text{ cm MeV}^{-1}$

for the ideal scintillator, the fluctuation around 1 is less than 0.58%. This result confirm the similarity of the polystyrene respect water from the radiation absorption point of view.

## 5.9 Discussion

The results show that the effect of ionization quenching for BCF-60 organic plastic scintillators cannot be neglected in MV dosimetry. This effect was considerably higher when changing the beam energy for a fixed field size than when changing the field size for a fixed 6 MV energy. AR Beierholm, Behrens, and Andersen [37] observed an over-response in the absorbed dose to water determined by a BCF-60 organic plastic scintillator compared to that one determined by an ionization chamber when changing the beam quality. In this work a similar behaviour is obtained, and this effect can be now explained by signal losses due to ionization quenching effect.

The results show that the spectral differences are almost 2 times bigger when changing the energy for a fixed field size than for changing the field size for a

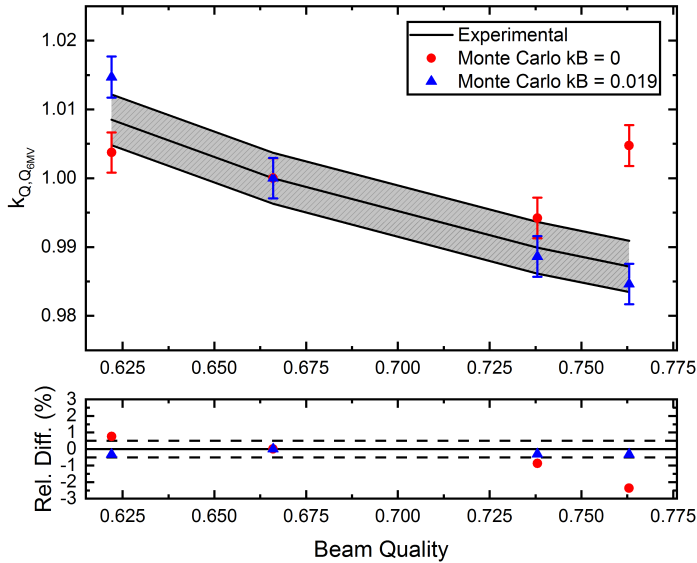


**Figure 5.5:** Beam quality correction factors measured and simulated by Monte Carlo using ionization quenching parameters  $0 \text{ cm MeV}^{-1}$  and  $0.019 \text{ cm MeV}^{-1}$

fixed energy. This effect predicts bigger variation in ionization quenching, from one radiation scenario to another. Figure 5.2 also shows the contribution to the absorbed dose per electron energy in the scintillator sensitive volume. The contribution to the total absorbed dose, from 100 keV energy electrons, are from 36% to 39% for  $0.5 \times 0.5 \text{ cm}^2$  to  $10 \times 10 \text{ cm}^2$  and from 33% to 44% for 15 MV to  $^{60}\text{Co}$  quality. This highlights a commonly overlooked issue in radiation therapy; the contribution of low energy electrons ( $\leq 100 \text{ keV}$ ) in the total dose delivered is generally not considered substantial, but as is evident from figure 5.2, this is not true.

The ionization quenching correction factor was computed by developing equation 5.4 in a Monte Carlo ausgab object. This factor cannot be determined purely experimentally, without Monte Carlo corrections, as the ionization quenching effect is always present in scintillators. The ionization quenching correction factor expresses how much of the absorbed energy in the scintillator cavity is lost in the signal creation process due to this phenomenon. For a fixed energy and different field sizes, the ionization quenching has a small variation, up to 0.6% (figure 5.3) therefore the implication of this effect is not expected to be significant for determining output factors. For a fixed  $10 \times 10 \text{ cm}^2$  field size and variable energy (figure 5.3), however, the ionization quenching effect vary up to 2.11% between

4 MV and 15 MV beam energies. Therefore the impact is expected to be significant for the computation of beam quality correction factors.

One approach to quantifying the clinical impact of the ionization quenching effect in scintillators is by computing the output factors and the beam quality correction factor with and without quenching. As figure 5.4 shows, the experimentally determined output factors are in good agreement (less than 1% of relative discrepancies) with those computed by Monte Carlo both with and without the quenching effect included. Moreover, the relative discrepancies between the computed output factors with and without quenching are less than 0.75%, which is in agreement with the result obtained from figure 5.3. The quenching effect has not been taken into account the output factor calculation in the published literature [3, 4, 7]. This study shows that for determining this quantity, the quenching effect is small and therefore explains why it has not been previously observed and reported in the literature.

The beam quality correction factor expresses how close to water a detector behaves for different beam qualities with respect a reference quality (see equation 5.1). Therefore, a possible energy dependency of the scintillator can be highlighted due to the ionization quenching effect. As figure 5.5 shows, the model in which the ionization quenching is taken into account, is in a good agreement with the experimentally determined beam quality correction factors (less than 0.5% relative discrepancies). For the ideal scintillator, i.e. without quenching, the relative discrepancies respect the experimentally beam quality correction factor are higher than 1% for beam qualities higher than the reference. The figure shows how both the experimental and the quenched beam quality correction factors drop when the energy is increasing. Moreover, this trend in the data highlights the energy dependence of the scintillator due to the quenching effect. It was found, however, that if the quenching effect is not taken into account the beam quality correction factor is rather flat around 1 (less than 0.58% of fluctuation). This result demonstrates that the radiation absorption process in a polystyrene-based scintillator is very similar to that of water, and therefore is a water equivalent detector.

This study quantifies the role of the ionization quenching effect in MV dosimetry. Through the computation of the cumulative absorbed dose per electron energy in the sensitive volume of the scintillator, the contribution of low energy electrons causing higher ionization quenching was computed. Surprisingly, this contribution was found higher than what is commonly assumed for the radiotherapy energy range. A Monte Carlo based `ausgab` object was developed for computing the light yield for scintillators and the ionization quenching correction factors. The ionization quenching correction factor was found to be very constant when changing the radiation field size for a fixed energy unlike for when changing the radiation beam energy and fixing the radiation field size. The impact of the ionization quenching effect for computing the output factors and beam quality correction factors was computed for the first time. A small impact, within uncertainties, was found for the calculation of output factors and therefore, the

quenching effect can be neglected, within uncertainties, when using polystyrene-based scintillators for this application. Since this effect has not been taken into account before, this study shows that even if it would have been taken into account the resulting computed output factor would have been approximately the same. When using the scintillator for a direct measurement of beam quality correction factors, the impact of the quenching effect is higher than 1%, when using 6 MV as a reference beam quality, and therefore should not be neglected. Higher discrepancies are expected if a higher or lower reference beam quality would have been used. This study confirms the high water-equivalence degree, from the energy absorption point of view, of the polystyrene-based scintillator. However, this study shows an energy dependence of the scintillator due to the ionization quenching effect which has not been taken into account before in the literature.

## Conclusions

The role of ionization quenching effect for an organic plastic scintillator, made of BFC-60, has been addressed in this work. A Monte Carlo implementation of Birks formalism was undertaken to allow the computation of the light yield of a plastic scintillator with and without quenching effect. Using the implemented Monte Carlo-based model, an ionization quenching correction factor has been proposed. The model shows a good agreement with the experimental data.

The ionization quenching effect has a small impact when measuring the output factors with an organic plastic scintillator made of BCF-60 and the variation of the output factors due to ionization quenching is probably within the uncertainty of the experimental measurements in a clinical setting. It was found, however, that the impact is higher when measuring the beam quality correction factor. This effect shows an energy dependence of the BCF-60 scintillator due to ionization quenching.

## Acknowledgement

This work was supported by the Danish Council for Independent Research (grant FTP, DFF-4184-00151). Special acknowledgements go to Jarkko Ojala and the EGSnrc developers because of their help in Monte Carlo simulations. Acknowledgements also to Anders Beierholm for providing output factors experimental data.

## References

- [1] S Beddar and L Beaulieu. TH-B-350-01: Scintillation Dosimetry: Review, New Innovations and Applications. *Medical Physics* **35** (6) (2008), 2964–2965.
- [2] L Beaulieu and S Beddar. Review of plastic and liquid scintillation dosimetry for photon, electron, and proton therapy. *Physics in Medicine and Biology* **61** (20) (2016), R305–R343.
- [3] TS Underwood et al. Application of the Exradin W1 scintillator to determine Ediode 60017 and microDiamond 60019 correction factors for relative dosimetry within small MV and FFF fields. *Physics in Medicine and Biology* **60** (17) (2015), 6669–6683.
- [4] D Poppinga et al. The output factor correction as function of the photon beam field size - direct measurement and calculation from the lateral dose response functions of gas-filled and solid detectors. *Zeitschrift für Medizinische Physik* (2017).
- [5] J Morin et al. A comparative study of small field total scatter factors and dose profiles using plastic scintillation detectors and other stereotactic dosimeters: the case of the CyberKnife. *Medical physics* **40** (1) (2013), 011719.
- [6] G Azangwe et al. Detector to detector corrections: A comprehensive experimental study of detector specific correction factors for beam output measurements for small radiotherapy beams. *Medical Physics* **41** (7) (2014).
- [7] H Palmans et al. Dosimetry of small static fields used in external beam radiotherapy: An IAEA-AAPM International Code of Practice for reference and relative dose determination. Technical Report Series No. 483. *Iaea TRS-483* (November) (2017).
- [8] F Therriault-Proulx, L Wootton, and S Beddar. A method to correct for temperature dependence and measure simultaneously dose and temperature using a plastic scintillation detector. *Physics in Medicine and Biology* **60** (20) (2015), 7927–7939.
- [9] P Sibolt et al. Time-resolved plastic scintillator dosimetry in a dynamic thorax phantom. *Radiation Measurements* **106** (2017), 373–377.
- [10] L Archambault et al. Toward a real-time in vivo dosimetry system using plastic scintillation detectors. *International Journal of Radiation Oncology Biology Physics* **78** (1) (2010), 280–287.
- [11] MA Clift, RA Sutton, and DV Webb. Water equivalence of plastic organic scintillators in megavoltage radiotherapy bremsstrahlung beams. *Physics in Medicine and Biology* **45** (7) (2000), 1885–1895.
- [12] AS Beddar. Water equivalent plastic scintillation detectors in radiation therapy. *Radiation Protection Dosimetry* **120** (1-4) (2006), 1–6.

- [13] AS Beddar et al. Monte Carlo calculations of the absorbed dose and energy dependence of plastic scintillators. *Medical Physics* **32** (5) (2005), 1265–1269.
- [14] J Morin et al. A comparative study of small field total scatter factors and dose profiles using plastic scintillation detectors and other stereotactic dosimeters: The case of the CyberKnife. *Medical Physics* **40** (1) (2013).
- [15] S Buranurak et al. Temperature variations as a source of uncertainty in medical fiber-coupled organic plastic scintillator dosimetry. *Radiation Measurements* **56** (2013). Proceedings of the 8th International Conference on Luminescent Detectors and Transformers of Ionizing Radiation (LUMDETR 2012), 307–311.
- [16] L Wootton and S Beddar. Temperature dependence of BCF plastic scintillation detectors. *Physics in Medicine & Biology* **58** (9) (2013), 2955.
- [17] L Archambault et al. Measurement accuracy and Cerenkov removal for high performance, high spatial resolution scintillation dosimetry. *Medical Physics* **33** (1) (2006), 128–135.
- [18] PZY Liu et al. Plastic scintillation dosimetry: Comparison of three solutions for the Cerenkov challenge. *Physics in Medicine and Biology* **56** (18) (2011), 5805–5821.
- [19] JM Fontbonne et al. Scintillating fiber dosimeter for radiation therapy accelerator. *IEEE Transactions on Nuclear Science* **49 I** (5) (2002), 2223–2227.
- [20] AM Frelin et al. Spectral discrimination of Čerenkov radiation in scintillating dosimeters. *Medical Physics* **32** (9) (2005), 3000–3006.
- [21] M Guillot et al. Spectral method for the correction of the Cerenkov light effect in plastic scintillation detectors: A comparison study of calibration procedures and validation in Cerenkov light-dominated situations. *Medical Physics* **38** (4) (2011), 2140–2150.
- [22] L Peralta and F Rêgo. Response of plastic scintillators to low-energy photons. *Physics in Medicine and Biology* **59** (16) (2014), 4621–4633.
- [23] J Boivin et al. A systematic characterization of the low-energy photon response of plastic scintillation detectors. *Physics in Medicine and Biology* **61** (15) (2016), 5569–5586.
- [24] LL Wang et al. Determination of the quenching correction factors for plastic scintillation detectors in therapeutic high-energy proton beams. *Physics in Medicine and Biology* **57** (23) (2012), 7767–7781.
- [25] AM Frelin et al. Comparative Study of Plastic Scintillators for Dosimetric Applications. *IEEE Transactions on Nuclear Science* **55** (5) (2008), 2749–2756.

- [26] JF Williamson et al. Plastic scintillator response to low-energy photons. *Physics in Medicine and Biology* **44** (4) (1999), 857–871.
- [27] F Lessard et al. Validating plastic scintillation detectors for photon dosimetry in the radiologic energy range. *Medical Physics* **39** (9) (2012), 5308–5316.
- [28] JB Christensen and CE Andersen. Applications of amorphous track structure models for correction of ionization quenching in organic scintillators exposed to ion beams. *Radiation Measurements* (2019).
- [29] IAEA. *Absorbed Dose Determination in External Beam Radiotherapy*. Technical Reports Series 398. Vienna: International Atomic Energy Agency, 2001.
- [30] JB Birks. Scintillation from organic crystals: Specific fluorescence and relative response to different radiation. *Proc. Phys. Soc A* **64** (10) (1951), 874–877.
- [31] G Valdes Santurio, M Pinto, and CE Andersen. Evaluation of the ionization quenching effect in organic plastic scintillators using kV x-rays and a modified Birks model with explicit account of secondary electrons. *submitted to Radiation Measurements* (2019).
- [32] A Beierholm et al. Reference dosimetry and small-field dosimetry in external beam radiotherapy: Results from a Danish intercomparison study (2014).
- [33] I Kawrakow and DWO Rogers. The EGSnrc code system: Monte Carlo simulation of electron and photon transport. *Ionizing Radiation Standards, National Research Council of Canada Technical Report No. PIRS-701* (2003), 2001–2015.
- [34] ICRU. *ICRU report 90 - Key Data for Ionizing-Radiation Dosimetry: Measurement Standards and Applications*. Vol. 14. 1. 2016, 1–118.
- [35] J Wulff, K Zink, and I Kawrakow. Efficiency improvements for ion chamber calculations in high energy photon beams. *Medical Physics* **35** (4) (2008), 1328–1336.
- [36] AR Beierholm, LR Lindvold, and CE Andersen. Organic scintillators with long luminescent lifetimes for radiotherapy dosimetry. *Radiation Measurements* **46** (12) (2011), 1982–1984.
- [37] AR Beierholm, CF Behrens, and CE Andersen. Dosimetric characterization of the Exradin W1 plastic scintillator detector through comparison with an in-house developed scintillator system. *Radiation Measurements* **69** (2014), 50–56.



## CHAPTER 6

# Design of a dosimetric system for establishing traceable output factor measurement in radiotherapy MV photon beams

---

Calorimetry is the most fundamental way of determining the absorbed dose. The deposited energy, in the measuring volume, is related either to electrical or temperature quantities [1]. Since the measurement of both, electrical power and temperature can be made traceable to the International System of units (SI), calorimetry can be used as a standard for absorbed dose [2, 3]. Based on that reasoning, current used radiotherapy protocols are based on absorbed dose to a point in water determined by primary standard laboratories (PSLs) using calorimetry [4].

For radiotherapy applications, the calorimetry is performed either based on graphite or water. Since radiotherapy protocols are based on absorbed dose to a point in water, there are several complications that take place even when water-based calorimetry is carried out [5]. Some of them are the specific high heat capacity of the water, larger corrections for heat conduction and convection among others. Graphite have high thermal conductivity and are ideal for small field dosimetry as the heat can be confined in a well defined volume. However, to obtain the absorbed dose to water a conversion factor from graphite to water is

required. This conversion factor is typically computed by Monte Carlo techniques [2].

Regardless the calorimetry type, a transfer detector from PSL conditions to clinical conditions is needed. The detectors used, by excellence, are air-filled ionization chambers. These detectors are mostly used, because the mean energy spent for producing an ion pair  $W_{\text{air}}$  is essentially constant for the radiotherapy energy range [6]. Therefore, this detector has become the 'backbone' of radiotherapy as it has been used over decades for reference dosimetry in radiotherapy practices. However, when measuring field output factors, for relative dosimetry, these detectors have proven to under-respond for small field sizes [7]. Moreover, the International Atomic Energy Agency (IAEA) and the American Association of Medical Physics (AAPM) issued a code of practice for small radiation field TRS-483 [8] in which the output correction factor, not only for ionization chambers but for several detectors, is reported. This code of practice shows that ionization chambers need higher corrections compared to solid-state detectors and the protocol states that organic plastic scintillators are the only detector that does not need correction when changing the field size due to its high degree of water equivalence and small sensitive volumes.

Fiber-coupled organic scintillators have been extensively studied for radiotherapy relative dosimetry applications [9–13]. This detector needs, however, three corrections when used for dosimetry; (i) for temperature dependence, (ii) for Cerenkov and fluorescence light created in the optical fiber (stem signal), (iii) and for ionization quenching effect. The correction for changes in temperature can be done using the model proposed by Buranurak et al. [14]. Several ways of correcting for the Cerenkov radiation obtained in the stem have been developed [15]. Archambault et al. [16] compared the most used methods for removing the stem signal and suggested that the chromatic removal [17] method gives a closer response to ionization chambers. To our knowledge the accuracy of this method, however, has not been fully established, therefore, an alternative accurate method for removing the stem signal is still desirable. In data used in the code of practice for small field dosimetry [8] the ionization quenching effect was not taken into account. This effect, however, was shown to have an effect when determining output factors ( see chapter 5). Therefore, a determination of the ionization quenching effect, with a sub-percentage uncertainty, is still under study.

The objective of this work was to design a dosimetric system that can establish traceable output factor measurements. Such a system can be use to determine the output correction factor for commercially available detectors used in radiotherapy clinics. The route for obtaining traceable output factors is shown in figure6.1. The recommended dosimetric system is based on graphite calorimetry for determining the absorbed dose, an organic plastic scintillator used as a transfer detector, and a design for using the transfer detector with a perfect stem removal for establishing the output factors in a clinical environment. The use of calorimetry will allow to quantify the ionization quenching of organic plastic scintillators and therefore, correct for it. The present study focuses on Monte Carlo with some heat-transfer

theoretical considerations.

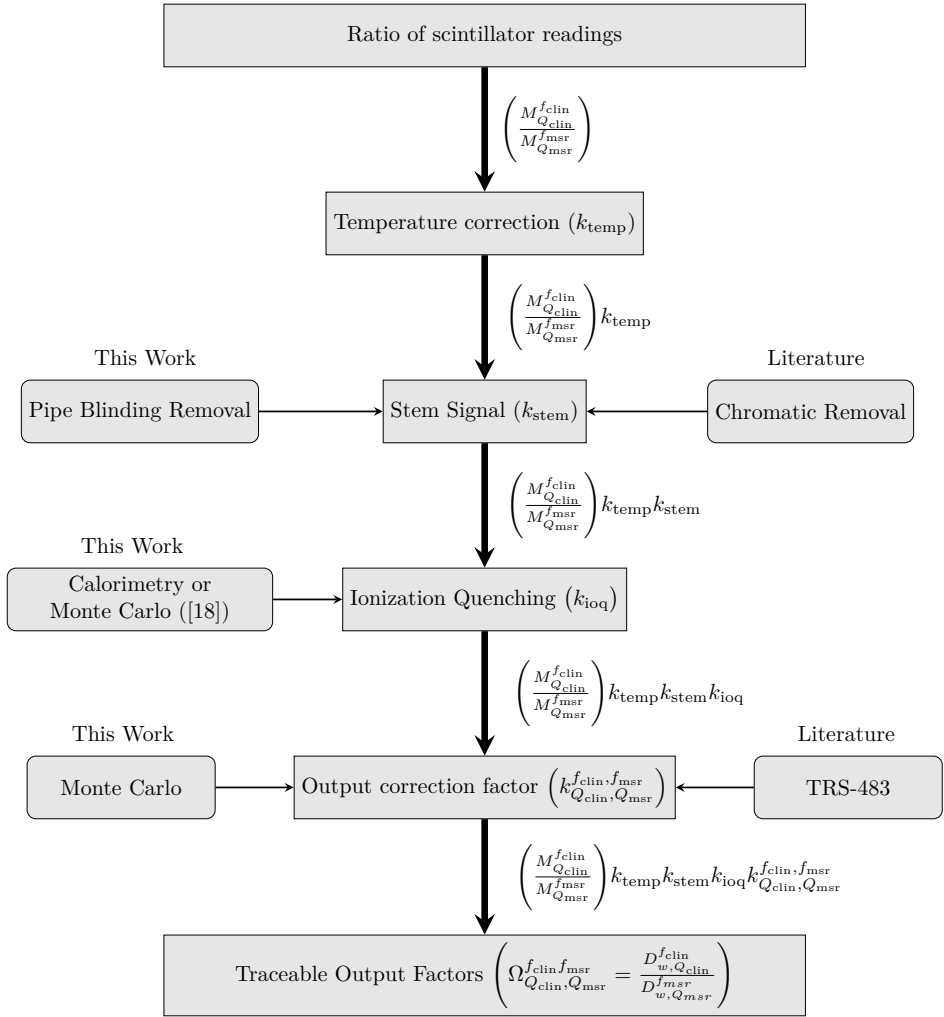


**Figure 6.1:** Flow chart for obtaining traceable output factors. The thick arrows represent the route implemented in this work and the thin arrows the route found in the literature.

## 6.1 Materials and Methods

### 6.1.1 Output Factors TRS-483

The code of practice for small radiation fields [8] defines the field output factor  $\Omega_{Q_{\text{clin}}, Q_{\text{msr}}}^{f_{\text{clin}}, f_{\text{msr}}}$  (OF) as the ratio of absorbed doses to water,  $D_w$ , for a clinical beam quality,  $Q_{\text{clin}}$ , and clinical field size,  $f_{\text{clin}}$ , to a machine-specific reference beam quality,  $Q_{\text{msr}}$ , and field size,  $f_{\text{msr}}$  as:

$$\Omega_{Q_{\text{clin}}, Q_{\text{msr}}}^{f_{\text{clin}}, f_{\text{msr}}} = \frac{D_{w, Q_{\text{clin}}}^{f_{\text{clin}}}}{D_{w, Q_{\text{msr}}}^{f_{\text{msr}}}} \quad (6.1)$$

where  $f_{\text{msr}}$ , for conventional linear accelerators is  $10 \times 10 \text{ cm}^2$ . This ratio is related to the ratio of detector responses,  $M$ , corrected by the influential quantities as:

$$\Omega_{Q_{\text{clin}}, Q_{\text{msr}}}^{f_{\text{clin}}, f_{\text{msr}}} = \frac{D_{w, Q_{\text{clin}}}^{f_{\text{clin}}}}{D_{w, Q_{\text{msr}}}^{f_{\text{msr}}}} = \frac{M_{Q_{\text{clin}}}^{f_{\text{clin}}}}{M_{Q_{\text{msr}}}^{f_{\text{msr}}}} k_{Q_{\text{clin}}, Q_{\text{msr}}}^{f_{\text{clin}}, f_{\text{msr}}} \quad (6.2)$$

where the term  $k_{Q_{\text{clin}}, Q_{\text{msr}}}^{f_{\text{clin}}, f_{\text{msr}}}$  is the output correction factor.

### 6.1.2 Monte Carlo Calculations

The Monte Carlo based software EGSnrc was used for the simulation of the radiation transport [19]. This software was used to compute all the physical quantities of interest in this work. In all the Monte Carlo simulation of radiation transport the ICRU90 [20] recommendation values were used. The electron transport cut-off energy, ECUT; as well as the photon transport cut-off energies, PCUT, were set to 1 keV. The threshold for secondary productions of photon and electrons were set to the same value as the cut-off energies. The transport parameters used were the default values in EGSnrc except for the photon cross section database in which the renormalized photon cross sections were used (mcdx-xcom).

Three applications in EGSnrc were used in the present study; BEAMnrc for the linear accelerator simulation, `egs_chamber` for the computation of the absorbed dose and `cavity` for the computation of the electronic fluence differential in energy. Unlike in `cavity` variance reduction techniques were used in the other two applications; directional bremsstrahlung splitting in BEAMnrc and russian roulette and cross section enhancement in `egs_chamber` [21].

Varian Truebeam phase space files (phsp) were used. The validation of these phsp was done in chapter 3. The used field sizes were  $1 \times 1$ ,  $1.5 \times 1.5$ ,  $2 \times 2$ ,  $2.5 \times 2.5$ ,  $3 \times 3$ ,  $4 \times 4$ ,  $5 \times 5$ ,  $6 \times 6$ ,  $8 \times 8$  and  $10 \times 10 \text{ cm}^2$  for a fixed energy of 6 MV.

### 6.1.3 Temperature dependence: $k_{\text{temp}}$

As pointed out in previous studies [14, 22] organic plastic scintillator have a temperature dependence in radiotherapy clinical environment. Following the model proposed by Buranurak et al. [14], the scintillator response,  $R(T)$ , for a given temperature  $T$ , can be described by:

$$R(T) = R_0(1 + \alpha(T - T_0)) \quad (6.3)$$

where  $R_0$  is the mean scintillator output at a given dose rate for the reference temperature,  $T_0 = 20$  °C, and  $\alpha$  is the linear temperature coefficient. By applying equation 6.3 corrections for temperature differences between a reference field size and a clinical field size can be done.

## 6.1.4 Stem Signal: Pipe Blinding Removal

### 6.1.4.1 Design

In this work a new method for a clean separation of the stem signal from the scintillator signal was developed. Widely used organic plastic scintillators are coupled to an optical plastic fiber [15]. The plastic fiber responds to ionizing radiation and therefore produce a signal similar to that one produced in the scintillator sensitive volume. Air core fibers for transporting the signal to the photo-multipliers have proven to be decrease the Cerenkov radiation induced in the part of the fiber that is exposed to radiation [23]. A scintillator-based detector, without fiber to carry to signal, was developed. The key idea is the eliminate the stem signal by a double measurement method. This developed detector, SP-1 (scintillating pipe), has four main components; the scintillating core, the pipe, a lens (F220SMA-A - 543 nm, Thorlabs) and a quartz fiber (FT600UMT, length m, Thorlabs). Figure 6.2 shows the technical drawings of the SP-1 detector.

The scintillator core is placed in the tip of the pipe. As shown in the figure 6.2 the height of the tip is 5 mm and diameter is 1.1 mm, therefore, scintillator cores of up to 5 mm of length and 1 mm diameter can be used in this pipe. The length is approximately 14 cm with a conical shape. This pipe is printed in a 3D printer with an acrylonitrile styrene acrylate (ASA) material of density  $1.08 \text{ g cm}^{-3}$ . The robustness of the material ensures that pipe is waterproof and therefore can be used in water phantoms under clinical conditions.

The scintillator core was chosen to be 2.12 mm of length and 1 mm of diameter for this study. The scintillating fiber used was the BCF-60 polystyrene-based (Saint Gobain, France) with a green (530 nm) wavelength emission. The BCF-60 fiber was polished after cut in order to ensure a good coupling with the lens. The lens was placed at the open end of the cone. This lens was coupled with a quartz optical fiber in order to carry the signal to the photo-multiplier tube. The photo-multiplier tube is integrated in a house developed box (ME-40 system) for the

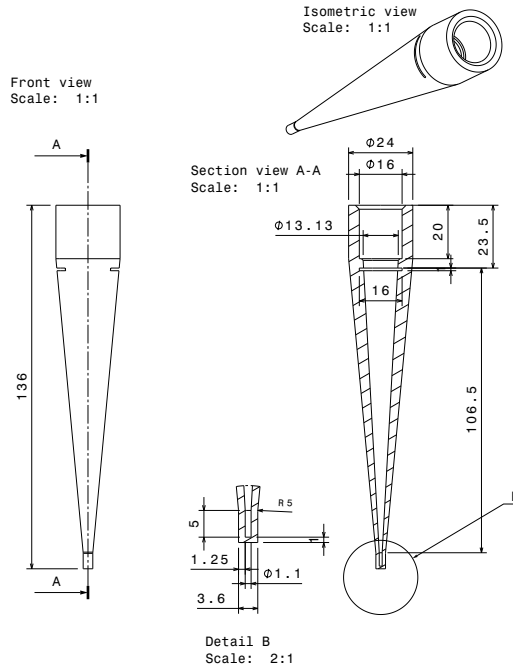


**Figure 6.2:** Technical drawings of the SP-1 prototype scintillator detector.

acquisition of the data. Figure 6.3 how the SP-1 was used for measurements of output factor in a water phantom.

In order to evaluate the design of the SP-1, Monte Carlo simulations were performed. The evaluation consists in computing the ratio of absorbed dose to the scintillator bare core,  $D_{\text{scint}}$ , to the absorbed dose to the scintillator core seating in the pipe,  $D_{\text{SP-1}}$ , (as it will be in experimental measurements) for each individual field size. This ratio,  $r_{\text{SP-1}}$ , will indicate if there is a dependence of field size when using SP-1. For a given field size,  $f$ ,  $r_{\text{SP-1}}$  is defined as:

$$r_{\text{SP-1}}^f = \left[ \frac{D_{\text{scint}}}{D_{\text{SP-1}}} \right]^f \quad (6.4)$$

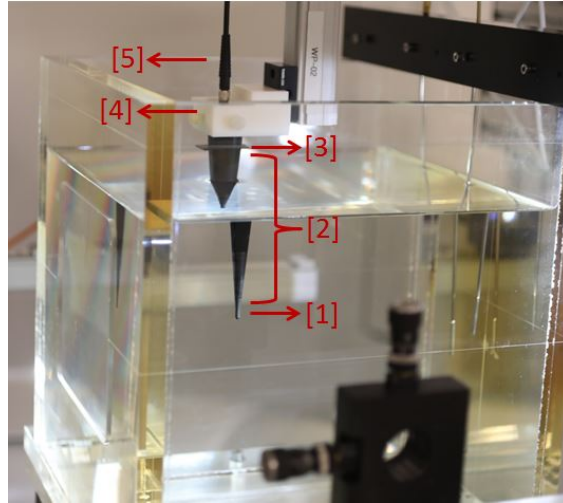


**Figure 6.3:** View of SP-1 in a water phantom while measuring output factors, in blinding mode, with highlights of the components. The scintillating fiber is placed in ([1]) the tip of the pipe ([2]). The black material for the blinding measurement mode [3], [4] is the holder for the pipe and the lens and [5] is represents the coupling of the lens and the quartz fiber.

#### 6.1.4.2 Stem removal

The stem removal was done in two steps, with the scintillator coupled with the lens, and with a dark, non reflective material, blocking the light from the scintillator and therefore "blinding" the lens (see figure 6.3 [3] component). This method we call blinding method. The SP-1 has two parallel slits (see figure 6.2) in which the dark material slides in for the blinding mode. In coupling mode, those holes are covered and therefore any external light sources will not reach the lens. The light in the scintillator,  $L_{scint}$ , will be given by:

$$L_{scint} = L_{cover} - L_{blind} \quad (6.5)$$

where  $L_{cover}$  is the light acquired when the lens is coupled with the scintillator and the SP-1 holes are covered, and  $L_{blind}$  is the light acquired when the lens is blinded by a dark material. Figure 6.4 shows a sketch of how the measurements are performed. This simple subtraction method ensures that the main components of the SP-1 remain the same for the two irradiation conditions. For removing the stem signal, for fiber-coupled organic scintillators, the chromatic removal is the method that gives a closer response to an ionization chamber [24]. In order to test the chromatic removal method, the output factors, using equation 6.2 (right term) without correction, were measured with those measured by an in-house developed fiber-coupled organic scintillator with the same sensitive volume.

The obtained output factors were compared using the blinding removal method. The employed fiber-coupled scintillator (F-134) has been extensively used [18, 25–28] and compared with the W1 commercial system [29]. Both detectors were connected to the same data acquisition system (ME-40) and therefore systematic errors of the readout system will be ruled out.

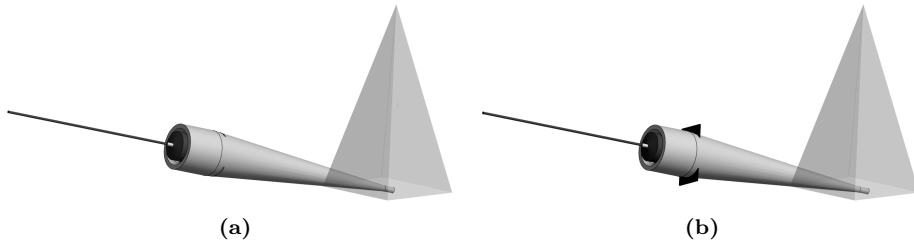


**Figure 6.4:** Graphical view of the blinding method for the stem removal. The first set-up is when the light produced by the scintillator when exposed to radiation is received by the lens (a), and the second when the lens is blind (b).

## 6.1.5 Light Yield

### 6.1.5.1 Monte Carlo-based $k_{ioq}$

For the theoretical estimation of the light yield in a scintillator, a variation of Birks [30] formalism 2.3.1 was used. In this formalism, the light yield in the scintillator,  $L(E)$ , can be computed as:

$$L(E) = \sum_{i=0}^n \int_{E_{min}}^{E_{max}} \frac{A}{1 + kB L_{\Delta i}} dE_i \quad (6.6)$$

where  $A$  is the scintillator efficiency and  $kB$  is the quenching parameter,  $n$  represents the number of charged particles interacting in the scintillator sensitive volume,  $E_{min}$  and  $E_{max}$  are the minimum and maximum energy of these particles that deposit energy along the scintillator sensitive volume and  $L_{\Delta}$  is the restricted lineal electronic stopping power with an energy  $\Delta$  cut-off value.

A Monte Carlo implementation of equation 6.6, previously developed and validated in chapter 4, was used in this work. This implementation allows to compute the light yield in the scintillator with and without a presence of the ionization quenching effect, therefore, correction for ionization quenching can be done. Following this logic, the ionization quenching correction factor as:

$$k_{ioq} = \left[ \frac{L(E)_{ideal}}{L(E)_{quench}} \right]^{f_{clin}, Q_{clin}} \quad (6.7)$$

where  $L(E)_{\text{quench}}$  and  $L(E)_{\text{ideal}}$  represent the scintillator light yield as defined in equation 6.6 with and without quenching effect respectively,  $f_{\text{clin}}$  represents the clinical field size for a beam quality  $Q_{\text{clin}}$ . This parameter corrects for those processes that do not lead to light production.

### 6.1.5.2 Calorimetry-based $k_{\text{ioq}}$

Since the quenching effect is always present in scintillating materials it is difficult to experimentally determine equation 6.7. However, a variation of this factor with respect the field size can be experimentally determined by comparing well known adsorbed doses with scintillator light yield. As explained by chapter 4 this factor heavily depends on the electron spectrum in the scintillator therefore the electron spectrum in which the scintillator is exposed to should be very similar to that one in absence of it. This condition can be fulfilled with using calorimetry in combination with Monte Carlo simulations of the radiation transport. The absorbed dose to the calorimeter core  $D_{\text{core}}$  and the scintillator light yield  $L(E)$ , are related as:

$$\left[ \frac{D_{\text{core}} / L(E)}{D_{\text{core,MC}} / D_{\text{scint,MC}}} \right]_{f_{\text{ref}}, Q_{\text{ref}}}^{f_{\text{clin}}, Q} = k_{\text{ioq}} \frac{f_{\text{clin}}, Q_{\text{clin}}}{f_{\text{ref}}, Q_{\text{ref}}} \quad (6.8)$$

where  $k_{\text{ioq}} \frac{f_{\text{clin}}, Q_{\text{clin}}}{f_{\text{ref}}, Q_{\text{ref}}}$  is the ionization quenching correction factor from a field size,  $f_{\text{clin}}$ , of quality,  $Q_{\text{clin}}$ , to a field size  $f_{\text{ref}}$ , of quality,  $Q_{\text{ref}}$ .

### 6.1.5.3 Calorimetry design and considerations

As stated in the COP for small field dosimetry [8], water-based calorimeters require very high heat loss corrections across the beam profile [1]. For small field sizes, the heat loss correction can be up to 60% [5] which successively depends on the dose rate. Therefore, graphite-based calorimeters are more advantageous for small field dosimetry.

In graphite-based calorimeters, the absorbed dose is measured, in a sensitive volume called core, as a function of either temperature or electric quantities. In order to have smaller corrections due to heat losses, usually the calorimeter has a core jacket and a shield. Two main operation methods are used for graphite based calorimetry: the isothermal [31] and the quasi-adiabatic [1]. In either way, highly sensitive electronics are required to control and monitor the calorimeter.

Typical graphite-based calorimeters used in PSLs are designed for measuring absorbed dose for a  $10 \times 10 \text{ cm}^2$  field size which is the reference field size in radiotherapy protocols [4, 32]. The core is usually built in a disk shape of 2 to 7 mm of height and 16 to 45 mm of diameter [2, 31, 33] and the jacket and the shield are typically with 2 mm of wall. These dimensions are used as the core size is small compared to the field size and the perturbation of the extra core components to the spectrum, in absence of the calorimeter, is small. When small radiation fields take place, however, the averaged absorbed dose will be highly

dependent on the dimensions of the core and the extra core components will create a high perturbation in the spectrum [8]. Moreover, in order to decrease this effect, the physical dimensions of the calorimeter core and the sensitive volume of the transfer detector should be very similar. However, there is a constrain of how small a calorimeter can be due to heat corrections in the core.

#### 6.1.5.4 Design

The design of the calorimeter is based on Monte Carlo simulations. An ideal calorimeter, for this application, will be that one that the ratio of the absorbed dose to the core and the absorbed dose to the transfer detector sensitive volume, has no dependence on field size. Therefore, a requirement of low dependence with field size is employed for testing the calorimeter design. The quantity  $r_f$  relates the absorbed dose to the calorimeter core,  $D_{\text{core}}$  to the absorbed dose to the scintillator sensitive volume  $D_{\text{scint}}$  for an specific field size,  $f$ , as:

$$r_f = \left[ \frac{D_{\text{core}}}{D_{\text{scint}}} \right]^f \tag{6.9}$$

Two main designs were considered for this work and therefore tested in this study one without lateral scatter (WLS) and one with full lateral scatter (FLS). Figure 6.5 shows a 2D sketch of the designs. The graphite core is a cylinder of 0.5 cm of diameter and 0.7 cm of height. The core is hold in vacuum by two straws of 0.025 cm of diameter made of Kapton. This design was chosen as it is a good thermal insulator and it minimizes the contact area. The BCF-60 scintillating fiber is placed at the same point of measurement as the graphite core in a core replica.

In the WLS design, for ensuring a better heat isolation, bodies were 0.5 cm away from the core. Both the upper and the bottom bodies in this design were a cylinder made of graphite with 9 cm diameter and 10 cm height. Figure 6.6 shows the technical drawings of the top and front view for the central part of the FLS design. In this design, the core is embedded in a slab made of solid water with 9 cm diameter and 6 cm height. Because of the low thermal conductivity of solid water, this material acts as a good isolator therefore the distance between the core and the body was shorten to be 0.1 cm in each direction. The solid water slab is in between 2 cylinders of graphite with 9 cm diameter and 3 cm height each. Figure 6.7 shows a view of FLS calorimeter during assembly. The light readout of the scintillator fiber, used as a transfer detector, will be done by coupling 2 lenses that will be placed outside the radiation field. The light will be guided to the lenses through holes in the phantom (see figure 6.7 [6]).

The calorimeter is then assembled and mounted in an aluminum frame. Each calorimeter cylinder is mounted into an aluminum frame using plastic screws for fixation. These aluminum frames are centered by rods and therefore the calorimeter components are placed by sliding them in. Once the calorimeter is

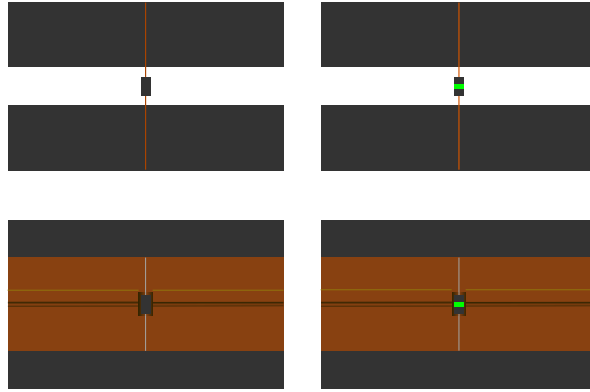


**Figure 6.5:** Sketch of the WLS (top) and FLS (bottom) calorimeter designs. At the left the absorbed dose is scored in the calorimeter core and at the right the absorbed dose is scored in the scintillator sensitive volume (represented as with the green color)

mounted into the aluminum frames (figure 6.8), it will be embedded in a vacuum chamber. This vacuum chamber have walls made of polymethyl methacrylate (PMMA) of 3 cm thickness that provides tightness for the vacuum chamber. This design was inspired by the Bureau International des Poids et Mesures (BIPM) report [2].

### 6.1.6 Output correction factor

The output correction factor,  $k_{Q_{\text{clin}}, Q_{\text{msr}}}^{f_{\text{clin}}, f_{\text{msr}}}$ , corrects for the detector differences compared to a point in water and is usually computed by Monte Carlo. From equation 6.2 this factor is defined as:

$$k_{Q_{\text{clin}}, Q_{\text{msr}}}^{f_{\text{clin}}, f_{\text{msr}}} = \frac{D_{w, Q_{\text{clin}}}^{f_{\text{clin}}} / \overline{D}_{\text{det}, Q_{\text{clin}}}^{f_{\text{clin}}}}{D_{w, Q_{\text{msr}}}^{f_{\text{msr}}} / \overline{D}_{\text{det}, Q_{\text{msr}}}^{f_{\text{msr}}}} \quad (6.10)$$

where the term  $\overline{D}_{\text{det}}$  represents the average absorbed dose in the detector sensitive volume, for a clinical or machine-specific field  $f_{\text{clin}}$  or  $f_{\text{msr}}$ , of quality  $Q_{\text{clin}}$  or  $Q_{\text{msr}}$ , respectively. In this work the output correction factor for the SP-1 was computed for several field sizes.

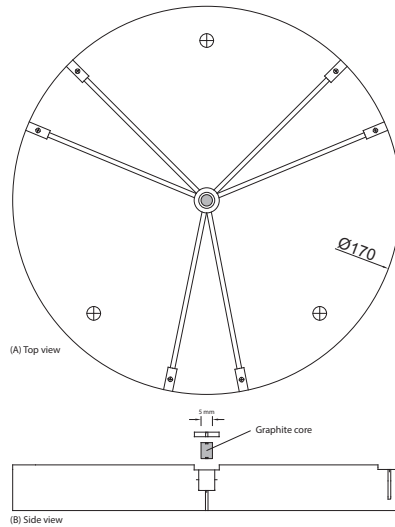


**Figure 6.6:** Technical drawings with the top and front view for the central part of the calorimeter prototype for the FLSr design.

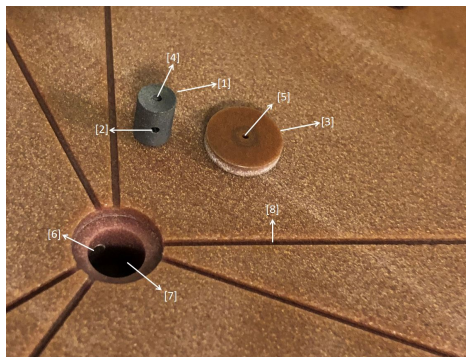


**Figure 6.7:** Zoom up view of the central part of the FLS calorimeter design. The core [1] with the hole for the scintillating fiber [2] is inserted in the vacuum hole [7] and cover with the lid [3]. The hole in the top part of the core [4] and the lid [5] are for centering. The hole across the phantom till the vacuum hole [6] is for light readout. The groove on top of the phantom [8] is one of the 6 grooves that are used for checking the centering of the core and also for the thermistors.

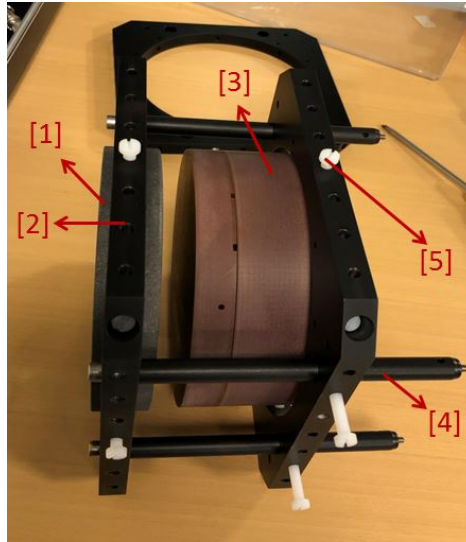


**Figure 6.8:** View of the calorimeter mounting process. The top part of the calorimeter (the graphite cylinder)[1] is mounted into an aluminum frame [2] using plastic screws for fixation [5] and that frame is slipped through the aluminum rods [4]. The same process is repeated with the solid water cylinder [3] until the calorimeter is fully mounted

## 6.2 Results

### 6.2.1 Output Factors

Figure 6.9 shows the measured output factors with the SP-1, using the blinding stem removal method, and with the fiber-coupled scintillator using the chromatic removal method. The measurements for both detectors were corrected by temperature using the equation 6.3. The right y axis of the figure represents the relative discrepancies between them. As the figure 6.9 shows, the relative discrepancies between them increase with the decrease of the field size. However, all the relative discrepancies are less than 1% for all the field sizes. This result shows that both stem removal methods give a similar output factor within uncertainties. This result suggests that the chromatic removal method does a good stem removal.

### 6.2.2 Field size dependence of SP-1

Figure 6.10 shows the field size dependence of SP-1 compared to the absorbed dose in the scintillator sensitive volume in absence of the pipe using equation 6.4. The figure shows the computed  $r_{SP_1}$  for all studied field sizes. Each individual

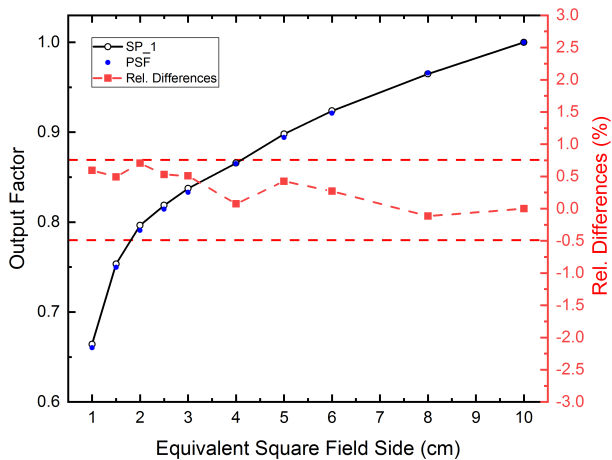


**Figure 6.9:** Output factors measured with SP-1 and a fiber-coupled organic plastic scintillator (F-134)

data point in figure 6.10 has an uncertainty of less than 0.25%. Figure 6.10 also shows the mean and standard deviation of the data. The results suggest that the perturbation of the pipe, to the electron spectrum in the sensitive volume, with respect to that one without the pipe is constant for the studied field sizes.

### 6.2.3 Calorimeter design

As explained in section 6.1.5.3 the calorimeter design is based on the electronic spectrum in the core compared to that one of the transfer detector, and the factor  $r_f$ . Figure 6.11 shows the computed electronic spectra for both designs (WLS and FLS) for an small field size of  $1 \times 1 \text{ cm}^2$  and a broad small field size of  $5 \times 5 \text{ cm}^2$ . The figure shows that in the FLS design the electronic spectrum for the scintillator and the graphite core are very similar whereas for the WLS design they are not. Moreover, the figure shows that the small differences between the electronic spectrum for the different field sizes are roughly the same.

The computed  $r_f$  for the 2 studied designs is shown in figure 6.12. The figure shows that the WLS design has a higher dependence with field size, compared to the FLS design, yielding corrections larger than 1% for field sizes smaller than  $4 \times 4 \text{ cm}^2$ . The FLS design shows a rather constant behaviour for field sizes higher than  $2 \times 2 \text{ cm}^2$ . Moreover, the correction for field sizes down to  $1.5 \times 1.5 \text{ cm}^2$  is less than 1%. The larger correction for the two studied designs

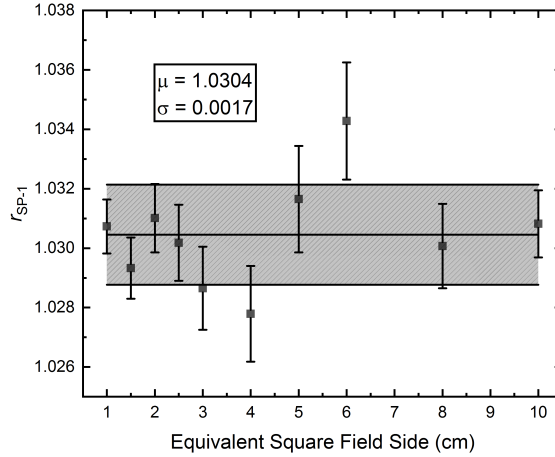


**Figure 6.10:** Field size dependence of the SP-1 detector.

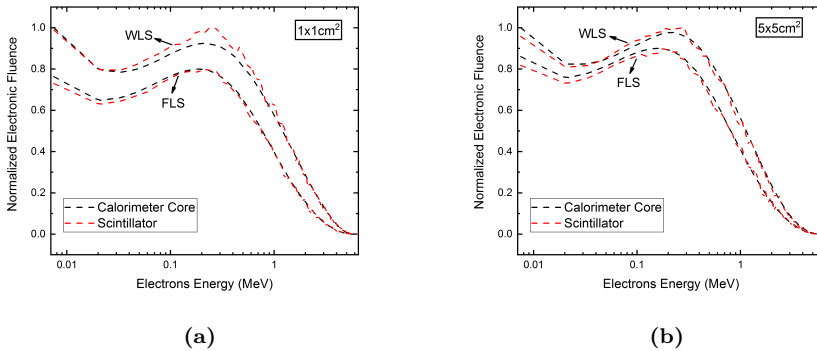


**Figure 6.11:** Normalized electronic spectra in the calorimeter core and in the transfer detector sensitive volume for a small field size of  $1 \times 1 \text{ cm}^2$  and a broad small field size of  $5 \times 5 \text{ cm}^2$

was found to be for the smallest field size,  $1 \times 1 \text{ cm}^2$ , yielding a 7.7% for the WLS design and 2.8% for the FLS design.

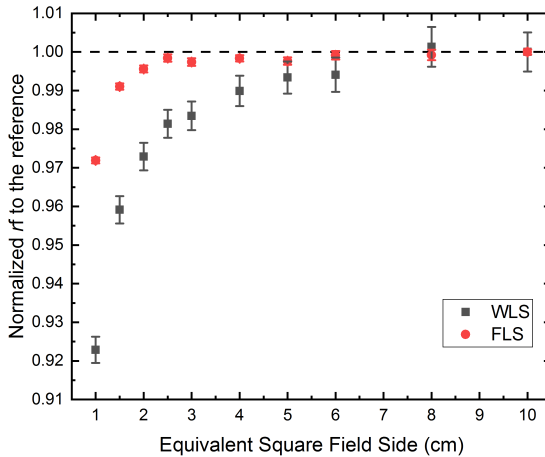


**Figure 6.12:** Normalized  $r_f$  to the reference for the 2 studied calorimeter designs.

### 6.2.4 Ionization Quenching Correction Factor

The ionization quenching correction factor was computed by Monte Carlo using equation 6.6. The used quenching parameter was the one previously obtained by chapter 4. For all the computations the uncertainty was less than 0.15%. Figure 6.13 shows the normalized ionization quenching correction factors to the reference  $10 \times 10 \text{ cm}^2$ . The figure shows that the correction for the smallest studied field size  $1 \times 1 \text{ cm}^2$  compared to the reference is 0.72%.

This factor was also computed in the calorimeter configuration in order to have a theoretical prediction of the experiment. Figure 6.14 shows the computed ionization quenching correction factors normalized to the reference field size  $10 \times 10 \text{ cm}^2$ . The effect of this factor seems to be less under the calorimeter conditions than when using it in the SP-1. This effect can be explained as the spectral changes when changing the field size are bigger for the SP-1 scenario compared to the calorimeter scenario. This factors are in good agreement with the previously obtained for fiber coupled organic plastic scintillator (see chapter 5).

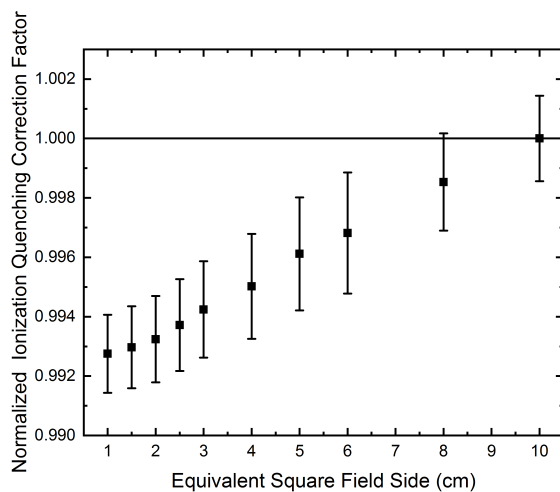


**Figure 6.13:** Ionization correction factors normalized to the reference field size  $10 \times 10 \text{ cm}^2$  for the SP-1 detector.

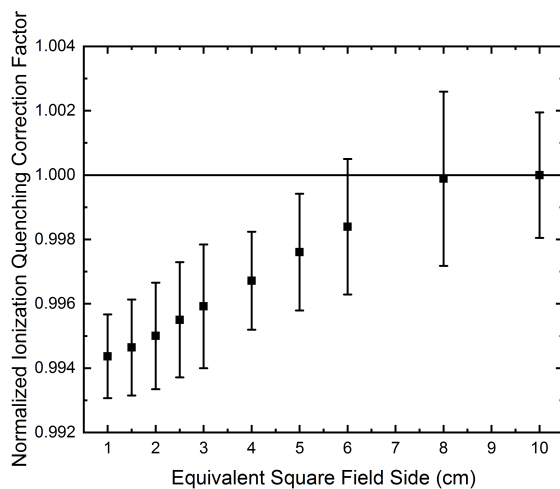


**Figure 6.14:** Predicted normalized ionization correction factors to the reference field size  $10 \times 10 \text{ cm}^2$  for the transfer scintillator detector

### 6.2.5 Output Correction Factor

Figure 6.15 shows the computed output correction factors for the SP-1 detector using equation 6.10. This correction factor was corrected by ionization quenching as explained in the figure 6.1. The relative discrepancies for all MC computations were less than 0.15%. The figure shows that for all field sizes this factor is less than 0.54% compared to the reference. Moreover, the figure does not show a noticeable trend in the data and therefore the output correction factors, after corrected for ionization quenching, for the SP-1 scintillator detector can be considered 1.

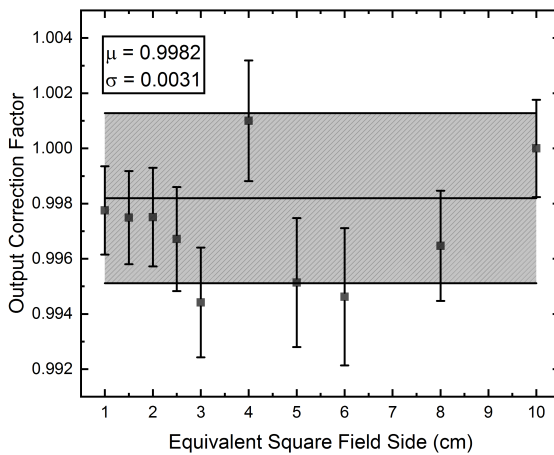


**Figure 6.15:** Output correction factors for the SP-1 detector corrected by ionization quenching

In order to compare the impact of the ionization quenching effect in the output correction factor, the figure 6.16 shows the uncorrected output correction factors. The figure shows more scatter compared the corrected values. Moreover, the mean value of the data is 0.28% off from the reference. However, this result suggests that the output correction factor can be assumed to be 1 (as states TRS-483) within uncertainties.

## 6.3 Discussion

In this work a dosimetric system for determining traceable output factors have been proposed. The system uses a graphite-based calorimeter for determining the absorbed dose and an organic plastic scintillator as a transfer detector. The

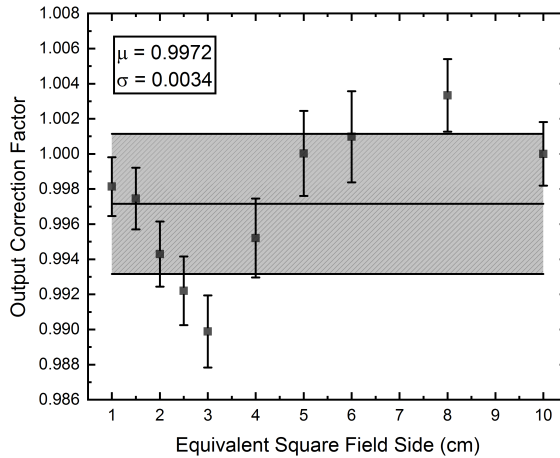


**Figure 6.16:** Output correction factors for the SP-1 detector without correction by ionization quenching (TRS-483)

transfer detector can be then used in a clinical environment by using pipe that allows a clean separation of the stem and the scintillator signals. Monte Carlo calculations support the use of the developed detector as the output correction factor is very closed to 1 for each field size. With the developed system traceable output factors for field sizes down to  $1 \times 1 \text{ cm}^2$  can be measured.

The dosimetric properties of two calorimeter designs (WLS and FLS) were evaluated. The electronic spectrum in the calorimeter core and the transfer detector sensitive volume together with the ratio of absorbed doses were used in order to test the designs. The results show that for the FLS the electronic spectrum is very similar in the core and in the transfer detector sensitive volume. Moreover, the small differences between them are extremely close for a small field size and a broad field size. This behaviour predicts that the ratio of absorbed doses will be approximately the same for these 2 field sizes. The WLS model, however, have bigger differences in the computed electronic spectrum. As pointed out in chapter 4, the ionization quenching effect is heavily dependent on the spectrum in the scintillator sensitive volume, as the calorimeter core is used for establishing the absorbed dose, such spectral differences between the calorimeter core and the scintillator sensitive volume will bias the estimation of the ionization quenching effect.

The  $r_f$  confirms what was predicted by the computed electronic spectra. The results show that the WLS design have a very strong field size dependence, yielding corrections larger than 1% for field sizes smaller than  $4 \times 4 \text{ cm}^2$ . On the other

hand, the FLS design has a small field size dependency. For all field sizes the correction is less than 1% but the smaller field size which the correction was 2.8%. These results recommend that the FLS design is more suitable for this application and suggest that this calorimeter can be used for field sizes down to  $1 \times 1 \text{ cm}^2$  with a small correction.

The SP-1 detector measured output factors are in good agreement with those measured by a fiber-coupled organic plastic scintillator. This result demonstrates that accuracy of the chromatic removal method is effective for removing the stem signal within uncertainties. With the developed SP-1 detector the stem removal is clean and no assumptions are made i.e the ratio of the blue channel to the green channel is constant when changing the field size. Therefore, the used of the pipe with the transfer detector as the sensitive volume is of importance for reducing uncertainties to a primary standard level. As shown in figure 6.10 the pipe compared to the bare sensitive volume in absence of it is field size independent. This result shows that the fluence perturbation of the pipe is very small. Moreover, it is expected that the volume averaging effect and the ionization quenching effect have a bigger role in the determination of output factors.

The ionization quenching correction factor (see equation 6.6) was computed for the developed detector SP-1. The effect of ionization quenching for the smallest field size compared to the reference was 0.72%. This result demonstrates that this effect is not negligible for output factor measurements as previously observed in chapter 5. This effect, was found to be 0.6% in chapter 5. We believe that the difference between the ionization quenching correction factors are because of spectral changes induced by the pipe compared to the optical fiber. The ionization quenching effect, predicted for the calorimeter scenario was found to be in the same order as those obtained in chapter 5.

The output correction factor for the developed detector SP-1 was computed by Monte Carlo following the equation 6.2 proposed by the code of practice. This factor was then corrected by ionization quenching as stated in the chart 6.1. The corrected output correction factor is very close to unity for all the studied field sizes. As the figure 6.15 shows, all the factors are agreed with the reference with less than 0.54% of discrepancy. Moreover, the mean of the data showed in the figure is very close to 1 with a small standard deviation. For the obtained output correction factors without taking into account the ionization quenching the result are slightly different. However, the value of the mean is very close to 1 and therefore this result suggests that this factor can be neglected within uncertainties as it has been done in the COP TRS-483. This result highlights the potential of this detector for direct measurements of output factors and supports that with this detector traceable output factors measurements can be carried out using the system proposed in figure 6.1.

## 6.4 Conclusions

A dosimetric system for measuring traceable output factors has been proposed in this work. This system includes a correction factor due to ionization quenching that has not been taken into account, in the literature, for this application. The determination of this factor relies on calorimetry measurements therefore a novel design of a calorimeter for small fields dosimetry was done. The calorimeter design was tested through Monte Carlo simulations obtaining promising results. Although heat transfer simulations were not performed in this study. The proposed transfer detector for calorimetry measurements was a bare organic plastic scintillator fiber. This fiber can be placed in a 3D printed pipe (SP-1) allowing to be used in clinical environment.

The developed SP-1 detector was tested against a fiber-coupled organic scintillator, with the same core size and fiber type, through output factor measurements yielding a good agreement. The ionization quenching effect was computed for the developed detector. This effect requires a correction of  $(0.72 \pm 0.25)\%$  for the small field ( $1 \times 1 \text{ cm}^2$ ) compared to the reference. However, it was found that when computing the output correction factor for the developed detector the ionization quenching has a small effect. Moreover, the computed output correction factors, with and without ionization quenching, are shown small differences.

In this chapter a detailed Monte Carlo supported study was carried out for testing a proposed dosimetric system for measurements of traceable output correction factors. The results suggest that the system is feasible and can be used. Once traceable output factor have been established, output correction factors for clinical available detectors can be obtained.

## References

- [1] J Seuntjens and S Duane. Photon absorbed dose standards. *Metrologia* **46** (2) (2009), S39.
- [2] S Picard, DT Burns, and P Roger. Construction of an absorbed-dose graphite calorimeter. *Rapport BIPM* **1** (May) (2009).
- [3] J Renaud et al. Aerrow: A probe-format graphite calorimeter for absolute dosimetry of high-energy photon beams in the clinical environment. *Medical Physics* **45** (1) (2018), 414–428.
- [4] International Atomic Energy Agency. IAEA Technical Report Series No.398. *Atomic Energy* (2000), 1–229.
- [5] L de Prez. *Small field dosimetry in high energy photon beams based on water calorimetry*. Tech. rep. 2010.
- [6] DT Burns, C Kessler, and JP McCaffrey. Key comparison BIPM.RI(I)-K3 of the air-kerma standards of the ENEA, Italy and the BIPM in medium-energy x-rays. **48** (2014), 1–15.

- [7] R Alfonso et al. A new formalism for reference dosimetry of small and nonstandard fields. *Medical Physics* **35** (11) (2008), 5179–5186.
- [8] H Palmans et al. Dosimetry of small static fields used in external beam radiotherapy: An IAEA-AAPM International Code of Practice for reference and relative dose determination. Technical Report Series No. 483. *Iaea TRS-483* (November) (2017).
- [9] D Poppinga et al. The output factor correction as function of the photon beam field size - direct measurement and calculation from the lateral dose response functions of gas-filled and solid detectors. *Zeitschrift für Medizinische Physik* (2017).
- [10] TS Underwood et al. Application of the Exradin W1 scintillator to determine Ediode 60017 and microDiamond 60019 correction factors for relative dosimetry within small MV and FFF fields. *Physics in Medicine and Biology* **60** (17) (2015), 6669–6683.
- [11] F Therriault-Proulx, L Wootton, and S Beddar. A method to correct for temperature dependence and measure simultaneously dose and temperature using a plastic scintillation detector. *Physics in Medicine and Biology* **60** (20) (2015), 7927–7939.
- [12] J Morin et al. A comparative study of small field total scatter factors and dose profiles using plastic scintillation detectors and other stereotactic dosimeters: the case of the CyberKnife. *Medical physics* **40** (1) (2013), 011719.
- [13] G Azangwe et al. Detector to detector corrections: A comprehensive experimental study of detector specific correction factors for beam output measurements for small radiotherapy beams. *Medical Physics* **41** (7) (2014).
- [14] S Buranurak et al. Temperature variations as a source of uncertainty in medical fiber-coupled organic plastic scintillator dosimetry. *Radiation Measurements* **56** (2013), 307–311.
- [15] S Beddar and L Beaulieu. *Scintillation dosimetry*. CRC Press, 2016.
- [16] L Archambault et al. Measurement accuracy and Cerenkov removal for high performance, high spatial resolution scintillation dosimetry. *Medical Physics* **33** (1) (2006), 128–135.
- [17] JM Fontbonne et al. Scintillating fiber dosimeter for radiation therapy accelerator. *IEEE Transactions on Nuclear Science* **49 I** (5) (2002), 2223–2227.
- [18] G Valdes Santurio, M Pinto, and CE Andersen. Evaluation of the ionization quenching effect in organic plastic scintillators using kV x-rays and a modified Birks model with explicit account of secondary electrons. *submitted to Radiation Measurements* (2019).

- [19] I Kawrakow and DWO Rogers. The EGSnrc code system: Monte Carlo simulation of electron and photon transport. *Ionizing Radiation Standards, National Research Council of Canada Technical Report No. PIRS-701* (2003), 2001–2015.
- [20] ICRU. *ICRU report 90 - Key Data for Ionizing-Radiation Dosimetry: Measurement Standards and Applications*. Vol. 14. 1. 2016, 1–118.
- [21] J Wulff, K Zink, and I Kawrakow. Efficiency improvements for ion chamber calculations in high energy photon beams. *Medical Physics* **35** (4) (2008), 1328–1336.
- [22] S Beddar. On possible temperature dependence of plastic scintillator response. *Medical Physics* **39** (10) (2012), 6522.
- [23] J Lambert et al. Cerenkov-free scintillation dosimetry in external beam radiotherapy with an air core light guide. *Physics in Medicine & Biology* **53** (11) (2008), 3071.
- [24] L Archambault et al. Water-equivalent dosimeter array for small-field external beam radiotherapy. *Medical Physics* **34** (5) (2007), 1583–1592.
- [25] AR Beierholm et al. Characterizing a pulse-resolved dosimetry system for complex radiotherapy beams using organic scintillators. *Physics in Medicine and Biology* **56** (10) (2011), 3033–3045.
- [26] AR Beierholm, LR Lindvold, and CE Andersen. Organic scintillators with long luminescent lifetimes for radiotherapy dosimetry. *Radiation Measurements* **46** (12) (2011), 1982–1984.
- [27] P Sibolt et al. Time-resolved plastic scintillator dosimetry in a dynamic thorax phantom. *Radiation Measurements* **106** (2017), 373–377.
- [28] G Valdes Santurio and CE Andersen. Quantifying the ionization quenching effect in organic plastic scintillators used in MV photon dosimetry. *submitted to Radiation Measurements* (2019).
- [29] AR Beierholm, CF Behrens, and CE Andersen. Dosimetric characterization of the Exradin W1 plastic scintillator detector through comparison with an in-house developed scintillator system. *Radiation Measurements* **69** (2014), 50–56.
- [30] JB Birks. Scintillation from organic crystals: Specific fluorescence and relative response to different radiation. *Proc. Phys. Soc A* **64** (10) (1951), 874–877.
- [31] J Daures and A Ostrowsky. New constant-temperature operating mode for graphite calorimeter at LNE-LNHB. *Physics in Medicine and Biology* **50** (17) (2005), 4035–4052.
- [32] PR Almond, PJ Biggs, and WF Hanson. AAPM 's TG - 51 Protocol for Clinical Reference Dosimetry of High-Energy Photon and Electron Beams. *Medical Physics* **26** (1999) (1999), 1–9.

- [33] Y Morishita et al. A standard for absorbed dose rate to water in a  $^{60}\text{Co}$  field using a graphite calorimeter at the National Metrology Institute of Japan. *Radiation protection dosimetry* **154** (3) (2012), 331–339.

## CHAPTER 7

# Summary and Outlook

---

## 7.1 Summary

The work presented in this thesis has been carried out in the scope of designing a calorimetry based dosimetric system, with an organic plastic scintillator as a transfer detector, for computing output correction factors with a sub-percent level of uncertainty. The motivation was to enable radiotherapy clinics in Denmark to have a detector-specific output correction factor, and thereby provide a higher precision in delivered doses. The first step was to characterize the organic plastic scintillators with respect to ionization quenching. In order to accomplish that, a Monte Carlo application was developed implementing Birks formalism for computing the light yield. The second step was to obtain the quenching parameter or the widely used scintillator material, BCF-60, as the reported values in the literature are not in agreement. With the obtained quenching parameter, the impact of ionization quenching was quantified for MV photon beam dosimetry. Based on the results, a dosimetric system was proposed for measuring traceable output factors. A calorimeter is used in this system for determining the ionization quenching effect in scintillators when measuring output factors. A detector with a scintillating fiber as the core was developed allowing a clean stem signal removal. This detector allows the use of the calorimeter transfer detector in clinical conditions.

A detailed summary and conclusions are presented below:

### 7.1.1 Monte Carlo

A Monte Carlo application computing the light yield using a variation of the Birks formalism was developed. This method uses the full electronic spectrum in the scintillator sensitive volume and therefore discards approximations commonly made in the literature e.g. the electrons are fully stopped in the scintillating volume. A validation against a different computation method was carried out. The discrepancies between the two methods are less than 0.97% for all the considered

energies. The developed application was also tested against experimental data available in the literature. A good agreement between simulations and the data was found.

### 7.1.2 Ionization quenching effect using kV x-rays

The developed MC application was used to determine the quenching parameter for a fiber-coupled organic plastic scintillator when exposed to low energy x-rays. This experiment allowed both the validation of the MC application for computing the ionization quenching, and to obtain the ionization quenching parameter ( $k_B$ ). A range of parameters was found to fit the experimental data within uncertainties (from 0.016 to 0.019  $\text{cm MeV}^{-1}$ ). The quenching parameter providing the best fit to the experimental data was 0.019  $\text{cm MeV}^{-1}$ . This study also highlighted the importance of using the electronic spectrum for reporting ionization quenching effects. Finally, the results demonstrate that the ionization quenching effect for MV photon beam dosimetry can be quantified by using the same validated Monte Carlo application with the best fit ionization quenching parameter.

### 7.1.3 Ionization quenching effect in MV photon dosimetry

The ionization quenching effect was quantified for two different scenarios: the determination of output factors and the direct determination of beam quality correction factors for ionization chambers using the organic plastic scintillator as reference for the absorbed dose to water in a given point. An ionization quenching correction factor was proposed based on the Monte Carlo developed application and the ionization quenching parameter previously obtained. This factor was found to be roughly 0.6% for a  $0.5 \times 0.5 \text{ cm}^2$  field size compared to the reference field size  $10 \times 10 \text{ cm}^2$  for a 6 MV photon beam. For the determination of the beam quality correction factor for ionization chambers, the ionization quenching effect was found to be 2.11% for beam qualities between 4 and 15 MV. These results agreed with the experimental data and suggested that fiber coupled organic plastic scintillators might have an energy dependence due to ionization quenching. Furthermore, the study concludes that although the experimental data is in good agreement with the computed values, the stem removal needs further investigation.

### 7.1.4 Design of dosimetric system for establishing output factors in MV photon beams

A dosimetric system for measuring traceable output factors was proposed in this thesis. This system is based on a graphite calorimeter for determining the absorbed dose, and an organic plastic scintillator as the transfer detector. This novel calorimeter design was supported by Monte Carlo computations, and it

was predicted that the absorbed dose can be measured with small corrections for field sizes down to  $1 \times 1 \text{ cm}^2$  for 6 MV photon beams. Additionally, a device capable of using the transfer detector in a clinical environment was developed, thereby solving the two main challenges of organic plastic scintillators used in MV dosimetry: the ionization quenching and the stem removal.

The ionization quenching effect can be directly quantified by using the calorimeter and the stem signal can be removed by using the transfer device, called SP-1. This removal method offers a more direct way for removing the stem signal. With the SP-1 and the stem removal method, the efficiency of the chromatic removal approach was investigated by measuring output factors with the device and a fiber-coupled organic plastic scintillator. The output factors measured with both system agreed with less than 1% of relative discrepancies. The chromatic removal method, however, is not very practical in a clinical environment and furthermore, several assumptions are needed for its usage e.g. the blue to the green light ratio is linear and independent of field size. The SP-1 and the proposed stem removal method do not rely on these assumptions and it can be used directly in a clinical environment. The output correction factor was computed for SP-1, and the effect of the ionization quenching in the output correction factor was quantified using the developed Monte Carlo application. The ionization quenching effect appears to have a small impact on the output correction factors, as it is close to 1 for field sizes down to  $1 \times 1 \text{ cm}^2$ . The result showed that in either case, taking the ionization quenching into account or discarding it, the output correction factor is very close to 1 and therefore agrees with the values previously reported in the code of practice TRS-483.

All the steps in the proposed dosimetric system were tested. The results suggested that with this system, traceable output factor measurements can be performed successfully. The next step will be to optimize the design with respect to heat transfer before the system can eventually be realized and implemented.

### 7.1.5 Main conclusions

1. The ionization quenching effect is a small but not negligible effect when measuring output factors.
2. Monte Carlo computations support that a graphite based calorimeter can be used for quantifying the ionization quenching effect in organic plastic scintillators exposed to small radiation fields.
3. The proposed dosimetric system allows the measurement of traceable output factors using organic plastic scintillators.
4. The developed detector can be used in a clinical environment for determining the output correction factor for clinically available detectors.

## 7.2 Outlook

The experimental realization of the calorimeter needs to be carried out. Heat conduction simulations for correction factors are needed in order to apply these to the experimental measurements. It is expected that this system will solidify the validation of the Monte Carlo implementation for the ionization quenching problem.

The prototype SP-1 detector can benefit from additional characterization and development such that it can be used for in-situ (at the clinic) for determination of output correction factors for detectors used routinely by hospitals. Therefore, detectors used in the clinic will have a specific output correction factor for the specific clinical conditions.

Beam quality correction factors needs to be determined for ionization chambers in MV and Flattening Filter Free (FFF) beams using the SP-1. Using the calorimeter system, beam quality correction factors will not only be determined for an specific ionization chamber, but the question of whether ionization quenching is creating an energy dependence in organic plastic scintillators will be answered.

# APPENDIX A

## C++ ausgab object

---

The creation of `egs_light_scoring` as an `ausgab` object used in EGSnrc C++ applications is explained in details.

In the `HEN_HOUSE` part of the EGSnrc installation all the source code of EGSnrc are established. Following the path to the `egs++` folder (`$/HEN_HOUSE/egs++/`) the C++ part of EGSnrc can be found. In this folder several modifications need to be done.

1. In the file `egs_application.h`, section "Utility functions for use with `ausgab` dose scoring objects", add the following lines:

---

```
virtual EGS_Float getStPwr(int imed, EGS_Float E){  
    return -1.0;  
};
```

---

2. In the file `egs_advanced_application.h`, section "Utility functions for use with `ausgab` dose scoring objects", add the following line:

---

```
EGS_Float getStPwr(int imed, EGS_Float E);
```

---

3. In the file `egs_advanced_application.cpp`, section "Utility functions for use with `ausgab` dose scoring objects", add the following lines:

---

```
// returns the stopping power  
EGS_Float EGS_AdvancedApplication::getStPwr(int imed, EGS_Float E){  
    return i_ededx[imed].interpolate(log(E- the_useful->prm));  
}
```

---

After making the changes a compilation of each C++-based application is needed as they use the modified files. The source code of each application is lying in the `egs_home` folder (i.e `$/egs_home/`). For the sake of the instructions, the

application `egs_chamber` will be used as an example. Go to the the `$/egs_-home /egs_chamber` and enter the command: `'make clean'`, and once is finished enter: `'make'` and the application will be compiled.

## A.1 `egs_light_scoring`

Go to the folder `HEN_HOUSE` folder: `$/HEN_HOUSE/egs++ /ausgab_objects/`. In this folder the distributed ausgab objects are declared. The `egs_light_scoring` is based on `egs_dose_scoring`, therefore, make a copy of `egs_dose_scoring` folder and name it: `egs_light_scoring`. This folder will have three files; the makefile, the `egs_dose_scoring.h` and the `egs_dose_scoring.cpp`. In the copied folder, change the name of the `"egs_dose_scoring.h"` and `"egs_dose_scoring.cpp"` files by `"egs_light_scoring.h"` and `"egs_light_scoring.cpp"` respectively. Open the makefile file and replace in lines 37 and 38:

---

```
library = egs_dose_scoring
lib_files = egs_dose_scoring
```

---

by:

---

```
library = egs_light_scoring
lib_files = egs_light_scoring
```

---

Save and close the file. In the `egs_light_scoring.h` file after the following lines:

---

```
int ir = app->top_p.ir, imed = ir>=0 ? app->getMedium(ir):-1;
EGS_Float edep = app->getEdep();
```

---

insert the next line of commands:

---

```
int q = app->top_p.q;
EGS_Float stpwr = app->getStPwr(imed,app->top_p.E);
EGS_Float Gri;
if (q!=0){
    Gri = 1/(1+ kb*stpwr);
} else {
    Gri=1;
}
```

---

In the section of energy deposition (`**** energy deposition in current region ***`) replace the following lines:

---

```
if (iarg <= 4 && ir >= 0 && edep > 0 && dose) {
    dose->score(d_reg_index[ir], edep*app->top_p.wt);
```

---

```
}  

```

---

by:

---

```
if (iarg <= 4 && ir >= 0 && edep > 0 && dose) {  
    dose->score(d_reg_index[ir], edep*app->top_p.wt*Gri);  
}
```

---

After the following lines:

---

```
void setUserNorm(const EGS_Float &normi){  
    norm_u=normi;  
};
```

---

insert the following lines:

---

```
void setUserBirks(const EGS_Float &Birks){  
    kb=Birks;  
};
```

---

After the line:

---

```
EGS_Float norm_u;
```

---

add the line:

---

```
EGS_Float kb;
```

---

Save and close the file. In the egs\_light\_scoring.cpp, replace the following line:

---

```
#include "egs_dose_scoring.h"
```

---

by:

---

```
#include "egs_light_scoring.h"
```

---

After the following lines:

---

```
EGS_Float norma = 1.0;  
int err04 = input->getInput("normalization",norma);
```

---

insert the following lines:

---

```
EGS_Float Birks = 0;  
int err05 = input->getInput("kb",Birks);  
err05 = Birks;
```

---

Finally after the line:

---

```
result->setName(input);
```

---

insert the following line:

---

```
result->setUserBirks(Birks);
```

---

Then the code needs to be compiled by entering 'make' in the main folder (\$/HEN\_HOUSE/egs++ /ausgab\_objects/egs\_light\_scoring/). Once is compiled the code is ready to be used. With this code the light yield in an specific region in the defined geometry can be computed. The input commands are explained in section X.



**DTU Nutech**

Center for Nuclear Technologies

Technical University of Denmark

Frederiksborgvej 399

DK-4000, Roskilde

Denmark

<http://www.nutech.dtu.dk/english>

Tel: (+45) 4677 4900